AFRL-RX-WP-TR-2021-0133

FUNDAMENTAL LIMITS OF NONLINEAR OPTICAL EFFECTS FOR METALENS DESIGN WITH HIGH INDEX OPTICAL MATERIALS

Dr. Baris Unal
Triton Systems, Inc.

29 SEPTEMBER 2021
Final Report

**AIR FORCE RESEARCH LABORATORY
MATERIALS AND MANUFACTURING DIRECTORATE
WRIGHT-PATTERSON AIR FORCE BASE, OH 45433-7750
AIR FORCE MATERIEL COMMAND
UNITED STATES AIR FORCE**

NOTICE AND SIGNATURE PAGE

This report is the result of contracted fundamental research deemed exempt from public affairs security and policy review in accordance with SAF/AQR memorandum dated 10 Dec 08 and AFRL/CA policy clarification memorandum dated 16 Jan 09. This report is available to the general public, including foreign nationals. Copies may be obtained from the Defense Technical Information Center (DTIC) (http://discover.dtic.mil).

AFRL-RX-WP-TR-2021-0133 HAS BEEN REVIEWED AND IS APPROVED FOR PUBLICATION IN ACCORDANCE WITH ASSIGNED DISTRIBUTION STATEMENT.

_____   _____
AUGUSTINE URBAS   MARK SCHMITT
Program Manager   Branch Chief
Nanoelectronic Materials Branch   Nanoelectronic Materials Branch
Functional Materials Division   Functional Materials Division
Materials and Manufacturing Directorate   Materials and Manufacturing Directorate

This report is published in the interest of scientific and technical information exchange, and its publication does not constitute the Government's approval or disapproval of its ideas or findings.

REPORT DOCUMENTATION PAGE

Form Approved
OMB No. 0704-0188

The public reporting burden for this collection of information is estimated to average 1 hour per response, including the time for reviewing instructions, searching existing data sources, gathering and maintaining the data needed, and completing and reviewing the collection of information. Send comments regarding this burden estimate or any other aspect of this collection of information, including suggestions for reducing this burden, to Department of Defense, Washington Headquarters Services, Directorate for Information Operations and Reports (0704-0188), 1215 Jefferson Davis Highway, Suite 1204, Arlington, VA 22202-4302. Respondents should be aware that notwithstanding any other provision of law, no person shall be subject to any penalty for failing to comply with a collection of information if it does not display a currently valid OMB control number. **PLEASE DO NOT RETURN YOUR FORM TO THE ABOVE ADDRESS**.

1. REPORT DATE *(DD-MM-YY)*	2. REPORT TYPE	3. DATES COVERED *(From - To)*
29 September 2021	Final	19 December 2019 – 30 November 2021

4. TITLE AND SUBTITLE
Fundamental limits of nonlinear optical effects for metalens design with high index optical materials

5a. CONTRACT NUMBER
FA8650-20-C-7019

5b. GRANT NUMBER

5c. PROGRAM ELEMENT NUMBER
62715

6. AUTHOR(S)
Baris Unal

5d. PROJECT NUMBER
DARPA

5e. TASK NUMBER

5f. WORK UNIT NUMBER
X1X7

7. PERFORMING ORGANIZATION NAME(S) AND ADDRESS(ES)
Triton Systems Inc.
330 Billerica Rd, Chelmsford MA 01824

8. PERFORMING ORGANIZATION REPORT NUMBER

9. SPONSORING/MONITORING AGENCY NAME(S) AND ADDRESS(ES)
Air Force Research Laboratory
Materials and Manufacturing Directorate, Wright-Patterson Air Force Base OH 45433-7750
Air Force Materiel Command
United States Air Force

10. SPONSORING/MONITORING AGENCY ACRONYM(S)
AFRL/RXAN

11. SPONSORING/MONITORING AGENCY REPORT NUMBER(S)
AFRL-RX-WP-TR-2021-0133

12. DISTRIBUTION/AVAILABILITY STATEMENT
DISTRIBUTION STATEMENT A. Approved for public release; distribution is unlimited.

13. SUPPLEMENTARY NOTES
Report contains color.

14. ABSTRACT *(Maximum 200 words)*
This report was developed under DARPA contract number FA8650-20-C-7019. Triton Systems in collaboration of Material Alchemy, Yale University and Vanderbilt University explored the underlying physics behind a material's refractive index within optical frequencies. Our multipronged approach searched for fundamental limits of arbitrary materials to determine the upper bounds of refractive indices based on their materials properties to aid in future materials design. We compiled an extensive literature data from different materials classes to develop trends that relate a material's high refractive index to its structure, composition, and various parameters. From these trends, we employed Ab-initio simulations of previously unexplored materials to uncover possible high refractive indices for optical frequencies. We studied synthesis methods for high refractive index materials to probe large scale synthesis routes for future optical components.

15. SUBJECT TERMS
DARPA report, high refractive index metamaterials, giant refraction, giant index of refraction, limits of refractive index, nonlinear optics in high refractive index media

16. SECURITY CLASSIFICATION OF:

a. REPORT	b. ABSTRACT	c. THIS PAGE
Unclassified	Unclassified	Unclassified

17. LIMITATION OF ABSTRACT:
SAR

18. NUMBER OF PAGES
110

19a. NAME OF RESPONSIBLE PERSON (Monitor)
Augustine Urbas

19b. TELEPHONE NUMBER *(Include Area Code)*
(937) 255-9713

Standard Form 298 (Rev. 8-98)
Prescribed by ANSI Std. Z39-18

TABLE OF CONTENTS

Section   **Page**

LIST OF FIGURES

LIST OF TABLES

PROJECT SUMMARY

The project efforts incorporated efforts from (list co-workers) to explore the underlying physics behind a material's refractive index under optical frequencies. The multipronged approach searched for fundamental limits of arbitrary materials to determine the upper bounds of refractive indices based on their materials properties to aid in future materials design. Literature data was compiled from different materials classes to develop trends that relate a material's high refractive index to its structure, composition, etc. From these trends, Ab-initio simulations of previously unexplored materials were undertaken to uncover possible high refractive indices for optical frequencies. Synthesis methods for high refractive index materials were studied to probe large scale synthesis routes for future optical components.

1. IDENTIFYING THE PURPOSE OF THE WORK

DARPA DSO initiatives EXTREME and NLM are seeking new classes of optical materials and architectures which can set the stage for radically new capabilities in communications, computation, and imaging. New or enhanced nonlinear optical effects, leveraged or amplified by phase-change materials (PCMs), may enable entirely new realms of performance. Although NLO is not a new subject, the ultimate bounds on speed and magnitude of responses are not well understood. Recent discoveries in the science of natural materials, advances in synthetic and metamaterials, and better theoretical and computational tools for light-matter interactions, will all contribute to the next stage of NLO. DARPA seeks orders of magnitude enhancements, not incremental improvements.

The current effort centers around identifying maximal possible refractive index at optical frequencies as well as synthesis methods for fabricating such materials. To date, people use a unit-cell-based approach to design for large effective index, and there had been no known materials with minimal absorption and refractive index n greater than 3 at optical frequencies until a report last year of $n > 26$. We have developed an *ab initio* theory to understand fundamental limits to refractive index, based on causality-induced sum rules as well as probing the effects of band-structure engineering. In other words, our primary intent was to map out a computational framework and apply it to the estimate refractive indices of complex classes of bulk materials. This in turn, will help understand the underlying physics of the high refractive indices in complex materials. It will also provide an important component to design and engineer other high RI materials, in addition to the examples chosen in this one-year study. The identification of mechanisms for achieving high index, and candidate materials to achieve it, can have transformative impact across the field of applied optics for lenses and related devices.

This work is mapping out a computation-based framework for design of materials to estimate refractive indices of complex classes of materials. Our intent in one year is to demonstrate feasibility of a systematic framework for correlating structural components that enable bulk materials with high refractive indices. These would be key components to designing materials with high refractive indices. Given the complexity of the specific property related to refractive index (atom-light interactions) and effect of structures on these properties, the multi-step methodology. The top-level goal for the experiments was to demonstrate the feasibility of creating large-area metasurfaces with a ultra-high refractive index. Our objective is to "reverse-engineer" the features of a bulk crystalline, giant-refraction material (KTN:Li) lies at the boundary between materials science and optical physics

Currently, electronic dielectric constants for bulk materials are simulated using ab initio methods. For ionic parts, electron-phonon interactions are computed using perturbation methods. These are limited both because of the applicability to all the material classes and the time-intensive nature of the computations. As reported in Nature Photonics **12**, 734-738, the recent demonstration of giant refractive index material (KTN:Li) is in the form of a bulk crystal of millimeter dimensions, operated at a temperature near the boundary between the paraelectric and ferromagnetic phases. The limitations of this demonstration are that it requires a special crystal-growth technique based on a complex oxide material, and does not translate readily to implementation in the form of a large-area, thin optical component such as a lens.

2. BRIEF DESCRIPTION OF THE EFFORT ACCOMPLISHED

In this work, we derive fundamental limits to the refractive index of any material, given only the underlying electron density and either the maximum allowable dispersion or the minimum bandwidth of interest. The Kramers-Kronig relations provide a representation for any passive (and thereby causal) material, and a well-known sum rule constrains the possible distribution of oscillator strengths. In the realm of small to modest dispersion, our bounds are closely approached and not surpassed by a wide range of natural materials, showing that nature has already nearly reached a Pareto frontier for refractive index and dispersion. Surprisingly, our bound shows a cube-root dependence on electron density, meaning that a refractive index of 26 over all visible frequencies is likely impossible. Conversely, for narrow-bandwidth applications, nature does not provide the highly dispersive, high-index materials that our bounds suggest should be possible. We use the theory of composites to identify metal-based metamaterials that can exhibit small losses and 2X increases in refractive index over the current best materials. Moreover, if the elusive lossless metal" can be synthesized, we show that it would enable arbitrarily high refractive index, nearly achieving our bounds even at refractive indices of 100 and beyond at optical frequencies.

Materials trends for materials with high refractive indices were tabulated and analyzed. These trends in materials properties laid a computation groundwork for the application of ab-initio computations to predict the refractive index of complex materials such as perovskites or tertiary materials. We have the used a systematic computational approach to understand the basis of high dielectric constants to design materials atom by atom.

Thin films of high refractive index KTN and KTN:Li on centimeter scale substrates through sputtering methods for potential of scaling the materials production.

3. POTENTIAL APPLICATIONS OF THE RESULTS

We systematically mapped out a general theory of maximum refractive index at optical frequencies, via geometrical patterning of an effective response from known materials or atomistic engineering towards a bulk response of novel materials. Our work identified the frontier of what was possible, balancing considerations of larger index with possible constraints on loss and bandwidth. We delivered models at two scales – one bulk materials, engineering at the scale of the wavelength, and a second assuming ab-initio material synthesis, allowing electronic band-structure engineering – that provide guidance as to how to synthesize high-index materials and maximum possible refractive indices.

Utilizing the models and design rules discovered in this project, advances in optical and nanophotonic systems open new vistas for design: for applications ranging from broadband meta-lenses to ultrathin photovoltaics to high quality- factor resonators, higher index directly leads to better devices with greater functionality.

4. PROJECT OBJECTIVES MET

The project objectives met were to:

- Determine the upper bounds for refractive indices based on fundamental limits to understand how giant refractive indices can possibly be achieved through engineering the physical properties of a material.
- Determine broadband limits for high index effective responses
- Categorized vast classes of materials to tabulate their composition, structure, electronic, and optical properties
- Utilizing the categorized materials, an analysis was undertaken to determine trends in material properties and their relation to a high refractive index.
- Promising candidates and materials classes were studies through Density Functional Theory simulations to uncover new materials with potentially high refractive index materials
- Synthesis pathways were studied to fabricate materials with maximal refractive indices.
- Evaluations of fabrication methods to make large area materials with reasonable super-crystal quality.

5. WORK COMPLETED

5.1 LIMITATIONS OPTICAL FOCUSING AND DETERMINING BROAD BAND LIMITS

Increasing the refractive index of optical materials would unlock new levels of functionality in fields ranging from metasurface optics [1–7] to high-quality-factor resonators [8–14]. In this Article, we develop a framework for identifying fundamental limits to the maximum possible refractive index in any material or metamaterial, dependent only on the achievable electron density, the frequency range of interest, and possibly a maximum allowable dispersion. We show that the Kramer's– Kronig relations for optical susceptibilities, in conjunction with a well-known sum rule, impose surprisingly strong constraints on refractive-index line shapes, imposing strict limitations to refractive index at high frequency, with only weak (cube-root) increases possible through electron-density enhancements or large allowable dispersion. We show that a large range of questions around maximum index, including bandwidth-averaged objectives with constraints on dispersion and/or loss, over the entire range of causality-allowed refractive indices, can be formulated as linear programs amenable to computational global bounds, and that many questions of interest have global bounds with optima that are single Drude– Lorentz oscillators, leading to simple analytical bounds. For the central question of maximum index at any given frequency, we show that many natural materials already closely approach the Pareto frontier of tradeoffs with density, dispersion, and frequency, with little room (ranging from 1.1–1.5 times) for significant improvement. We apply our framework to high-index optical glasses (characterized by their Abbe number) and bandwidth-based bounds. For anisotropic refractive indices, or materials with magnetic in addition to electric response, we use a nonlocal-medium-based transformation to prove that any positive- or negative-semidefinite material properties cannot surpass these bounds, although there is an intriguing loophole for hyperbolic metamaterials. There are no natural materials in the regime of high index and high dispersion, but we show that composite metamaterials can be designed to have refractive indices approaching our bounds along this curve. With conventional metals such as gold and aluminum, we show that low-loss refractive indices of 5 in the visible, 18 in the near-infrared (3 µm wavelength), and 40 in the mid-infrared (10 µm wavelength) are achievable. If a near-zero-loss metal can be discovered or synthesized [15, 16], high-dispersion refractive indices above 100 would be possible at any optical frequency.

A large material refractive index n offers significant benefits for nanophotonic devices. First, the reduced internal wavelength enables rapid phase oscillations, which enable wavefront reshaping over short distances and is the critical requirement of high-efficiency meta-lenses and metasurfaces [1–7]. Second, it dramatically increases the internal photon density of states, which scales as n^3 in a bulk material [17] and offers the possibility for greater tunability and functionality. The enhanced density of states is responsible for the ray-optical $4n^2$ "Yablonovitch limit" to all-angle solar absorption [18] and the random surface textures employed in commercial photovoltaics. Third, high optical index unlocks the capability for near degenerate electric and magnetic resonances within nano resonators. Tandem electric and magnetic response is critical for highly directional control of waves; whereas a single electric dipole radiates efficiently in two equal and opposite directions, a tandem electric and magnetic dipole can radiate efficiently into a single, controllable direction, then forming the building blocks of complex, tailored scattering profiles [19–26]. Fourth, a large phase index can lead to a large group index, which underpins the entire field of slow light [27], for applications from delay lines to compressing optical signals. Finally, high refractive index enables significant reductions of the smallest possible mode volume in a dielectric resonator. Recent theoretical and experimental demonstrations show the possibility for highly subwavelength mode volumes in lossless dielectric materials [28–32]. In this case, a high refractive index increases the discontinuities in the electric and displacement fields across small-feature boundaries, enabling significant enhancements of the local field intensity that are useful for applications from single molecule imaging [33–36] to high-efficiency nonlinear frequency conversion [37–40].

The very highest refractive indices of transparent natural materials are 4 to 4.2 at near-infrared frequencies [41], and 2.85 at visible frequencies [42]. Metamaterials, comprising multiple materials combined in random or designed patterns, have been designed with refractive indices up to 5 at visible frequencies [43],

albeit with significant material losses. As the frequency is reduced, the refractive index can be significantly increased, a feature predicted by our bounds and borne out by the literature. Low-loss metamaterials have been designed to achieve refractive indices near 7 at infrared frequencies (3–6 µm) wavelengths [44], above 38 at terahertz frequencies [45], and above 1200 at microwave frequencies. Near the phase transition of ferroelectric materials, it is known (Chap. 16 of Ref. [46]) that in principle the refractive index is unlimited. Yet the caveat is that the frequency at which this occurs must go to zero. Experimental and theoretical studies have identified multiple materials with "colossal" static dielectric constants [47], even surpassing values of 10,000 [48]. All of these results are consistent with and predicted by the bounds that we derive.

Recently, scattering experiments on KTN:Li near its phase transition led to the claim of a refractive index of at least 26 across the entire visible region [49]. As we discuss further below, such a refractive index appears to be theoretically impossible: it would require an electron density and/or dispersion almost three orders of magnitude larger than those of known materials, an unprecedented anomaly. Thus, our work suggests that the experimental measurements may arise from linear-diffraction or even nonlinear optical effects, and do not represent a true phase-delay refractive index.

Theoretical inquiries into possible refractive indices have revolved around *models* that relate refractive index to other material properties, and particularly that of the energy gap in a semiconducting or insulating material. The well-known Moss Relation [50, 51] is a heuristic model that suggests that refractive index falls off as the fourth root of the energy gap of the material. This model can be effectively describe some materials over a limited energy range, but is not a rigorous relation and cannot be used for definite bounds. Another approach, related to ours, is to use the Kramer's–Kronig relation for refractive index to suggest that refractive index should scale with the square root of refractive index [52, 53]. But this approach has not been used for definite bounds, nor is the scaling relation correct: as we show, an alternative susceptibility-based sum rules shows that the refractive index should scale as the cube-root of electron density (for a fixed dispersion value, without which any value can in principle be arbitrarily high). A recent result utilizes renormalization-group theory to suggest that the refractive index of an ensemble of atoms must saturate around 1.7 (Ref. [53]). There have also been bounds on *nonlinear* susceptibilities using quantum-mechanical sum rules [54, 55], but, as far as we know, there have not been bounds for arbitrary materials on linear refractive index, which is the key controlling property for optics and nanophotonic applications.

Separately, bounds *have* been developed for other material properties, such as the minimum dispersion of a negative-permittivity or negative-index material [56, 57]. Such bounds utilize causality properties, similar to our work, to optimize over all possible susceptibility functions. There have also been claims of bounds on the minimum losses of a negative-refraction material [58], though recent work [59] has identified errors in that reasoning and shown that lossless negative-refraction materials are possible, in principle. If the approaches of these papers were directly applied to refractive index, they would yield trivially infinite bounds, as they do not use of electron density sum rule of Eq. (2) below. Interestingly, if one were to apply this electron-density sum rule to the problems of negative permittivity and negative index, it may tighten the bounds of Refs. [56–58], especially at high frequencies. We discuss this possibility further in the Conclusion, Sec. 8. VII.

In this paper, we establish the maximal attainable refractive index for arbitrary passive, linear, isotropic media, applicable to naturally occurring materials as well as artificial metamaterials. We first derive a general representation of optical susceptibility starting from Kramer's–Kronig relations (Sec. 8. I), enabling us to describe any material by a sum of Drude–Lorentz oscillators with infinitesimal loss rates (Sec. 8. I). By considering a design space of an arbitrarily large number of oscillators, the susceptibility is a linear function of the degrees of freedom, which are the oscillator strengths.

Many constraints (dispersion, bandwidth, loss rate, etc.) are also linear functions of the oscillator strengths, which themselves are constrained by the electron density via a well-known sum rule. Thus a large set of questions around maximum refractive index are *linear programs*, whose global optima can be computed quickly and efficiently [60]. The canonical question is: what is the largest possible refractive index at any

frequency ω, such that the material dispersion is bounded? In Sec. 8. II we show that this linear program has an *analytical* bound, which is a single, lossless Drude–Lorentz oscillator that corresponds to sharp two-level transitions. These bounds describe universal tradeoffs between refractive index, dispersion, and frequency, and we show that many natural materials and metamaterials closely approach the bounds. We then devote a separate section (Sec. 8. III) to optical glasses, which are highly studied and critical for high-quality optical components. We show that our bounds closely describe the behavior of such glasses, and that there may be opportunities for improvement at low Abbe numbers (high dispersion values). An alternative characterization for refractive index may not be a specific dispersion value, and instead a desired bandwidth of operation, and in Sec. 8. IV we derive bounds on refractive index as a function of allowable bandwidth. Across all of our bounds we find that there may be small improvements possible relative to current materials (1.1–1.5×). Finally, we consider the possibilities of anisotropy and/or magnetic response (Sec. 8. V). We show that a large swath of such effects cannot lead to higher refractive indices, and are subject to the same isotropic-index bounds derived earlier in the paper. We also find intriguing loopholes including gyrotropic plasmonic media (which have a modified Kramer's–Kronig relation) and hyperbolic metamaterials, although the former may be particularly hard to achieve at optical frequencies while the latter may be difficult to achieve with low losses. We identify exactly the material properties that enable such loopholes. Furthermore, we use the theory of composites to design highly dispersive, high-index metal-based metamaterials with low losses not realized in nature (Sec. 8. VI). In the Conclusion, Sec. 8. VII, we discuss possible extensions of our framework to incorporate alternative metrics, gain media, anomalous dispersion, and nonlinear response.

5.1.1 MAXIMUM REFRACTIVE INDEX AS A LINEAR PROGRAM

To identify the maximal refractive index, one first needs a representation of all physically allowable optical material properties. We consider here a transparent, isotropic, nonmagnetic material, which can be described by its refractive index n, relative permittivity $\varepsilon = n^2$, or its susceptibility $\chi = \varepsilon - 1$. (We discuss extensions to anisotropic and/or magnetic materials in Sec. 8. V and we discuss the possible inclusion of loss below.) Instead of assuming a particular form for the susceptibilities (like a small number of Drude–Lorentz oscillators), we assume only passivity: that the polarization currents in the material do no net work. Any passive material must be causal [61]; causality, alongside technical conditions on the appropriate behavior at infinitely large frequencies in the complex plane, implies that each of the material parameters must satisfy the *Kramer's–Kronig* (KK) relations. One version of the KK relation for the material susceptibility relates its real part at one frequency to a principal-value integral of its imaginary part over all frequencies:

$$\operatorname{Re}\chi(\omega) = \frac{2}{\pi} \int_0^\infty \frac{\omega' \operatorname{Im}\chi(\omega')}{\omega'^2 - \omega^2}\, \mathrm{d}\omega'.$$

(1)

With the exception of gyrotropic plasmonic response [62], whose presence is negligible at optical frequencies, any material's susceptibility must satisfy Eq. (1). This restriction already imposes bounds on regions of negative dispersion [56–58], but it does not by itself impose any bound on how large the real part of the susceptibility (and correspondingly the refractive index) can be. The key constraint is the "*f*-sum rule:" a certain integral of the imaginary part of the susceptibility *must* equal a particular constant multiplied by the electron density N_e of the medium. Typically, electron density is folded into a frequency ω_p, which for metals is the plasma frequency but for any material describes the high-frequency asymptotic response of the material. The *f*-sum rule for the susceptibility is [63–65]

$$\int_0^\infty \omega' \operatorname{Im}\chi(\omega')\, \mathrm{d}\omega' = \frac{\pi e^2 N_e}{2\varepsilon_0 m_e} = \frac{\pi \omega_p^2}{2}.$$

(2)

7

where e is the charge of an electron, ε_0 the free-space permittivity, and m_e the electron rest mass. This sum rule arises as an application of the KK relation of Eq. (1): at high enough frequencies ω, the material must be nearly transparent, with only a perturbative term that arises from the individual electrons without any multiple scattering effects. The sum rule of Eq. (2) is the critical constraint on refractive index: intuitively, it places a limit on the distribution of oscillators in any material; mathematically, it limits the distribution of the measure $\omega' \text{Im}\chi(\omega')\text{d}\omega'$ that appears in Eq. (1).

To simulate any possible material, we must discretize Eqs. (1,2) in a finite-dimensional basis. If we use a finite number N of localized basis functions (e.g. a collocation scheme [66] of delta functions), straightforward insertion of the basis functions into Eq. (2), in tandem with the constraint of Eq. (1), leads to a simple representation of the susceptibility:

$$\text{Re}\,\chi(\omega) = \sum_{i=1}^{N} \frac{c_i \omega_p^2}{\omega_i^2 - \omega^2},$$
(3)

$$\sum_i c_i = 1$$
(4)

Equation (3) distills the Kramer's–Kronig relation to a set of lossless Drude–Lorentz oscillators with transition frequencies ω_i and relative weights, or oscillator strengths, c_i. Equation (4) is a renormalized version of the f-sum rule of Eq. (2), thanks to the inclusion of ω_p^2 in the numerator of Eq. (4). There is one more important restriction on the c_i values: they must all be positive, since $\omega^0 \text{Im}\chi(\omega^0)$ must be positive for a passive material. Given Eqs. (3,4), it now becomes plausible that there is a bound on refractive index: the oscillators of Eq. (3) represent all possible line shapes, and the sum rule of Eq. (4) restrict the oscillator strengths, and effective plasma frequencies, of the constituent oscillators.

It is important to emphasize that the constants in the sum rule of Eq. (2) are indeed constants; in particular, that the mass m_e is the free-electron mass and not an effective mass of an electron quasiparticle. In interband models [67, 68], the linear susceptibility can be written as a sum of Drude–Lorentz oscillators similar to Eq. (3) and containing the effective masses of the relevant bands. But for those models, the sum over all bands leads to the free-electron mass in the final sum rule [68]. Alternatively, one can use the fact that electrons can be considered as free, non-interacting particles in the high frequency limit [69]. Thus the only variable in the sum rule is the electron density, which itself does not vary all that much over all relevant materials at standard temperatures and pressures. It is equally important to emphasize that the representation of Eq. (3) does not rely on any of the standard assumptions of interband models (no many-body effects, periodic lattice, etc.), and is valid for *any* linear (isotropic) susceptibility, assuming only passivity. Equation (3) is *not* a Drude–Lorentz approximation or model; instead, it is a first-principles representation of the Kramer's–Kronig relations.

To determine the maximum possible refractive index, one could maximize Eq. (3) over all possible sets of parameter values for the oscillator strengths and transition frequencies, c_i and ω_i, respectively. However, a global optimization over the Drude–Lorentz form that is nonlinear in the ω_i will be practically infeasible for a large set of transition frequencies. Instead, we *a priori* fix a very large number of possible oscillator transition frequencies ω_i, and then treat only the corresponding oscillator strengths c_i as the independent degrees of freedom. This "lifting" transforms a moderately large nonlinear problem to a very large linear one, and there are well developed tools for rapidly solving for the global optima of linear problems [60, 70].

Crucially, not only is the susceptibility linear in the oscillator-strength degrees of freedom c_i, but so are many possible quantities of interest for constraints: first-, second-, and any-order frequency derivatives of the susceptibility, loss rates (the imaginary part of the susceptibility), etc. Thus maximizing refractive index over any bandwidth, or collection of frequency points, subject to any constraints over bandwidth or dispersion, naturally leads to generic linear programs of the form:

$$\begin{aligned}
\underset{c}{\text{maximize}} \quad & z^T c \\
\text{subject to} \quad & A_j^T c + b_j \leq 0 \\
& 1^T c = 1 \\
& c \geq 0.
\end{aligned} \tag{5}$$

where c without a subscript denotes the length-N vector comprising the oscillator strengths, j indexes any number of possible constraints, the constraint $1^T c = 1$ corresponds to the sum rule $^P{}_i c_i = 1$, and z, A_i, and b_i are the appropriate vectors and matrices that are determined by the specific objectives, constraints, and frequencies of interest. There are well-developed tools for rapidly solving for the global optima of linear problems such as Eq. (5), and in the following sections we detail relevant questions that share this form.

Equation (5) represents the culmination of our transformation of generic refractive-index-maximization problems to linear programs. A natural question might be why we use the Kramer's–Kronig relation, Eq. (1), and sum rule, Eq. (2), for material susceptibility χ instead of refractive index n directly? In fact, one could replace all of the preceding equations with their analogous refractive-index counterparts, and arrive at an analogous linear-program formulation for refractive index. But the bounds would be significantly looser, the physical origins for which we explain in Sec. 8. IIC. Instead, it turns out that the susceptibility-based formulation presented above leads to bounds that are rather tight.

5.1.2 SINGLE-FREQUENCY BOUND

5.1.2.1 FUNDAMENTAL LIMIT

A canonical version of the refractive-index question is: what is the largest possible refractive index of a transparent (lossless) medium, at frequency ω, subject to some maximum allowable dispersion? The dispersion constraint is important for many applications, from metalenses to photovoltaics, where one may want to operate over a reasonable bandwidth or minimize the phase and/or group-velocity variability that can be difficult to overcome purely by design [71, 72]. Given the susceptibility representation of Eqs. (3,4) in Sec. 8. I, we can formulate the maximum-refractive-index question in terms of the susceptibility, and then transform the optimal solution to a bound on refractive index. We assume here a nonmagnetic medium, in which case we can connect electric susceptibility to refractive index; in Sec. 8. V we show that the same bounds apply even in the presence of magnetic response.

The formulation of this canonical single-frequency refractive-index-maximization question as a linear program is straightforward. The Kramer's–Kronig representation of Eq. (3) can be written as $\chi(\omega) = \Sigma_i c_i f_i(\omega)$,
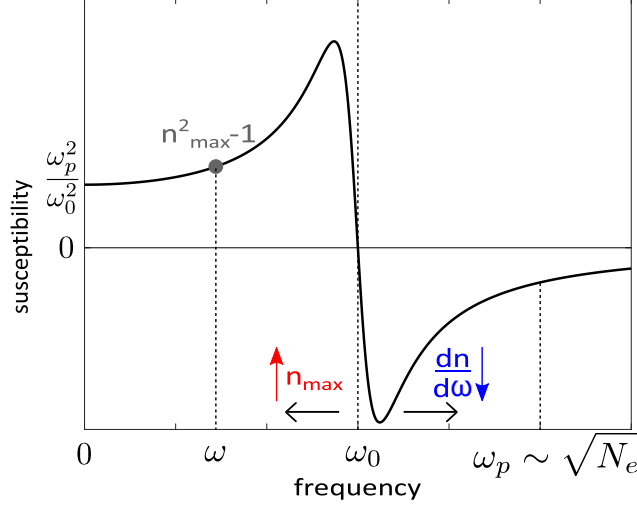
Figure 1. Schematic representation of a single Drude–Lorentz oscillator, depicting the tradeoff between refractive index and dispersion. Decreasing the resonance frequency ω_0 increases the ratio $\frac{\omega_p^2}{\omega_0^2}$ and hence the maximum refractive index n_{max} at ω, but at the cost of higher dispersion $\frac{dn}{d\omega}$ (and vice versa for increasing ω_0). $\omega_p = \sqrt{\frac{N_e e^2}{\epsilon_0 m_e}}$ The plasma frequency is determined by the material's electron density.

where f_i at frequency ω is given by $f_i(\omega) = \omega_p^2/(\omega_i^2 - \omega^2)$ and $\chi(\omega)$ is linear in the c_i values. The dispersion, as measured by the frequency derivative of the real part of the susceptibility, has the same representation but with $f_i(\omega)$ replaced by its derivative $f_i^0(\omega) = 2\omega\omega_p^2/(\omega_i^2 - \omega^2)^2$. Then, the largest possible susceptibility at frequency ω, with dispersion constrained to be smaller than an application-specific constant χ^0, is the solution of the optimization problem:

$$\begin{aligned}
\underset{c_i}{\text{maximize}} \quad & \text{Re}\,\chi(\omega) = \sum_{i=1}^{N} c_i\, f_i(\omega) \\
\text{subject to} \quad & \frac{\text{d}\,\text{Re}\,\chi(\omega)}{\text{d}\omega} = \sum_{i=1}^{N} c_i\, f_i'(\omega) \leq \chi', \\
& \sum_{i=1}^{N} c_i = 1,\; c_i \geq 0.
\end{aligned}$$

(6)

Equation (6) is of the general linear-program form in Eq. (5). Comparing the two expressions, the vector z has $f_i(\omega)$ as its elements. There is only a single index j, with matrix A_1 given by a single column with values $g_i(\omega)$ and vector b_1 with value of $-\chi^0$ multiplied by a vector of 1's. To computationally optimize the maximum-index problem of Eq. (6), one must simply represent a sufficiently large space of possible oscillator frequencies ω_i. Since we are interested in transparent (lossless) media, there should not be any oscillator at the frequency of interest ω (otherwise there will be significant absorption). Nor should there be any frequencies $\omega_i < \omega$, which can only reduce the susceptibility at ω. Thus, one only needs to consider oscillator strengths ω_i greater than ω.

Strikingly, for any frequency ω, electron density N_e (or plasma frequency ω_p), and allowable dispersion χ^0, the optimal solution to Eq. (6) is always represented by a single nonzero oscillator, with strength $c_0 = 1$ and frequency

$\omega_0 = \omega\sqrt{1 + \sqrt{2\omega p2/(\omega 3\chi 0)}}$. We prove in the SM that the single-oscillator solution is globally optimal. The intuition behind the optimality of a single oscillator can be understood from Fig. 1. The susceptibility of a single oscillator is governed by three frequencies: the frequency of interest, ω, the oscillator frequency, ω_0, and the electron-density-based plasma frequency, ω_p. The static susceptibility of such an oscillator at zero frequency is given by $\chi = \omega_p^2/\omega^2$. This sets a starting point for the susceptibility that ideally should be as large as possible. The plasma frequency is fixed for a given electron density, and thus the only way to increase the static susceptibility is to reduce the oscillator frequency ω_0 (as indicated by the black left arrow). Yet this comes with a tradeoff: as ω_0 decreases, the oscillator nears the frequency of interest, and the dispersion naturally increases. Hence for minimal dispersion one would want as large of an oscillator frequency as possible. A constraint on allowable dispersion thus imposes a bound on how small of an oscillator frequency one can have, and the maximum refractive index is achieved by concentrating all of the available oscillator strength at that frequency.

The single-oscillator optimality of the solution to Eq. (6) leads to an *analytical* bound on the maximum achievable refractive index. Denoting a maximal refractive-index dispersion $n' = \chi'/2n$ (from $\chi = n^2 - 1$), straightforward algebra (cf. SM) leads to a general bound on achievable refractive index:

$$\frac{(n^2 - 1)^2}{n} \le \frac{\omega_p^2 n'}{\omega}. \tag{7}$$

Equation (7) is a key result of our paper, delineating the largest achievable refractive index at any frequency for any causal, linear, isotropic material. Equation (7) highlights the three key determinants of maximum refractive index: electron density, allowable dispersion, and frequency of interest. We will discuss each of these three dependencies in depth. First, though, there is a notable simplification of the refractive index bound, Eq. (7), when the refractive index is moderately large. In that case, the left-hand side of Eq. (7) is simply the cube of n; taking the cube root, we have the high index ($n^2 \gg 1$) bound:

$$n \le \left(\frac{\omega_p^2 n'}{\omega}\right)^{1/3}. \tag{8}$$

The cube-root dependence of the high-index bound, Eq. (8) is a strong constraint: it says that increasing electron density or allowable density by even a factor of 2 will only result in a $\sqrt[3]{2} \approx 1.26X$ enhancement. Similarly, even an order-of-magnitude, 10X increase in either variable can only enhance refractive index by a little more than 2X. Thus the opportunity for significant increases in refractive index are highly limited. The cube root dependence that is responsible for this constraint is new and surprising: conventional arguments suggest that refractive index should scale with the square root of electron density [69]. Moreover, applying our analysis to the Kramer's–Kronig representation of refractive index also leads to square-root scaling. It is the fact that the *susceptibilities* of nonmagnetic materials, in addition to their refractive indices, must satisfy Kramer's–Kronig relations that ultimately leads to the tighter cube-root dependence.

To investigate the validity of our bounds of Eqs. (7,8), we compare them to the actual refractive indices of a wide range of real materials. To compare the bound to a real material at varying frequencies, we must account for the different electron densities, dispersion values, and frequencies of interest for those materials. To unify the comparisons, we use the bound of Eq. (7) to define a material-dependent refractive-index "figure of merit,"

$$\text{FOM} \equiv \left[\frac{(n^2 - 1)^2}{n\omega_p^2 n'} \right]^{1/3} \leq \frac{1}{\omega^{1/3}}. \tag{9}$$

which is approximately the refractive index rescaled by powers of the plasma frequency and allowable dispersion. On the right-hand side of Eq. (9) is the factor $1/\omega^{1/3}$, which is the upper bound to the material figure of merit for any material.

Figure 2 compares the material-figure-of-merit bound (solid black line) to the actual material figure of merit for a wide range of materials (colored lines and markers) [42, 74–96]. We use the experimentally determined refractive indices and dispersion values for each material. Parts (a) and (b) of the figure are identical except for the values of the electron density: in part (b), we use the total electron density of each material, while in part (a) we use only the valence electron density. The valence electron-density bound is not a rigorous bound, but in practice it is only the valence electrons that contribute to the refractive index at optical frequencies, and one can see that the bound in (a) is tighter than that of (b) due to the use of the valence densities, while not being surpassed by any real materials. Within the materials considered, we use the line and marker colors to distinguish materials that are transparent at infrared (IR), visible, and ultraviolet (UV) frequencies, respectively. The higher the frequency of interest, the lower the material FOM bound is (and the lower the refractive-index bound is), because at higher frequencies the oscillator frequency must increase to prevent the dispersion value from surpassing its limit, and a higher oscillator frequency reduces the electrostatic index that sets a baseline for its ultimate value (as can be seen in Fig. 1).

Three metamaterials structures [43, 44, 73] are included in Fig. 2. These metamaterials are patterned to exhibit anomalously large effective indices (ranging from 5 to 10). Ultimately, these metamaterials are configurations of electrons that effectively respond as a homogeneous medium with some refractive index, and thus they too are subject to the bounds of Eqs. (7,8). Indeed, as shown in Fig. 2, two of the metamaterials approach the valence-electron bound line, but do not surpass it. Their high refractive indices are accompanied by dramatically increased chromatic dispersion.

Many materials can approach the bound over a small window of frequencies where their dispersion is minimal relative to their refractive index. Two outliers are silicon and germanium, which approach the bound across almost all frequencies at which they are transparent. Silicon, for example, has a refractive index ($n = 3.4$) that is within 16% of its valence-density-based limit. The key factor underlying their standout performance is a subtle one: the absence of optically active phonon modes. It turns out that optical phonons primarily increase the dispersion of a material's refractive index without increasing its magnitude. From a bound perspective, this can be understood from the sum rule of Eq. (2). In that sum rule, the total oscillator strength is connected to the electron density of a material, divided by the free-electron mass. Technically, there are additionally terms in the sum rule for the protons and neutrons [97]. However, their respective masses are so much larger than those of electrons that their relative contributions to the sum rule is insignificant. Similarly, because phonons are excitations of the lattice, their contribution to refractive index comes from the proton and neutron sum-rule contributions, and are necessarily insignificant in magnitude at optical frequencies. They can, however, substantially alter the dispersion of the material, and indeed that is quite apparent in the refractive indices of many of the other materials (e.g. GaAs, InP, etc.), which thus tend to fall short of the bounds at many frequencies. This result also suggests that ideal high-index materials should not host active optical phonons, which increase dispersion without increasing refractive index.

Figure 2. Comparison of representative high-index materials, as well as three metamaterial designs (visible metasurface [43], 3D metamaterial [44], meso-crystal [73]) from the literature, as measured

by the FOM = $\left[\dfrac{(n^2-1)^2}{n\omega_p^2 n} \right]^{1/3}$ $\approx \dfrac{n}{N_e n}$ **for n >> 1 ($N_e n'$ normalized to that of valence SiO$_2$ at 400 nm),**

plotted against the material-independent bound in Eq. (9). Shown above are two figures, based on (a) total and (b) valence electron density, which only shifts the FOM for each material without distorting qualitative features. The materials can be broadly classified into three categories depending on the spectrum at which they are transparent—UV (LiF [74], MgF$_2$ [74], CaF$_2$ [74], SiO$_2$ [75, 76], Al$_2$O$_3$ [75, 77], Si$_3$N$_4$ [78], diamond [79]), visible (HfO$_2$ [80], ZrO$_2$ [81], LiNbO$_3$ [82], ZnS [83, 84], GaN [85], ZnSe [86], TiO$_2$ [42]), and IR (ZnTe [87], InP [88], GaAs [89], Si [90], InAs [91], Ge [92], PbS [93], PbSe [93], Te [94, 95], PbTe [96]). Most materials approach the bound quite closely at different frequencies, with silicon at IR outperformed only by a factor of 1.16 relative to the bound. The parabolic shape bending downwards at IR frequencies can be attributed to phonon dispersion, notable exceptions being silicon and germanium, which are IR-inactive and hence highly transparent even in mid-IR (i.e. very non-dispersive). The quality factor for the perovskite sample produced in [1] is off of the current scale for the both graphics.

Table I presents numerical values of valence electron densities, dispersion values, refractive indices, and their bounds for representative materials averaged over the visible spectrum (see SM for more details on bounds for nonzero bandwidth). One can see that for a wide variety of materials [42, 74–82, 85] and dispersion values, there is a close correspondence between the actual refractive index and the bound, for both natural materials and artificial metamaterials. Taken together, Fig. 2 and Table I show that many materials can closely approach their respective bounds, showing little room for improvement at the dispersion values naturally available. These results also cast doubt about the result of Ref. [49]: a refractive index of 26 at optical frequencies is an order of magnitude larger than any of the natural materials in Table I. Because of the cube-root scaling of the bound of Eqs. (7,8), a 10X increase in refractive index requires a 1000-fold increase in electron density or dispersion. Large dispersion would inhibit the possibility for the broadband nature of the result in Ref. [49], hence the only remaining possibility is a $\approx 1000X$ increase in electron density. Yet this would be orders of magnitude larger than the largest known electron densities [46]. Hence, our results strongly suggest that the light-bending phenomena of Ref. [49] are due to diffractive or nonlinear effects, instead of a linear refractive index.

5.1.2.2 MAXIMUM INDEX VERSUS CHROMATIC DISPERSION

To visualize the tradeoff between maximal refractive index and dispersion, Fig. 3 depicts the refractive-index bound of Eq. (7) as a function of chromatic dispersion, for materials transparent at three different wavelengths: infrared (λ = 5um), visible (λ = 700nm), and ultraviolet (λ = 320nm). We use dispersion with respect to wavelength, i.e. $dn/d\lambda$, instead of frequency, as the wavelength derivative is commonly used in optics [98]. Without careful attention to the wavelength of interest, it would appear that refractive index tends to decrease as dispersion increases: silicon, for example, has both a higher refractive index and smaller dispersion than titanium dioxide, at their respective transparency wavelengths. Yet our bound of Eq. (7) highlights the key role that wavelength is playing in this comparison: the bound shows that maximum index must decrease with increased dispersion but increase at longer wavelengths. Within each color family in Fig. 3, wavelength is held constant, and then it is readily apparent that maximum index increases as a function of chromatic dispersion. One can see that in each wavelength range, many materials are able to approach our bounds across a wide range of dispersion levels. The largest gaps between actual index and that of the bound occur for infrared III-V and II-VI materials, due to the presence of active optical phonons, as discussed above.

Table 1. High-index materials transparent over the visible spectrum, showing the (valence) electron density N_e, dispersion $\frac{dn}{d\omega}$ refractive index n, and upper bound on n for each material. The table shows that refractive index, as well as its bound, increases with dispersion, and that they closely approach the bound. Except for the metamaterial, all the quantities listed above are averaged over 400–700 nm. [a] refers to the metamaterial in Ref. [43], here evaluated at $\approx$ 710 nm.

Material	Electron density N_e (10^{23} cm−3)	Dispersion $\frac{dn}{d\omega}$ (eV^{-1})	Refractive index n	Bound on n
		(averaged over 400–700 nm)		
MgF$_2$	4.85	0.0059	1.38	1.58
CaF$_2$	3.92	0.0076	1.43	1.60
SiO$_2$	4.25	0.0112	1.46	1.73
Al2O3	5.67	0.0176	1.77	2.04
Si3N4	4.39	0.0514	2.06	2.48
HfO$_2$	4.65	0.0482	2.13	2.49
ZrO$_2$	4.75	0.0597	2.18	2.63
LiNbO$_3$	4.52	0.1266	2.34	3.12
C (diamond)	7.04	0.0436	2.43	2.74
GaN	3.03	0.1448	2.45	2.97
TiO$_2$	5.11	0.3342	2.72	4.17
Metamaterial [a]	0.59	$\approx$ 4.1	$\approx$ 5.1	$\approx$ 5.7

At visible and UV frequencies, where phonon contributions are negligible, the deviation of refractive indices from their respective bounds can be attributed to the distributions of oscillator strengths, manifest in the frequency dependence of $\text{Im}\chi(\omega)$. The larger the frequency spread (variance) of $\text{Im}\chi$ relative to its average frequency, the more a material's refractive index falls short of the bound (cf. SM). Note that for a fixed frequency of interest, the average frequency of the optimal oscillator depends directly on the maximum allowable
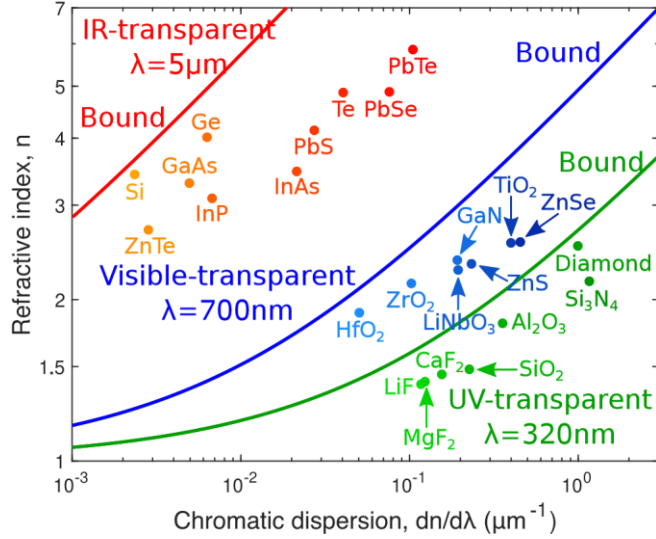
Figure 3. Refractive indices of various materials evaluated at three different wavelengths (320 nm, 500 nm, 5 μm) based on the spectrum at which they are transparent (UV, visible, and IR respectively), compared to their respective bounds. For each wavelength, the average electron density of all materials belonging to that wavelength was used to compute the bound. The bounds show refractive index increasing with dispersion, as measured by (the magnitude of) chromatic dispersion $\frac{dn}{d\omega}$, as also demonstrated by materials closely aapproaching the bounds.

dispersion: larger dispersion implies smaller oscillator frequency, and vice versa. Hence, higher-dispersion materials have smaller average oscillator frequencies, which reduces the total variance allowed before significant reductions relative to the bounds arise. Diamond would appear to be an exception, but that is only because its valence electron density is much larger than average; its gap to its respective bound is as expected. To summarize: highly dispersive materials are more sensitive to deviations of $\mathrm{Im}\chi(\omega)$ from the ideal delta function than are small-dispersion materials. A direct comparison can be done for TiO_2 and HfO_2, which have similar oscillator spreads but a smaller center frequency for TiO_2. This explains why TiO_2 is farther from its bound than is HfO_2, and explains the general trend of increasing gaps with increasing dispersion.

5.1.2.3   BOUNDS FROM REFRACTIVE-INDEX KK RELATIONS

In Sec. 8. I, we noted the importance of using Kramer's– Kronig relations for the *susceptibility* instead of KK relations for refractive index. Here, we briefly show the bound that can be derived via refractive-index KK relations, and explain why the two bounds are quite different. Analogous to the sum rule of Eq. (2), there is a sum rule on the distribution of the imaginary part of refractive index that also scales with the electron density:

$\int_0^\infty \omega \, \mathrm{Im}\, n(\omega)\, \mathrm{d}\omega \,=\, \pi\omega_p^2/4$ (Ref. [65]). Similarly, there is a KK relation for refractive index that exactly mimics Eq. (1). Together, following the same mathematical formulation as in Sec. 8. I, one can derive a corresponding bound on refractive index given by (cf. SM):

$$n \leq 1 + \frac{\omega_p}{2}\sqrt{\frac{n'}{\omega}}.$$

.   (10)

To distinguish the two bounds from each other, we will denote this bound, Eq. (10), as the n-KK bound, and the susceptibility-based bound, Eq. (7), as the χ-KK bound. Equation (10) shows that the n-KK bound has a square root dependence on the parameter $\frac{\omega_p^2 n'}{\omega}$, in contrast to the cube-root dependence for the χ-KK bound (explicitly shown in Eq. (8) for high-index materials). The nKK bound is always smaller than the χ-KK bound (cf. SM, TODO), and the square-root versus cube-root dependencies implies that the gap increases with dispersion or electron density. Figure 4(a) shows the difference between the two bounds, and the increasing gap between them at large plasma frequencies
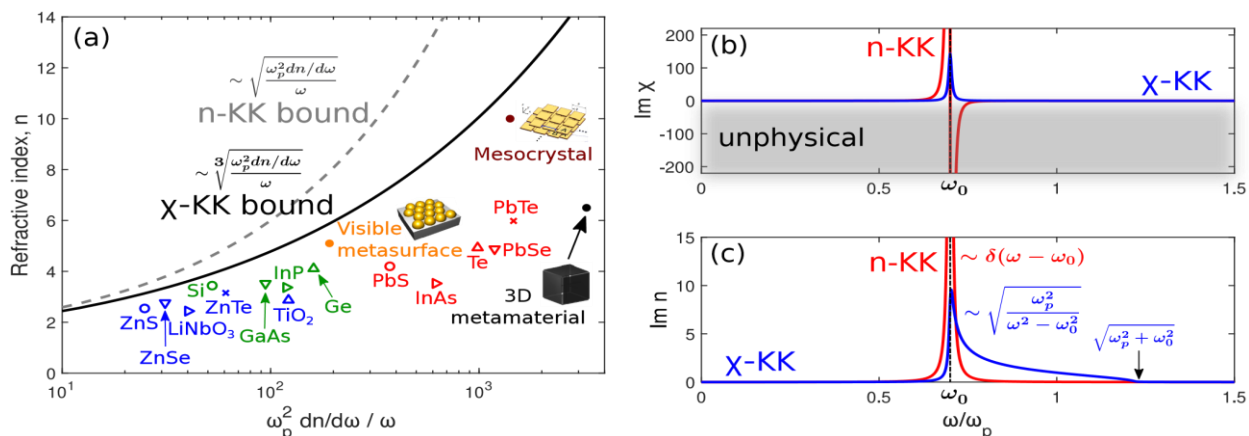
Figure 4. (a) Comparison of bounds based on Kramer's–Kronig relations on susceptibility, Eq. (7), and refractive index, Eq. (10), denoted as n-KK and χ-KK bound respectively. Natural materials are categorized in terms of the frequencies at which they obtain the highest refractive index (visible, near-IR, and mid-IR, marked as blue, green, and red respectively). All the materials lie below the χ-KK bound. (b) Optimal Imχ profiles attaining the n-KK and χ-KK bound. Around the resonance frequency ω_0, Imχ for the former goes negative, which is not allowed by passivity. (c) Optimal Imn profiles attaining the n-KK and χ-KK bound. In contrast to an infinitely sharp resonance for the former, the latter is characterized by a broadened line shape to the right of ω_0. For (b) and (c), the loss rate was taken to be small but nonzero ($\gamma = 0.01\omega_p$) for purposes of illustration.

or allowable dispersion. Figure 4(b,c) shows the physical origins of the discrepancy between the two approaches. The optimal n-KK solution has a delta-function imaginary part of its refractive index, as in Fig. 4(c), concentrating all of the imaginary part in a single refractive-index oscillator. Yet for a delta function in Imn, the imaginary part of the electric susceptibility *must* go negative in a nonmagnetic material, as in Fig. 4(b), which is unphysical and violates passivity. By contrast, the optimal solution in the χ-KK bound is a delta function in susceptibility, as in Fig. 4(b), which yields a smoother distribution of Im$n(\omega)$, as seen in Fig. 4(c). Hence another way of understanding the surprising cube-root dependency of our bound is that it arises as a unique consequence of the fact that both refractive index n and its square, $n^2 = \chi + 1$, obey Kramer's–Kronig relations [61].

5.1.3 BOUND ON OPTICAL GLASSES

The optical glass industry has put significant effort into designing high-index, low-dispersion optical glasses. Thus, transparent optical glasses provide a natural opportunity to test our bounds. It is common practice to categorize refractive indices at specific, standardized wavelengths. The refractive index n_d refers to refractive index at the Fraunhofer d spectral line [100], for wavelength $\lambda = 587.6$nm, in the middle of the visible spectrum. Dispersion is measured by the Abbe number V_d [101, 102]:

$$V_d = \frac{n_d - 1}{n_F - n_C},$$

(11)

where n_F and n_C are evaluated at 486.1nm and 656.3nm, the Fraunhofer F and C spectral lines, respectively (the Abbe number can be defined differently based on other spectral lines, but the above convention is commonly used to compare optical glasses [103]).
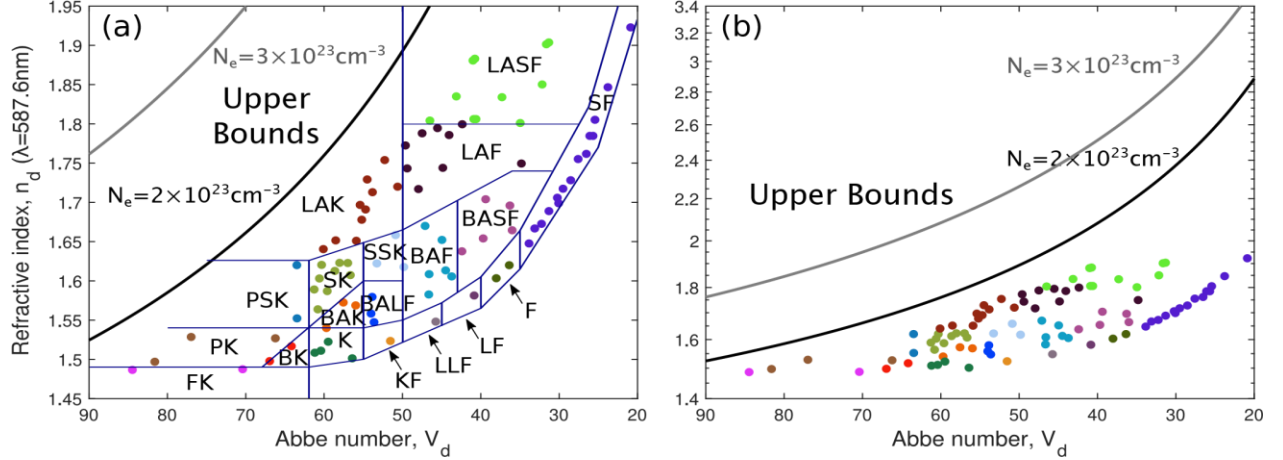
Figure 5. (a) Abbe diagram showing the glasses categorized depending on their refractive indices (at 587.6 nm) n_d and Abbe number V_d, compared to the bounds for electron density $N_e = 2 \times 10^{23}\,\mathrm{cm}^{-3}$ (black line) and $N_e = 3 \times 10^{23}\,\mathrm{cm}^{-3}$ (gray line). (b) Same plot but shown in logarithmic scale with larger range of values to fully illustrate the bounds. The data for different glass categories was obtained from Ref. [99].

The quantity in Eq. (11) cannot be directly constrained in our bound framework, as it is nonlinear in the susceptibility, but optical glasses of interest have sufficiently weak dispersion that their refractive indices can be approximated as linear across the visible spectrum. Then, we can relate the Abbe number directly to the dispersion of the material at n_d, $dn/d\omega$, and to the frequency bandwidth between the F and C spectral lines, $\Delta\omega_{FC}$:

$$\frac{dn}{d\omega} \approx \frac{n_d - 1}{\Delta\omega_{FC}} \frac{1}{V_d}.$$

(12)

which is valid for the wide range of glasses depicted in Fig. 5 with up to only 5% error. Inserting Eq. (12) into the refractive-index bound of Eq. (7), we can write a bound on refractive index in terms of Abbe number V_d:

$$\frac{(n_d^2 - 1)^2}{n_d(n_d - 1)} \leq \frac{\omega_p^2}{\omega_d \Delta\omega_{FC}} \frac{1}{V_d}.$$

(13)

Figure 5 plots the Abbe diagram [103] of many optical glasses along with our bounds for two representative electron densities, the valence electron density of silicon (2×10^{23} cm^{-3}) and the mean valence electron density of high-index materials shown in Fig. 2 (3×10^{23} cm^{-3}). From Fig. 5(a), there is a striking similarity of the shape of the upper bound and the trendlines for real optical glasses. Moreover, depending on the relevant electron density, the bounds may be quantitatively tight for the best optical glasses. Figure 5(b) zooms out and highlights the high-dispersion (large-Abbe-number) portion of the curve. The trend is very similar to that seen in Fig. 2 earlier: as dispersion increases, the gap between the bound and the refractive index of a real material increases, as the magnitude of the refractive index becomes more sensitive to nonzero spreads of the electron oscillator frequencies.

5.1.4 BANDWIDTH-BASED BOUND

Instead of constraining the dispersion of a material refractive index, one might similarly require the refractive index to be high over some bandwidth of interest. A first formulation might be to maximize the average refractive index over some bandwidth, but this is ill-posed: an oscillator arbitrarily close to the frequency band of interest can drive the refractive index at the edge of the band arbitrarily high, and the average itself can also diverge. In any case, in a band of potentially large dispersion, the *minimum* refractive index over the band is the more meaningful metric, as that will be the limiting factor in the desired optical response. Hence, maximizing the minimum refractive index over a bandwidth, i.e., solving a minimax problem, is the well-posed and physically relevant approach. We can pose the corresponding optimization problem for some bandwidth $\Delta\omega$ around a center frequency ω as:

$$\underset{c_i}{\text{maximize}} \quad \min \frac{1}{\Delta\omega} \int_{\omega-\frac{\Delta\omega}{2}}^{\omega+\frac{\Delta\omega}{2}} \text{Re}\,\chi(\omega')\,d\omega' = \sum_{i=1}^{N} c_i\, h_i(\omega)$$

$$\text{subject to} \quad \sum_{i=1}^{N} c_i = 1, \ c_i \geq 0.$$

(14)

where $h_i(\omega) = \frac{1}{\Delta\omega} \int_{\omega-\frac{\Delta\omega}{2}}^{\omega+\frac{\Delta\omega}{2}} \frac{\omega_p^2}{\omega_i^2 - \omega'^2}\,d\omega'$, and again we are considering only a transparency window in which the material is lossless. (As we show in the SM, none of our bounds change substantially if small but nonzero losses are considered.) The solution to Eq. (14) is a single oscillator, analogous to the solution of Eq. (7). In this case, the optimality conditions imply a single oscillator at the frequency $\omega + \Delta\omega/2$, i.e., exactly at the high-frequency edge of the band of interest. This optimal oscillator then implies a fundamental upper limit on the minimum refractive index over bandwidth $\Delta\omega$ around frequency ω to be (SM):

$$n_{\min} \leq \frac{\omega_p}{\sqrt{2\omega\Delta\omega}}.$$

(15)

Equation (15) fundamentally constrains how large the minimal refractive index can be over any desired bandwidth. The only extra parameter is the material electron density, as encoded in ω_p. The bound increases linearly as the square root of bandwidth $\Delta\omega$ decreases, which can be understood intuitively from the optimal refractive index profile: decreasing the bandwidth $\Delta\omega$ effectively moves the infinitely sharp resonance (characterized by a delta-function Imχ) closer to the frequency of interest, thereby shifting the entire refractive-index spectrum upwards and resulting in higher $n_{\min}$.

Figure 6 shows the refractive index, normalized by plasma frequency, for representative high-index materials in the visible and UV spectrum (over each of their transparency windows), compared to the bounds for three different bandwidths. Some materials like ZnTe and GaN more closely approach the bounds than others like TiO$_2$ and HfO$_2$, which can be traced back to their absorption loss (Imχ) spectrum.

Ideally, the absorption is a delta function situated infinitesimally to the right of the transparency windows for each material, leading to a diverging refractive index at the edge of the transparency window (i.e. the dots for each curve). However, real materials are characterized by broad, smeared-out Imχ and thus deviate from the ideal, single Drude–Lorentz response with infinitesimal loss rate. How much each material falls short of the bound signifies to what extent their Imχ spectrum is, on average, concentrated away from the frequency of interest. One can deduce from Fig. 6 that, for example, ZnTe is characterized by Imχ spectrum focused more towards higher wavelengths relative to TiO$_2$. The bound of Eq. (15) is more closely approachable for materials with a sharp absorption peak situated as close as to the frequency of interest as possible.

5.1.5 BIANISOTROPIC MEDIA

To this point, we have considered only the possible refractive indices of isotropic, nonmagnetic media. Although intrinsic magnetism is small at optical frequencies, the possibility for patterned metamaterials to exhibit significant effective permeabilities demonstrates the possibility for magnetic response to alter the *effective* refractive index. More generally, natural and especially artificial materials can demonstrate extreme anisotropy in their response. In this section we consider the most general class of bi-anisotropic materials, and we outline
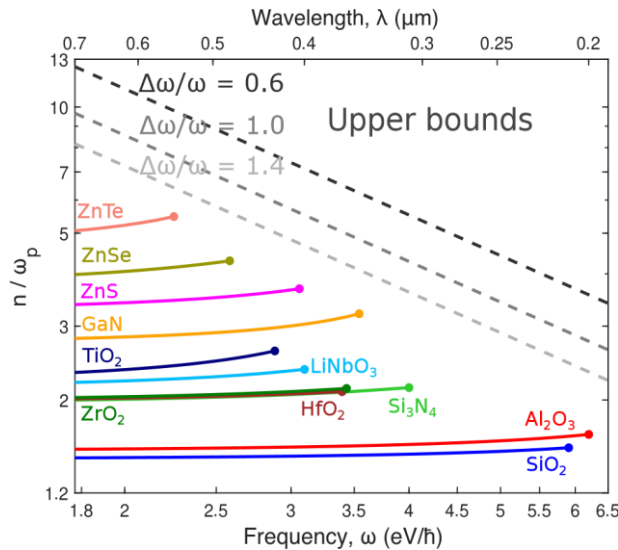
Figure 6. Refractive index normalized by plasma frequency over the UV and visible spectrum, compared to the bounds for three different bandwidths. The dots for each material correspond to the edge of the transparency window, i.e. the frequency beyond which Imχ becomes non-negligible. The plasma frequency for each material is normalized to that of SiO$_2$.

a broad set of conditions under which the refractive index bounds are identical to those of Eqs. (7,8) discussed above.

One possibility is to simply use the refractive-index Kramer's–Kronig relation and sum rule, as described in Sec. 8. IIC. The refractive index itself allows for magnetism and anisotropy, and thus certainly the bound of Eq. (10) would be valid. Yet it turns out to again be too loose, as we will discuss below. Another possibility would be to consider a magnetic-susceptibility Kramers-Kronig relation and sum rule, in analogy to the electric-susceptibility versions of Eq. (1) and Eq. (2). However, there is no known sum rule on the imaginary part of the magnetic susceptibility. This relates to a deep and fundamental asymmetry between

magnetic and electric properties of materials, and to the fact that permeability itself is not a well-defined quantity at very high frequencies [69].

Instead, we exploit an alternative theoretical formulation of bianisotropy developed in Ref. [104]. We consider an arbitrary linear, local, bianisotropic medium, with constitutive relation

$$\begin{pmatrix} \mathbf{D} \\ \mathbf{B} \end{pmatrix} = \begin{pmatrix} \bar{\bar{\varepsilon}} & \frac{1}{c}\bar{\bar{\xi}} \\ \frac{1}{c}\bar{\bar{\zeta}} & \bar{\bar{\mu}} \end{pmatrix} \begin{pmatrix} \mathbf{E} \\ \mathbf{H} \end{pmatrix},$$

(16)

where $\bar{\bar{\varepsilon}}$ is permittivity, $\bar{\bar{\mu}}$ is permeability, $\bar{\bar{\xi}}$ and $\bar{\bar{\zeta}}$ are magneto-electric coupling tensors, and c is the speed of light. Through the transformation properties of Maxwell's equations (TODO: be more explicit), one can show that a local, bianisotropic medium is equivalent to a *nonlocal*, anisotropic, nonmagnetic medium. The nonlocality manifests through a spatially dispersive permittivity that is a function of wavevector $\mathbf{k}$, with the nonlocal effective permittivity given by

$$\bar{\bar{\varepsilon_{nl}}}(\omega, \mathbf{k}) = \bar{\bar{\varepsilon}} - \bar{\bar{\xi}} \cdot \bar{\bar{\mu}}^{-1} \cdot \bar{\bar{\zeta}} + \left(\bar{\bar{\xi}} \cdot \bar{\bar{\mu}}^{-1} \times \frac{\mathbf{k}}{k_0} - \frac{\mathbf{k}}{k_0} \times \bar{\bar{\mu}}^{-1} \cdot \bar{\bar{\zeta}} \right)$$
$$+ \frac{\mathbf{k}}{k_0} \times \left(\bar{\bar{\mu}}^{-1} - \bar{\bar{\mathbf{I}}} \right) \times \frac{\mathbf{k}}{k_0},$$

(17)

where $k_0 = \omega/c$ is the wavenumber in the host medium (taken to be vacuum). In general, Eq. (17) is anisotropic even for isotropic permittivity and/or permeability, due to the wavevector dependence. In this case, we can utilize the fact that Kramer's–Kronig relations and the f-sum rule are valid for each diagonal component and each individual wavevector of a spatially dispersive, anisotropic medium [105, 106] (cf. SM). We can then represent the nonlocal susceptibility, $\chi_{nl}(\omega, \mathbf{k}) \equiv \bar{\bar{\varepsilon_{nl}}}(\omega, \mathbf{k}) - I$, where I is the identity tensor, as a sum of lossless Drude–Lorentz oscillators, exactly analogous to Eq. (4). This is because we can always choose a polarization basis for which $\chi_{nl}(\omega, \mathbf{k})$ is diagonal, since it is Hermitian in the absence of dissipation. (Note that $\chi_{nl}(\omega, \mathbf{k})$ need not be diagonal for all frequencies ω and/or wavevectors $\mathbf{k}$ under the same basis. However, we only require that $\chi_{nl}(\omega, \mathbf{k})$ is diagonalizable at a given frequency and wavevector.)

The refractive index of an anisotropic medium is itself anisotropic and depends also on the polarization of the electromagnetic field. Consider a propagating plane wave with wavevector $\mathbf{k} = \frac{n\omega}{c}\hat{\mathbf{s}}$. The square of the bianisotropic refractive index, $n_{bianiso}$, experienced by that plane wave is one of two non-trivial solutions of the eigenproblem,

$$\bar{\bar{\varepsilon_{nl}}}(\omega, \mathbf{k})\mathbf{e_0} = n^2_{bianiso} B \mathbf{e_0},$$

(18)

where $B = \mathbf{I} - \hat{\mathbf{s}}\hat{\mathbf{s}}^T$ and $\mathbf{e_0}$ is the corresponding eigenvector that physically represents an eigen-polarization. For any material described by a positive- or negative semidefinite $\bar{\bar{\varepsilon_{nl}}}(\omega, \mathbf{k})$, the (square of) refractive index in Eq. (18) is bounded by the largest eigenvalue of $\bar{\bar{\varepsilon_{nl}}}(\omega, \mathbf{k})$ (we defer the discussion of indefinite $\bar{\bar{\varepsilon_{nl}}}(\omega, \mathbf{k})$ to the end of this section). Choosing a polarization basis for which $\bar{\bar{\varepsilon_{nl}}}(\omega, \mathbf{k})$ is diagonal, the latter corresponds to the largest diagonal component of $\bar{\bar{\varepsilon_{nl}}}(\omega, \mathbf{k})$. The largest eigenvalue of $\bar{\bar{\varepsilon_{nl}}}(\omega, \mathbf{k})$ is then equivalent to the square of refractive index with isotropic permittivity given by the largest eigenvalue of $\bar{\bar{\varepsilon_{nl}}}(\omega, \mathbf{k})$, which we denote by $n_{max,iso}$. Thus, we can bound the refractive index for bianisotropic media by that of isotropic media with largest eigenvalue of $\bar{\bar{\varepsilon_{nl}}}(\omega, \mathbf{k})$ (more details in SM):

$$n_{bianiso} \leq n_{max,iso}.$$

(19)

Equation (19) says that, no matter how one designs bianisotropic media, its maximum attainable refractive index can never surpass that of isotropic, electric media as long as $\overline{\overline{\varepsilon_{nl}}}$ (ω,$\mathbf{k}$) is positive- or negative-semidefinite. We can intuitively explain why magnetism, gyrotropy, and other bianistropic response cannot help increase the refractive index. Instead of viewing them as distinct phenomena, it is helpful to view them as resulting from the same underlying matter, which can be distributed in different ways to create different induced currents. For example, one can tailor the spatial dispersion of permittivity to obtain strong magnetic dipole moments, resulting in effective permeability, or alternatively, create strong gyrotropic response. Independent of the resulting bianisotropic response, they can all be described by the effective, nonlocal permittivity of Eq. (17) (with varying degrees of spatial dispersion), which is still subject to our upper bound. Carrying over our bound techniques employed in Sec. 8. II, the maximal refractive index for such $\overline{\overline{\varepsilon_{nl}}}$ (ω,$\mathbf{k}$) is therefore identical to Eq. (7) with dispersion corresponding to the maximum principal component of $\overline{\overline{\varepsilon_{nl}}}$ (ω,$\mathbf{k}$). We show in the SM that most bianisotropic media are captured by positive-definite $\overline{\overline{\varepsilon_{nl}}}$ (ω,$\mathbf{k}$) and also identify particular conditions (for example, magnetic materials with permeability greater than unity) under which $\overline{\overline{\varepsilon_{nl}}}$ (ω,$\mathbf{k}$) must be positive definite. Thus, our refractive-index bound is applicable to generic bianisotropic media that describe a wide range of metamaterials. This is a powerful result suggesting that, no matter how one designs metamaterials to include magnetic, chiral, or other bianisotropic response, the tradeoff between refractive index and dispersion is inevitable.

The class of materials that have indefinite material tensors is exactly the class of *hyperbolic (meta)materials* [107, 108]. In such materials, the bound of Eq. (19) does not apply, and in fact there is no bound that can be derived. Physically, this makes sense: the indefinite nature of such materials leads to hyperbolic dispersion curves that can have arbitrarily large wavenumbers at finite frequencies, and correspondingly refractive indices approaching infinity at particular wavenumbers. Yet such waves are difficult to access as they are well outside the free-space light cone. And, crucially, they are highly lossy: no matter how small the loss is in the underlying material, if one tries to push the refractive index of a hyperbolic-material mode to infinity, the loss rate will also go to infinity, as proven in the SM.

Another case in which our bound does not hold is for gyrotropic plasmonic materials, the simplest example being a magnetized Drude plasma. For such media, the Kramer's–Kronig relations need to be modified to account for the contribution of the pole at zero frequency [62]. Due to this additional term, one can attain large values of permittivity, and hence refractive index, below the cyclotron resonance frequency with low loss far away from resonance. In fact, such response occurs only below the cyclotron resonance frequency, which is typically much smaller than optical frequencies of interest. Also, the cyclotron frequency has to be comparable to plasma frequency to attain large refractive indices, which can be hard to achieve.

5.1.6 DESIGNING HIGH-INDEX COMPOSITES

In the previous sections we showed that for low to moderate dispersion values, natural materials already nearly saturate the fundamental bounds to refractive index. The high-dispersion, high-index part of the fundamental limit curve has no comparison points, however, as there are no materials that exhibit high dispersion in transparency windows at optical frequencies, and hence they are prohibited from reaching the correspondingly high refractive-index bounds. In fact, renormalization-group principles [53] have been used to identify the maximum refractive index in ensembles of atoms, yielding a value 1.7 that is close to those of real materials. Hence, an important open question is whether it is even possible to engineer high dispersion, and the large index that our bounds suggest should then be possible?

Here, we show that composite materials can indeed exhibit significantly elevated refractive indices over their natural-material counterparts. Key to the designs is the use of metals and negative-permittivity materials, whose large susceptibilities unlock large positive refractive indices when patterned correctly. We find that with typical metals such as silver and aluminum, it should be possible to reach refractive indices larger than 10, with small losses, at the telecommunications wavelength 1.55µm. The lossiness of the metals is the only factor preventing them from reaching even larger values; if it becomes possible to synthesize the

"elusive lossless metal," with vanishingly small loss, then properly designed composites can exhibit refractive indices of 100 and beyond.

The theory of composite materials and the effective material properties that they can be achieved has been developed over many decades [112]. Composite materials, or metamaterials, comprise multiple material mixed at highly subwavelength length scales that show effective properties different from those of their underlying constituents. They offer a promising potential route, then, to achieving higher refractive indices through mixing than are possible in natural materials themselves. Bounds, or fundamental limits, to the possible refractive index of an isotropic composite have been known since the pioneering work of Bergman and Milton [109, 110, 113–115] (and even earlier for lossless materials [116]), and were recently updated and tightened [111]. Bounds are identified as a function of the fill fraction of one of the two materials, and comprise two intersecting arcs in the complex permittivity plane. The analytical expressions for the bounds are given in Eqs. (7,79) of Ref. [111], which we do not repeat here due to their modest complexity.

In Fig. 7, we demonstrate what is possible according to the updated Bergman–Milton bounds. At 1550nm wavelength, we consider two classes of composite, one comprising a higher index dielectric material, germanium, with a low-index material taken to be air, and the second comprising a metallic material, aluminum, with the same low-index partner. The Ge-based composite exhibits only small variations in its possible refractive index, the red line, occupying the range between 1 (air) and 4.2 (Ge). By contrast, composites with aluminum can exhibit far greater variability, and potentially much larger real parts of their refractive index. The increasingly large regions occupied by the blue arcs represent the bound regions with increasing fill fractions of the aluminum. Of course, one cannot simply choose the highest real refractive index: most of those points are accompanied by tremendously large loss as well. Part (b) of Fig. 7 zooms in on the lower left-hand side of the complex-n plane, where the imaginary parts are sufficiently small that the materials can be considered as nearly lossless. In that region, one can see that there are still sizable possible refractive indices. The largest loss rate can be defined as a ratio of the imaginary part of n to its real part. The real part determines the length over which a 2π phase accumulation can be achieved, while the imaginary part determines the absorption length, and the key criteria would typically be a large ratio of the two lengths. The black line in Fig. 7(b) maps out a loss-rate ratio of Im$n/$Re$n = 0.05$. One can see that refractive indices beyond 11 are achievable with an Al-based composite.

It is important to emphasize that the refractive indices shown in Fig. 7(b) are indeed achievable. All of the low-loss bounds shown there, and below, arise from a circular arc that can be achieved by assemblages of doubly coated spheres [111]. The inset of Fig. 8(a) schematically shows such an assemblage, comprising densely packed doubly coated spheres that fill all space (cf. Sec. 8. (7.2) of Ref. [112]). Figure 8(a) uses circular markers to indicate the largest refractive indices that are possible, as a function of their dispersion values, for doubly-coated-sphere assemblages of aluminum and gold. Accompanying the markers are solid lines that indicate the electron-density based refractive-index bounds of Eq. (7). One can see that the composites track quite closely with the bounds. Also included are markers for some of the highest-index natural materials, GaN, ZnTe, and GaAs, clearly showing the dramatic extent to which metal-based composites can improve on their natural dielectric counterparts. The figure does not go past dispersion values of 8eV^{-1}, however, as the losses of the composites grow too large in the designs for higher dispersion values. In Fig. 8(b), we map out the largest refractive indices as a function of wavelength that are possible with low-loss composites, with loss rates, as defined above, no larger than 0.05. With such composites, refractive indices larger than 5, 18, and 40 are possible in the visible, near-infrared, and mid-infrared frequency ranges, respectively. Each would represent a record high in its respective frequency range.
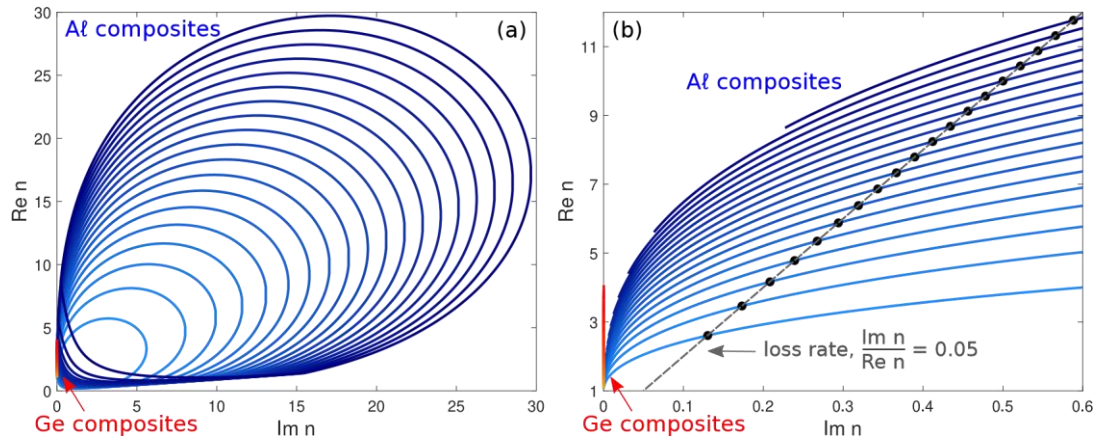
Figure 7. The Bergman–Milton bounds [109, 110], recently strengthened [111], identify the feasible effective material properties of isotropic composite materials (metamaterials). (a) Feasible regions for composites of germanium (red) versus aluminum (blue) at 1550nm wavelength; in the latter case, each enclosed region represents a different fill fraction of aluminum relative to air. The large, negative susceptibility of aluminum enables strikingly large regions of high index, albeit also with nonzero losses. (b) The low-loss portion of the feasible regions.
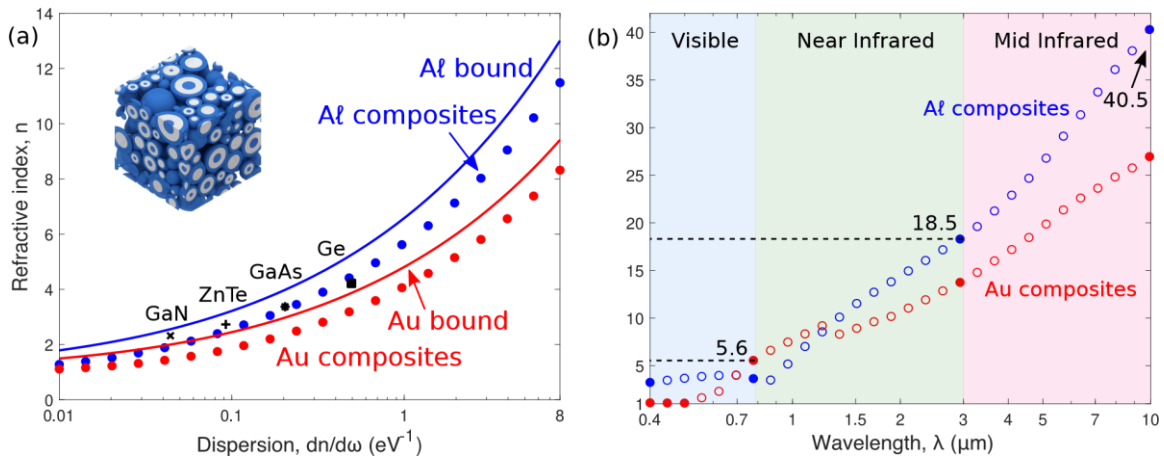
Figure 8. Composites can achieve high refractive indices, at high levels of dispersion, as predicted by our bounds. (a) At 1550nm wavelength, typical high-index dielectrics such as GaAs and Ge have refractive indices approaching 4. By contrast, assemblages of doubly coated spheres (inset) of gold and aluminum can be designed to achieve low-loss, effective refractive indices above 8 and approaching 12, respectively. Moreover, these composites quite closely approach our bounds (solid lines), suggesting that they are tight or nearly so. (b) Maximum low-loss refractive index of gold and aluminum composites as a function of wavelength. Much higher refractive indices are possible at longer wavelengths, as predicted by our bounds.

The large indices of the Al- and Au-based composites can be increased even further with lower-loss materials. To test the limits of what is possible, in Fig. 9 we consider a composite with a lossless Drude metal with plasma frequency of 10eV (corresponding to an electron density of $0.7 \times 10^{23} \, \text{cm}^{-3}$). The updated

BM bound, achieved by the doubly-coated-sphere assemblages, can now exhibit phenomenally large refractive indices, even surpassing longer wavelengths, as predicted by our bounds.

100 in the infrared. As required by our bounds, such refractive indices are accompanied by large dispersion values, and the inset shows the slow cube-root increase of refractive index with dispersion for these composites. Our bound of Eq. (7), applied to the Drude material, now lies along the curve for the composites, showing that the composites can saturate our bounds (and, consequently, that our bounds are tight and cannot be further improved.) There is significant interest in engineering lossless metals [15, 16]; if it can be done, we have shown that refractive indices above 100 would be achievable at visible frequencies.
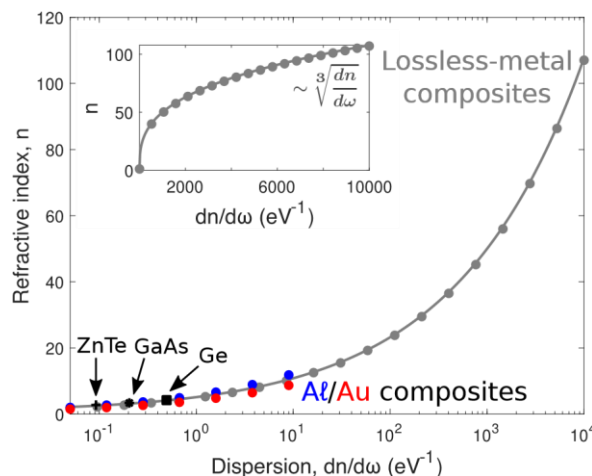
Figure 9. Lower-loss metals would enable even more dramatic enhancements of refractive index. Composites with a nearly lossless metal can be designed to achieve refractive indices larger than 100 at 1550nm wavelength. These composites (circle markers) exactly achieve our bounds (solid line), and require enormous dispersion values to do so, thanks to the cube-root scaling indicated in the inset.

5.2 COMPUTATIONAL FRAMEWORK FOR DESIGN OF MATERIALS

5.2.1 SUMMARY

The intent of the project is to use key principles of Materials Design that we have pioneered in the electronics industry. We had developed several accelerated methods for combining first-principle based ab-initio methods and machine learning or artificial intelligence methods in conjunction with experimental data to design materials. Given the complexity and tight timelines, for this project, Material Alchemy collaborated with a national laboratory and a university. Although we have developed and applied the Material Design framework in industry successfully, this project had aggressive timelines and targets and hence there is likelihood that we will not meet all the proposed items. This was compounded by the Covid19 pandemic which closed down the national laboratories for most of 2020 and constrained access to the universities. Our project summary is given below.

We have specifically demonstrated that chalcogenides and perovskites as bulk materials that can exhibit higher refractive indices ($> RI = 10$) with appropriate engineering of several aspects of the materials. Our hope is that the principles as an outcome of the product will help further progress on down selecting and designing material classes for the specific high RI on bulk materials.

The research that has exhibited as giant Refractive Index (RI) by Di Mei et al in 2018 has the chemical structure of $K_{0.997} Ta_{0.64} Nb_{0.36}:Li_{0.003}$ (KTN:Li) perovskite. With this as background our intent was to use existing literature data and a variety of modeling and computational methods to further the understanding of how RI can be modulated by chemical and material knobs in bulk materials. The rest of the report is divided into the following sections and is based on the following methodology: 1). Detailed literature review to identify correlations between chemical elements, material chemistry (organic or inorganic), and wavelength dependence; 2). Based on the analysis, identify specific classes of materials for detailed quantum simulation analysis; 3) Use quantum and molecular methods to understand the effect of knobs on RI of specific bulk materials; 4) Combine the different methods to identify design knobs for engineering high RI materials.

In Section 8.2.2, we will expound our analysis of existing experimental data on refractive indices. The data analysis will start from elemental properties of 120 elements of the periodic table. Building upon this, we will analyze functional groups for organic and inorganic materials. In addition, we analyzed thousands of inorganic materials to select classes of simulations for our ab initio simulations. Based on our exhaustive literature search, we have identified specific classes of materials (Chalcogenides and Perovskites), for which we will extend *ab intio* quantum modeling to understand sensitivity of the materials. Further analysis included wave length dependence on refractive indices of the above classes of materials including real and imaginary components of refractive indices of materials. Based on the detailed analysis in the above section, we identified two classes of materials for further analysis.

In Section 8.2.3, we will expound the ab initio quantum simulation analysis to predict the dielectric constant (directly related to the refractive index). The large-scale simulations were done in Oak Ridge and in Caltech using two different methods: Density Functional Theory and Molecular Methods. The simulations were used to study the downs-selected classes of materials based on our Section 2 analysis discussed. The DFT analysis revealed that cations and structure modulate the RI of materials. The molecular analysis was being set up to simulate larger materials with heterogenous interfaces for follow-up project, if funded. This analysis demonstrated the proof of concept and was compared with the detailed ab initio analysis.

In the second part of Section 8.2.3, we discuss the semi-empirical method formalism based on force fields, that was demonstrated for perovskite materials. Initial results seem promising, but further analysis is targeted for future work.

In the last part of Section 8.2.3, we integrate the results from experimental data analysis, quantum simulations and machine learning (ML) to extract correlations for estimating refractive indices. This analysis demonstrated the premise of how ML-based Artificial Methods could be used selectively to help identify further materials with higher dielectric constant.

In Section 5, we conclude the project over this year and summarize the results with specific future directions. These directions include using the method illustrated above to analyze frequency dependence of specific classes of materials, assessing phase equilibria of the materials, and assessing chemical synthesizability of specific classes based on ML/AI formalism.

5.2.2 EXPERIMENTAL DATA ANALYSIS

This section is divided into five subsections. In Section 8.2.2.1, we will discuss our analysis of existing experimental data for atomic properties that correlate with higher dielectric constants. Based on the Lorentz-Lorenz equation that connects the macroscopic RI value of a bulk material to the electronic polarizability and number density N of its molecular constituents. Although the ionic and atomic components contribute to the RI and dielectric constants, the static polarizability calculations can be viewed as a lower bound for the frequency-dependent values in the visible range.

In Section 8.2.2.2, we study organic molecules and the primary functional groups and their correlation with the Refractive Indices. The different chemical fingerprints that contribute to higher RI in organic compounds including polymers helped in understanding chemical and structural characteristics that contribute to the RI.   Polymer−inorganic hybrid materials were our focus because of two specific reasons: 1) they have combinations of mechanical, thermal, magnetic, optical, electronic, and optoelectronic properties when compared to the corresponding individual polymer or inorganic component; 2) Perovskite classes of materials are among the higher RI materials are used in other applications (photovoltaics) are bonded with organic molecules. For this analysis, we used existing RI data for 127 organic compounds and 110 polymers.

In Section 8.2.2.3, we analyzed RI of bulk inorganic materials. We evaluated existing RI data for a wide variety of inorganic materials: 1) Binary Compounds. RIs of elements, such binary compounds as halides, oxides, chalcogenides and pnictides hydroxides, cyanide salts of metals; 2) Ternary or Complex Halides and Oxides; 3) Silicates and Germanates; 4)   Oxygen-Containing Salts; 5) Coordination Compounds. of Group 11–14 Metals; 6) Coordination Compounds. of d- and f-Metals.

In Section 8.2.2.4, we identify wave length dependence of the materials. Since practical importance to the materials. As the refractive index is determined by the interaction of the material with the electric field of an electromagnetic wave that propagates through the material, studying the imaginary part is critical, since it describes the decay of the incident electric field's amplitude inside the materials

5.2.2.1   CHEMICAL ELEMENTS

The research that has exhibited as giant RI by Di Mei et al in 2018 has the chemical structure of $K_{0.997}$ $Ta_{0.64}$ $Nb_{0.36}$:$Li_{0.003}$ (KTN:Li) perovskite. To identify the fundamental material characteristics that contribute to the Refractive Index, we have been reviewing the literature. As mentioned previously, Lorentz-Lorenz equation connects the macroscopic RI value of a bulk material to the electronic polarizability and number density N of its molecular constituents. This in turn, depends on the accessible excited states for the electrons and the asymptotic value of RI closer to the static polarizability. Generally, the RI variation is relatively small in the visible range. Although the ionic and atomic components contribute to the RI and dielectric constants, the static polarizability calculations can be viewed as a lower bound for the frequency-dependent values in the visible range.   There is another critical reason for examining the effect of components.

We have collected empirical and theoretical data for the static polarizabilities of 120 elements of the periodic table. Polarizabilities have units of volume, and the proportionality between atomic polarizability and volume is reasonably understood in terms of nuclear charge. The data comes from a combination of experimental results and theoretical calculations from literature. Many of the theoretical calculations especially for the f-orbital elements were based on Dirac equation-based theory for relativistic corrections. The intent of this analysis is many-fold:

1. This helps compare the static polarizability with the perovskite compound used to demonstrate giant refractive index in 2018;

2. It will identify potential elements that can provide higher RI;

3. Provide the basis for the electronic structure analysis based on higher polarizability elements;

4. it was expected to help understand the correlations between bulk material properties and elemental properties.

We have plotted the static polarizabilities of the whole periodic table of elements going from highest to lowest static polarizabilities in the figure below. Several interesting characteristics can be observed for

Figure 10, where the elements are given in the Y-axis and the polarizabilities are in the X-axis. In Figure 11, we plot the static polarizabilities as functions of the atomic numbers, along the periodic table. From Figures 10 and 11 the following specific observations can be made. Many of the elements with higher atomic numbers (> 92) are based on theoretical estimates and have been provided for the sake of completeness. As can be seen, these observations indicate a potential design space for elements to make up the materials with higher RIs.
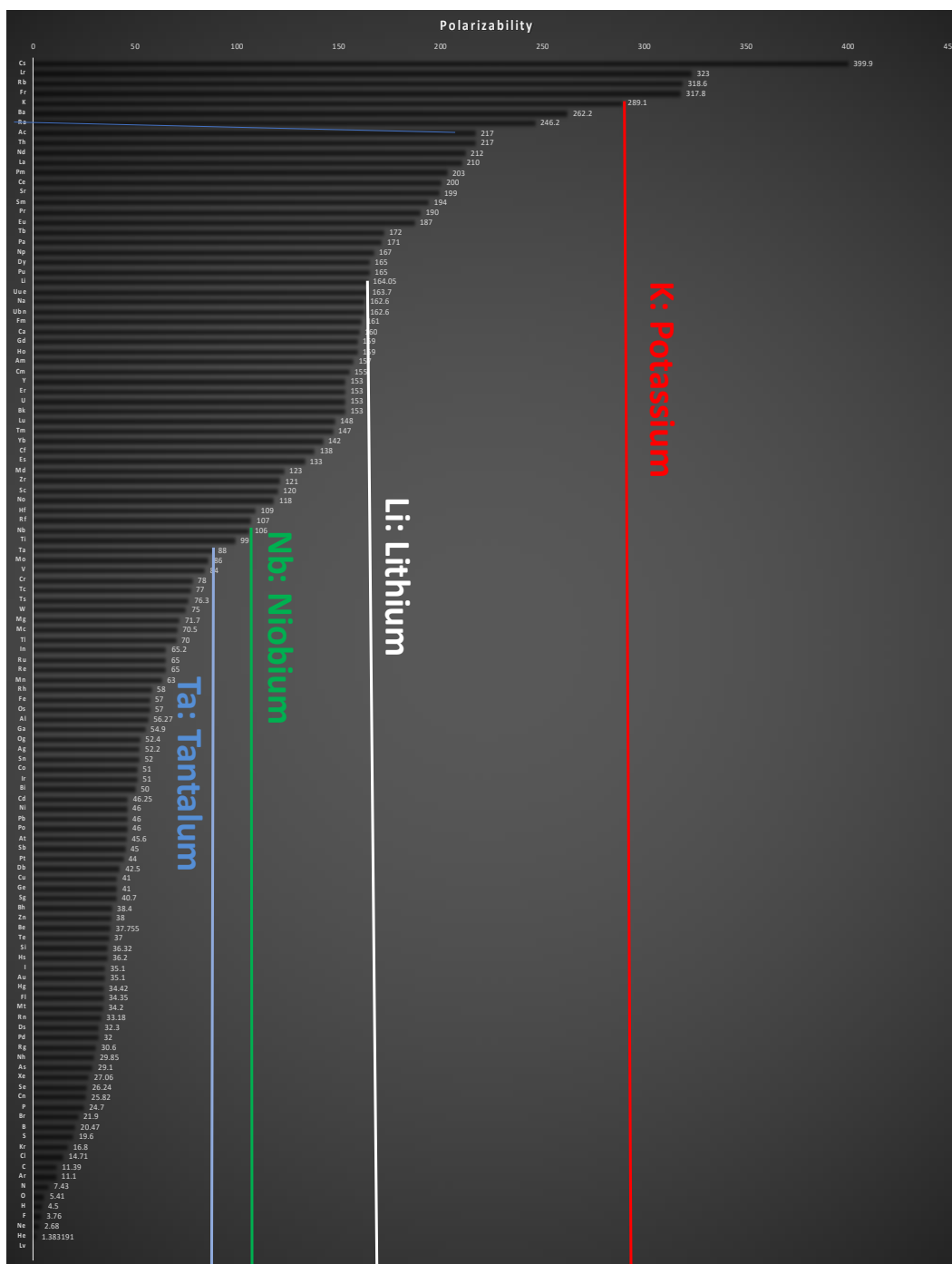
Figure 10. Static polarizabilities of the elements in the entire period table. In order to understand the Giant RI of material K $_{0.997}$ Ta $_{0.64}$ Nb $_{0.36}$:Li $_{0.003}$ (KTN:Li) perovskite, we have marked each of the elements in the figure. Red for K, White for Li, Green for Nb; Blue for Ta.
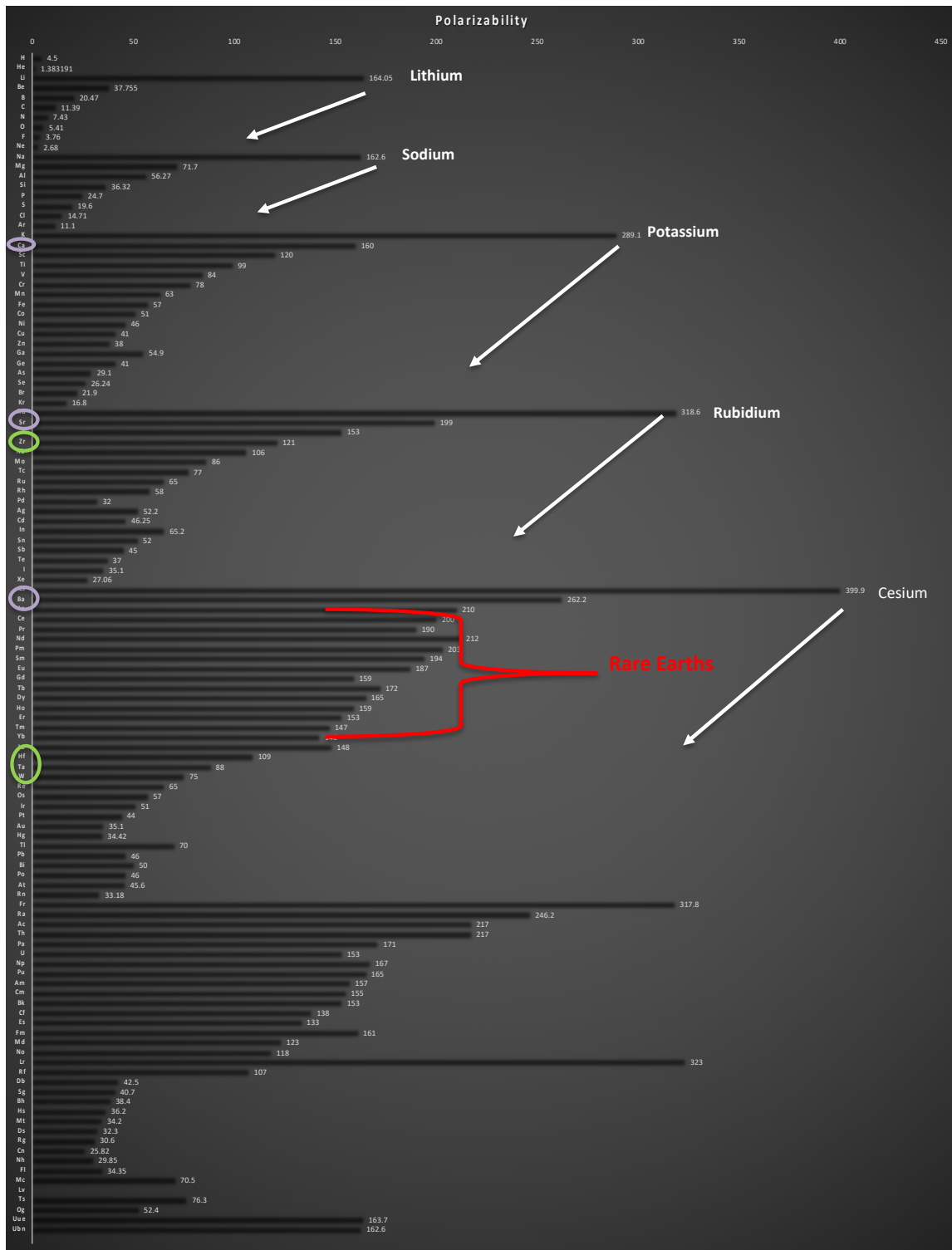
Figure 11. Static polarizabilities of the elements plotted as function of the atomic number.

Specific observations are highlighted below:

1. Of all the elements in K $_{0.997}$ Ta $_{0.64}$ Nb $_{0.36}$:Li $_{0.003}$ (KTN:Li), Potassium has the highest polarizability, followed by Lithium, then Niobium, and Tantalum;

2. There are many elements including from Rare Earths and other groups which have higher polarizabilities than that of the material selected in 2018 paper;

3. Alkaline, alkaline earths, and rare earths all have higher polarizabilities indicating that higher electropositivity (or lower electronegativity) correlates with higher static polarizabilities;

4. Non-metallic elements exhibit lower polarizabilities as given by the elements at the bottom of the plot;

5. For the heavier elements, it appears that large relativistic effects are responsible for their departure from the more systematic behavior exhibited by the lighter elements;

6. The values decrease as we move from Group 1 to Group 8. The highest values are typically associated with alkaline metals. This is illustrated in white arrows as the values go down from Group 1. We can observe an increase in polarizability with increasing period number for the lighter elements in conjunction with a reversal in behavior as the polarizabilities decrease for the heavier elements in these groups.

7. Typically, the values increase down a Group, although this trend changes depending on the electronic configurations as we will see in the next section. This reflects the well-known decrease in size with increasing atomic number for elements in a given row of the periodic table, an effect generally attributed to increasing effective nuclear charge;

8. We have highlighted several groups of elements in circles on the left side of the plot. In addition to alkaline and alkaline earth metallic elements, rare earths, and Group IV (B)-Titanium family of elements. Group 5 (B) Vanadium family of elements have relatively lower variations;

In order to understand the possible cause of these polarizabilities, we examined the electronic configuration of the atomic elements with the higher refractive indices, in Figure 12. Using the *polarizabilities of the elements Potassium and Tantalum as bounding values,* we have listed the electronic configuration of the highest value polarizabilities.

ELEMENT	ELECTRON CONFIGURATION
Cesium	[Xe]6s1
Lawrencium	[Rn]5f147s27p1
Rubidium	[Kr]5s1
Francium	[Rn]7s1
Potassium	[Ar]4s1
Barium	[Xe]6s2
Radium	[Rn]7s2
Actinium	[Rn]6d17s2
Thorium	[Rn]6d27s2
Neodymium	[Xe]4f46s2
Lanthanum	[Xe]5d16s2
Promethium	[Xe]4f56s2
Cerium	[Xe]4f15d16s2
Strontium	[Kr]5s2
Samarium	[Xe]4f66s2
Praseodymium	[Xe]4f36s2
Europium	[Xe]4f76s2
Terbium	[Xe]4f96s2
Protactinium	[Rn]5f26d17s2
Neptunium	[Rn]5f46d17s2
Dysprosium	[Xe]4f106s2
Plutonium	[Rn]5f67s2
Lithium	[He]2s1
Sodium	[Ne]3s1
Fermium	[Rn]5f127s2
Calcium	[Ar]4s2
Gadolinium	[Xe]4f75d16s2
Holmium	[Xe]4f116s2
Americium	[Rn]5f77s2
Curium	[Rn]5f76d17s2
Yttrium	[Kr]4d15s2
Erbium	[Xe]4f126s2
Uranium	[Rn]5f36d17s2
Berkelium	[Rn]5f97s2
Lutetium	[Xe]4f145d16s2
Thulium	[Xe]4f136s2
Ytterbium	[Xe]4f146s2
Californium	[Rn]5f107s2
Einsteinium	[Rn]5f117s2
Mendelevium	[Rn]5f137s2
Zirconium	[Kr]4d25s2
Scandium	[Ar]3d14s2
Nobelium	[Rn]5f147s2
Hafnium	[Xe]4f145d26s2
Rutherfordium	[Rn]5f146d27s2
Niobium	[Kr]4d45s1
Titanium	[Ar]3d24s2
Tantalum	[Xe]4f145d36s2

Figure 12. Electronic Configurations of higher polarizability elements. Potassium, Titanium, and Tantalum are highlighted for comparisons.

There are several key observations that based on electronic configurations that further reinforces the above key points: Criticality of alkaline, alkaline earth, rare earth, and Group 4-B (Titanium-family). The s, d, and f orbitals seemed to contribute to the higher values of polarizabilities. This could be the associated higher electronic densities. However, this also indicates that electronic correlation could play a bigger role in the optical properties, especially in f-orbital electronic elements. It is also important to emphasize that there may be multiple factors contributing to the high polarizability including specific quantum many-body correlations.

5.2.2.2 ORGANIC MATERIALS

In this section, we analyze organic and polymeric materials for various reasons. Polymer−inorganic hybrid materials have become the focus of many research breakthroughs because they have combinations of mechanical, thermal, magnetic, optical, electronic, and optoelectronic properties when compared to the corresponding individual polymer or inorganic component. Perovskites (the class of material studied in 2018 paper) are one such class of materials which are among the higher RI materials are used in other applications (photovoltaics) are bonded with organic molecules. In turn, this will be helpful when we recommend specific material classes for high RI at the conclusion of this project. In addition, this analysis has specific attributes:

1. It should help compare the different chemical fingerprints that contribute to higher RI in organic compounds including polymers.

2. When we go further into inorganic material studies, it will help understand chemical and structural characteristics that contribute to the RI. As chemical bonds can modulate optical properties of organic materials and since organic materials are key part of many integrated material systems, these should provide critical insights.

3. We had examined static polarizabilites of all chemical elements during the fourth month above. By studying specific compounds, we hope to identify the sensitivity of the macroscopic properties to atomic element characteristics.

RI values of polymers typically range from 1.3 to 1.5 in contrast with inorganic materials, although as we will see below, there are new developments in polymers with higher values as we will illustrate below. Methods to increase this include methods to incorporate highly polarizable groups such as incorporation of aromatic molecules, heteroatoms, or organometallics into polymers. In addition, incorporation of metal alkoxides (e.g., TiO_2, Fe_3O_4) or other high-RI molecules (e.g., sulfides) also could lead to higher RIs.

Our analysis of organic materials and polymers has two parts: 1) Analysis of organic compounds to identify key groups that contribute to high RI; 2) Analysis of polymers to identify bonds and chemical structures that contribute to high RI.

5.2.2.3   ORGANIC COMPOUNDS:

The data are from Handbook of Chemistry and Physics and work of Katritzky (1998). We have analyzed data of 127 organic compounds, based on experimental data. The RI of the materials are plotted from the high to low values are plotted below (Figure 13). The higher RI and lower RI materials are given in Tables 2 and 3 below:
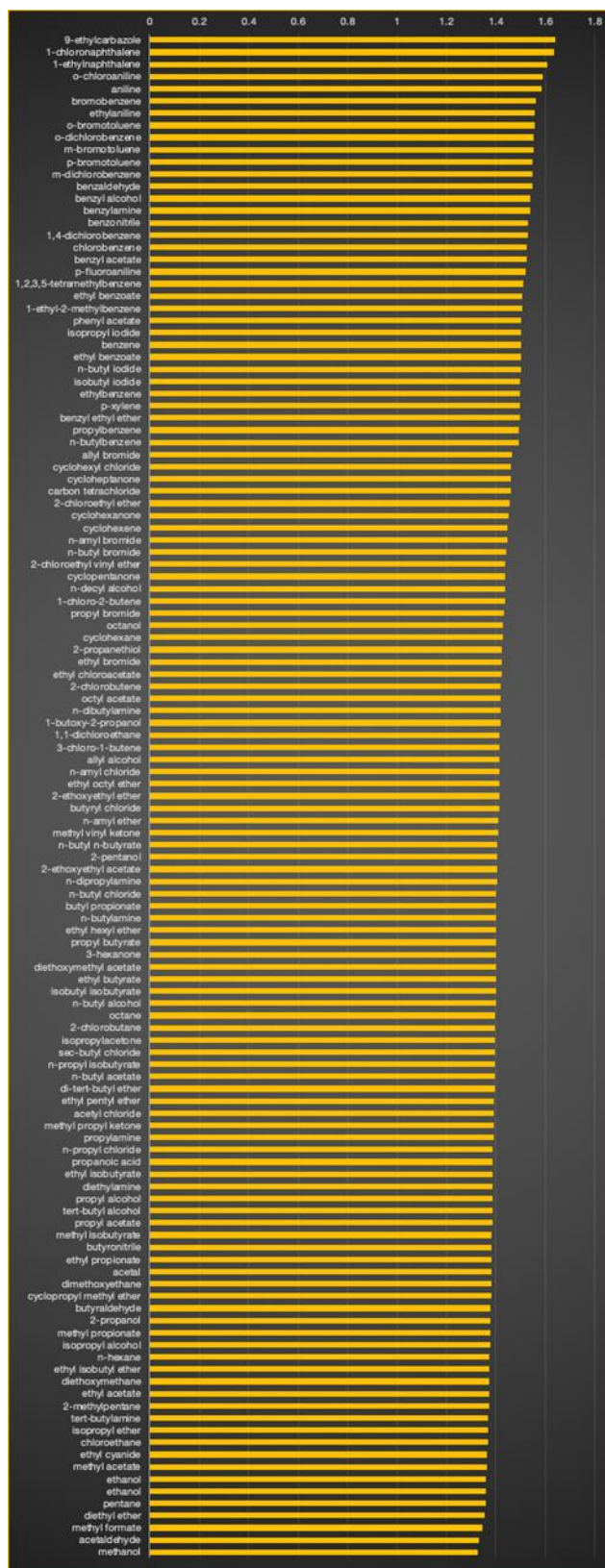
Figure 13. Refractive Indices of 127 organic compounds.

The condensed aromatic groups tend to increase the RI. This can be seen both at the large RI end of the spectrum and the low end of the spectrum. The aliphatic compounds especially halides and alcohols have lower RI compared to condensed aromatic ring compounds like naphthalene. We would like to highlight key aspects of high RI organic compounds:

1. The range of values are essentially between 1.32 and 1.64, limited compared to polymers (as illustrated in the next section);

2. Higher RI structures are essentially aromatic. The highest RI compound is 9-ethylcarbazole as shown in the following structure (Figure 14):
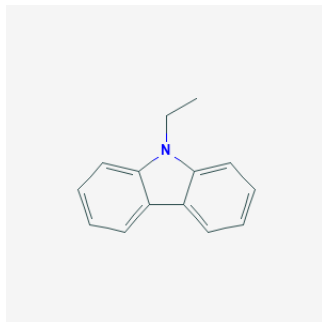
Figure 14. High RI Organic Compound, 9-ethylcarbazole, Two-dimensional molecular diagram.

Table 2. High RI Organic Compounds.

9-ethylcarbazole	1.6394
1-chloronaphthalene	1.6332
1-ethylnaphthalene	1.6062
o-chloroaniline	1.5895
aniline	1.5863
bromobenzene	1.5602
ethylaniline	1.5559
o-bromotoluene	1.555
o-dichlorobenzene	1.5515
m-bromotoluene	1.551
p-bromotoluene	1.549
m-dichlorobenzene	1.5459
benzaldehyde	1.5456
benzyl alcohol	1.5404
benzylamine	1.5401
benzonitrile	1.5289
1,4-dichlorobenzene	1.5285
chlorobenzene	1.5248

Table 3. Low RI Organic Compounds.

isopropyl ether	1.3689
chloroethane	1.3676
ethyl cyanide	1.3655
methyl acetate	1.3614
ethanol	1.3611
ethanol	1.3611
pentane	1.3577
diethyl ether	1.3526
methyl formate	1.344
acetaldehyde	1.3316
methanol	1.3288

They are likely to have N-bonding linked to aromatic rings (e.g. aniline, carbazole). Halides with aromatic rings also seem to indicate higher RI in compounds. It appears that heteroaromatic rings containing −C=N−C− bonds will enhance RI values.

5.2.2.4 POLYMERIC MATERIALS:

Polymers consist of a number of repeating units of building units of monomers. The molecular weight of a polymer molecule is the product of the degree of polymerization and the molecular weight of the repeating unit. The polymer molecules are not identical but are a mixture of many species with different degrees of polymerization, with different molecular weights. We analyzed 113 polymers as shown in the following figures (Figure 15; Tables 4 and 5 indicating high RI and low RI polymers respectively).

Figure 15. Refractive Indices of 113 polymers (RI same scale as that of organic compounds).

Table 4. High RI polymers.

Polymer name	Experiment RI
poly(pentabromophenyl methacrylate)	1.710
poly(N-vinylcarbazole)	1.683
poly(-vinylnaphthalene)	1.682
poly(p-xylylene)	1.669
poly(styrene sulfide)	1.657
poly(-naphthyl methacrylate)	1.630
poly(chloro-p-xylylene)	1.629
poly(4-bromostyrene)	1.620
poly(phenyl -bromoacrylate)	1.612
poly(2-chlorostyrene)	1.610
poly(4-chlorostyrene)	1.600
poly(vinylidene Chloride)	1.600
poly(diphenylmethyl methacrylate)	1.599
poly(p-methoxystyrene)	1.597
poly(N-benzyl methacrylamide)	1.597
poly(p-bromophenyl methacrylate)	1.596
poly(propylene sulfide)	1.596
poly(o-methoxystyrene)	1.593
poly(styrene)	1.592

Table 5. Low RI polymers.

poly(vinyl n-pentyl ether)	1.459
poly(propylene oxide)	1.457
poly(oxyethylene)	1.456
poly(vinyl n-butyl ether)	1.456
poly(oxyethylene)	1.456
poly(ethoxyethylene)	1.454
poly(vinyl isobutyl ether)	1.451
poly(trifluoroethyl methacrylate)	1.437
poly(vinylidene fluoride)	1.420
poly(2,2,2-trifluoro-1-methylethyl methacrylate)	1.419
poly(trifluoroethyl acrylate)	1.407
poly(chlorotrifluoroethylene)	1.390
poly(trifluorovinyl acetate)	1.375
polyoxytetrafluoroethylene	1.350

The bonds of the twenty highest RI polymers are given below in Table 6 below. Note that halogen atoms, especially with aromatic rings, followed by O and S are present in high RI polymers.

Table 6. Bonds in the top twenty high RI polymers.

poly(pentabromophenyl methacrylate)	C(C)(c1c(Br)c(Br)c(Br)c(Br)c1(Br))C	1.710
poly(N-vinylcarbazole)	C(n1c2c(cccc2)c2c1(cccc2))C	1.683
poly(-vinylnaphthalene)	C(c1cccc2ccccc12)C	1.682
poly(p-xylylene)	Cc1ccc(cc1)C	1.669
poly(styrene sulfide)	C(S)C(c1ccccc1)	1.657
poly(-naphthyl methacrylate)	C(C)(C(=O)Oc1ccc2ccccc2c1)C	1.630
poly(chloro-p-xylylene)	Cc1c(Cl)cc(cc1)C	1.629
poly(4-bromostyrene)	C(c1ccc(Br)cc1)C	1.620
poly(phenyl -bromoacrylate)	C(Br)(C(=O)Oc1ccccc1)C	1.612
poly(2-chlorostyrene)	C(c1c(Cl)cccc1)C	1.610
poly(4-chlorostyrene)	C(c1ccc(Cl)cc1)C	1.600
poly(vinylidene Chloride)	CC(Cl)(Cl)	1.600
poly(diphenylmethyl methacrylate)	CC(C)(C(=O)OC(c1ccccc1)(c1ccccc1)	1.599
poly(p-methoxystyrene)	C(c1ccc(OC)cc1)C	1.597
poly(N-benzyl methacrylamide)	C(C)(C(=O)NCc1ccccc1)C	1.597
poly(p-bromophenyl methacrylate)	C(C)(C(=O)Oc1ccc(Br)cc1)C	1.596
poly(propylene sulfide)	SC(C)C	1.596
poly(o-methoxystyrene)	C(c1c(OC)cccc1)C	1.593
poly(styrene)	C(c1ccccc1)C	1.592
polystyrene	C(c1ccccc1)C	1.592

In polymers halogens, oxygen, and sulfurs tend to increase the RI. Consistent with the observations of organic compounds, aromatic groups play a significant role. This can be seen in the lower RI polymers where olefins have lower RIs. We would like to highlight a few key aspects of high RI organic compounds:

1. The range of values are essentially between 1.35 and 1.72, larger compared to organic molecules (as illustrated in the previous section);

2. Higher RI structures are essentially aromatic. The highest RI compounds are poly(pentabromophenyl methacrylate) (RI = 1.7) and poly(N-vinylcarbazole) (RI = 1.68) as shown in the following structures (Figures 16 (a) and 16 (b)). Note that both of them have aromatic rings and also include Br, O, or N.
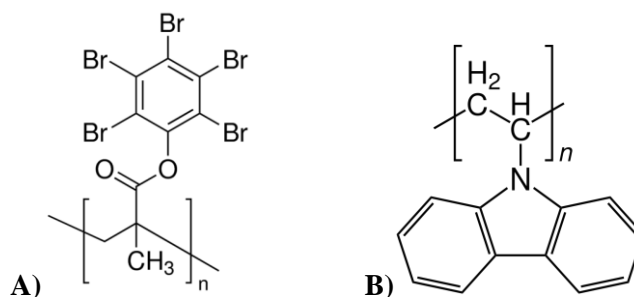
Figure 16. 2D Molecule diagram of poly(pentabromophenyl methacrylate (b): 2D Molecule diagram of poly(N-vinylcarbazole).

In order to understand the bonding effects, chemical bond contributions to the overall RI, are estimated. Comparisons of the additive RI with experimental values are useful to designing materials as we will summarize in the conclusions. We indicate the bond molar fractions from literature in Table 7 below. [118-120]

Table 7. Refractive bond refractions in units of cm³/mole.

Bond	Rd	R∞
C–H	1.676	1.645
C–C	1.296	1.339
C–C (cyclopropane)	1.50	1.44
C–C (cyclobutane)	1.38	1.32
C–C (cyclopentane)	1.28	1.24
C–C (cyclohexane)	1.27	1.23
C_{ar}–C_{ar}	2.69	2.55
C=C	4.17	4.14
C≡C	5.87	5.67
C–F	1.55	1.53
C–Cl	6.51	6.36
C–Br	9.39	8.27
C–I	4.61	14.33
C–O (ethers)	1.54	1.47
C–O (acetals)	1.46	1.43
C=O	3.32	3.24
C=O in MeC(O)R	3.49	3.38
C–S	4.61	4.42
C=S	11.91	10.79
C–N	1.57c	1.49
C=N	3.75	3.51
C≡N	4.82	4.7

The higher values correspond to *triple carbon bonds, aromatic bond*s, carbon-bromine, and carbo-sulfur bonds. If we examine Table 6 above, we can see the same trends are observed in the following polymers: *poly pentabromophenyl methacrylate), poly N-vinylcarbazole, poly-vinylnaphthalene, polyp-xylylene),* and *poly styrene sulfide.* Thus, in polymers and organic molecules, the bond contributions are more correlated with RI than atomic polarizabilities.

5.2.2.5 Bulk Inorganic Materials

Refractive Index data for a wide variety of inorganic materials are analyzed in this section. They consist of: 1) Binary Compounds. RIs of elements, such binary compounds as halides, oxides, chalcogenides and pnictides hydroxides, cyanide salts of metals; 2) Ternary or Complex Halides and Oxides; 3) Silicates and Germanates; 4) Oxygen-Containing Salts; 5) Coordination Compounds. of Group 11–14 Metals; 6) Coordination Compounds. of d- and f-Metals.

The first group of compounds that we analyze are 111 binary compounds. The plots are given with the RI at a specific wavelength of 589.3 nm. The scales are the same for helping with the comparisons. The first analysis will be on halides, followed by chalcogenides, and pnictides.

5.2.2.5.1 BINARY METALLIC HALIDES:

We have plotted the RI of a few metallic halides in Figure 17. The colors denote blue for F, turquoise for Cl, green for Br, and yellow for I. The data indicates that bromides and iodides tend to have higher RI as can be expected from atomic polarizabilities. Most of these compounds are ionic in nature. Another thing to note is that the atomic polarizabilities of alkali metals increased as we go down a group, but in compound form, the trend is not strictly followed. This is due to a variety of factors including that as lattice constant increases, the dielectric constant is expected to decrease.
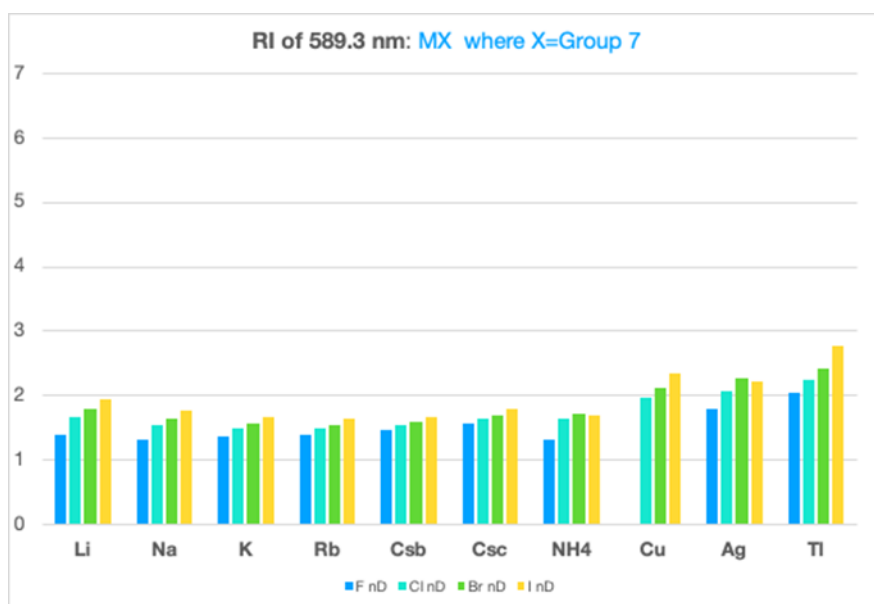
Figure 17. Refractive indices of metallic Halides (F, Cl, Br, I).

5.2.2.5.2 BINARY METALLIC CHALCOGENIDES:

The next set of materials analyzed are on chalcogenides. Here we have plotted the RI of a few metallic chalcogenides in Figure 18. The colors denote blue for O, green for S, red for Se, and dark blue for Te. The RI of MX increases as we go from O to Te. For the metallic cations, it appears that Ge and Sn are indicating higher RI.
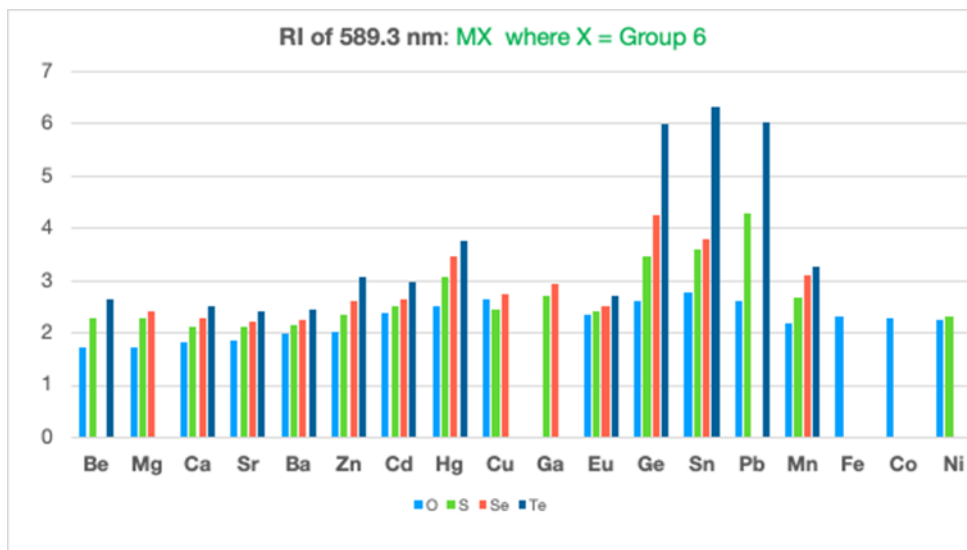
Figure 18. Refractive indices of metallic Chalcogenides (F, Cl, Br, I).

5.2.2.5.3 BINARY METALLIC PNICTIDES:

We have plotted the RI of a few metallic pncitides in Figure 19. The colors denote turquoise for N, yellow for P, pink for As, and green for Sb. The RI of MX increases as we go from N to Sb. For the metallic cations, it appears that Al, Ge and In are indicating higher RI.
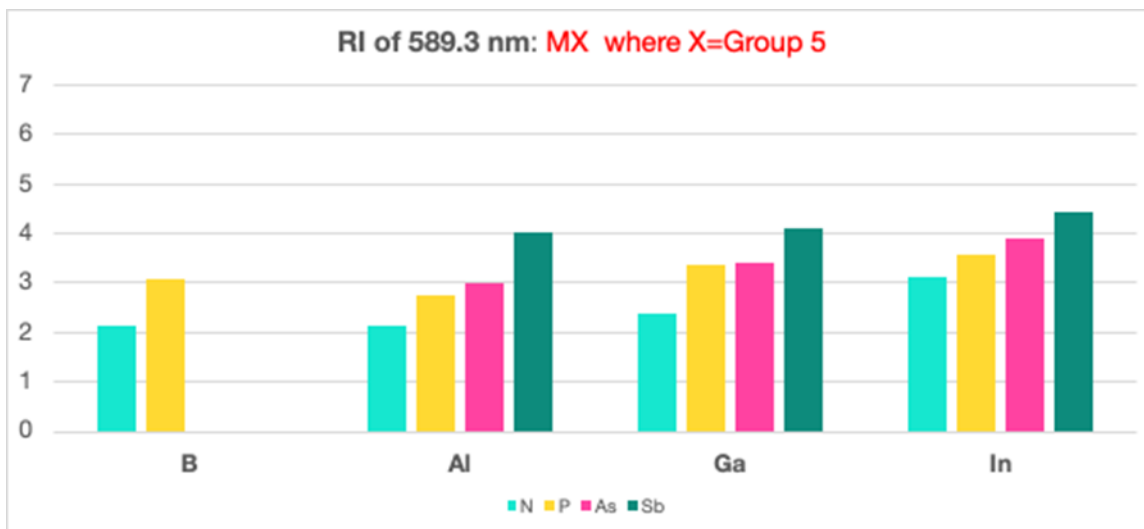
Figure 19. Refractive indices of metallic Pnictides (N, P, As, Sb).

5.2.2.5.4 BINARY METALLIC COMPOUNDS MX₂:

The first group of compounds that were analyzed focused on MX_2 binary compounds. These span all ranges of structures including glass, type of quartz, tetragonal phase, orthorhombic phase, structure of CaF_2, structure of $PbCl_2$, etc. The RIs are plotted in Figure 20. [121-127]
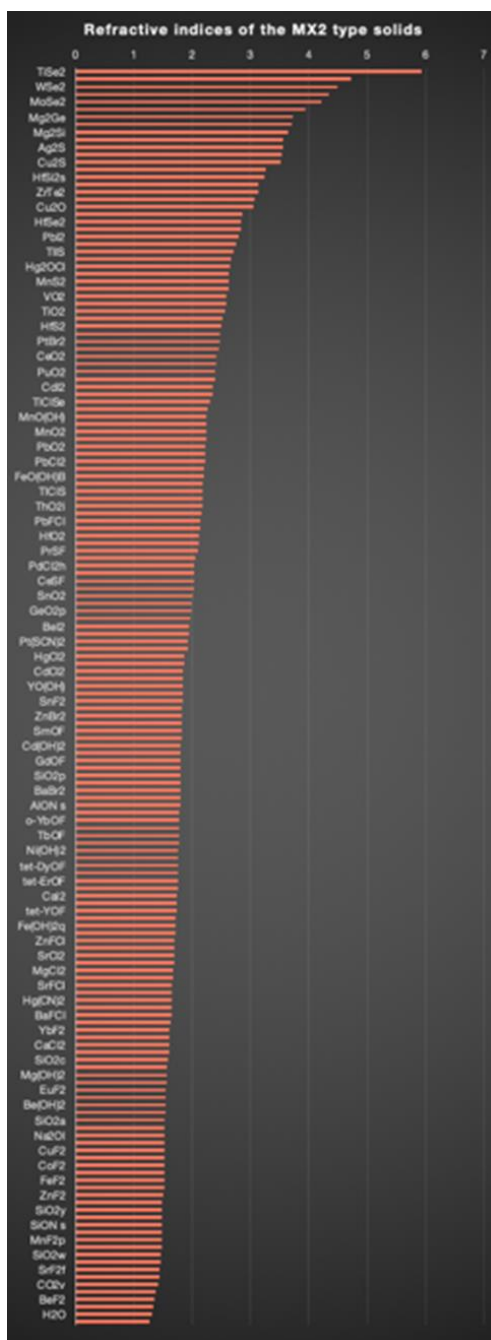
Figure 20. Refractive indices of metallic binary compounds of the type MX2.

Of the 168 materials analyzed, the higher RI material list is given below in Table 8. The specific materials with RI range from 5.92 for TiSe2 to 3.7 for TiS2. Clearly group IV B elements with chalcogenide family are indicating higher RI is reasonably consistent with the analysis of static polarizabilities of elements. Although the highest RI is still below 10, it is important to note that Ti and Group VI element compounds lead to high values of refractive indices.

Table 8. Highest Refractive Index materials from MX$_2$ classes.

TiSe2	5.92
MoSi2	4.73
WSe2	4.5
MoS2	4.34
MoSe2	4.22
Mg2S	3.94
Mg2Ge	3.73
TiS2	3.7

5.2.2.5.5 *BINARY METALLIC COMPOUNDS MX$_3$:*

In this we study MX3 binary compounds and the results are plotted in Figure 21. The halides and oxides tend to indicate higher RI materials, but the values tend to be lower than the previous types of materials.
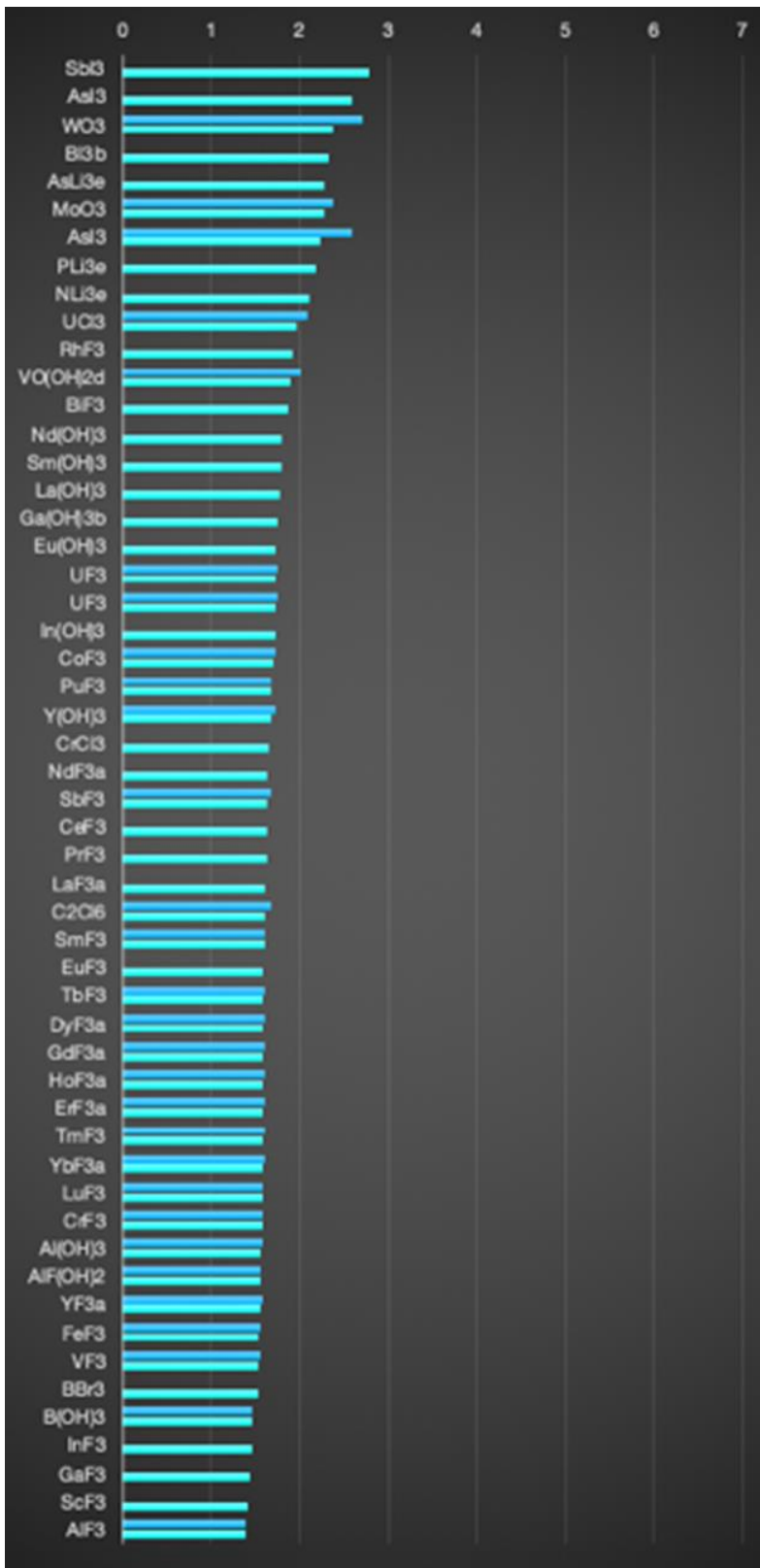
Figure 21. Refractive indices of metallic binary compounds of the type MX₃.

5.2.2.5.6   *BINARY METALLIC COMPOUNDS M_NX_3:*

This class of materials are of the form MnX3 type. The results are plotted in Figure 22. Here the optical properties seem to provide an indication of a higher RI for materials indicating a higher RIs than the previous two classes.
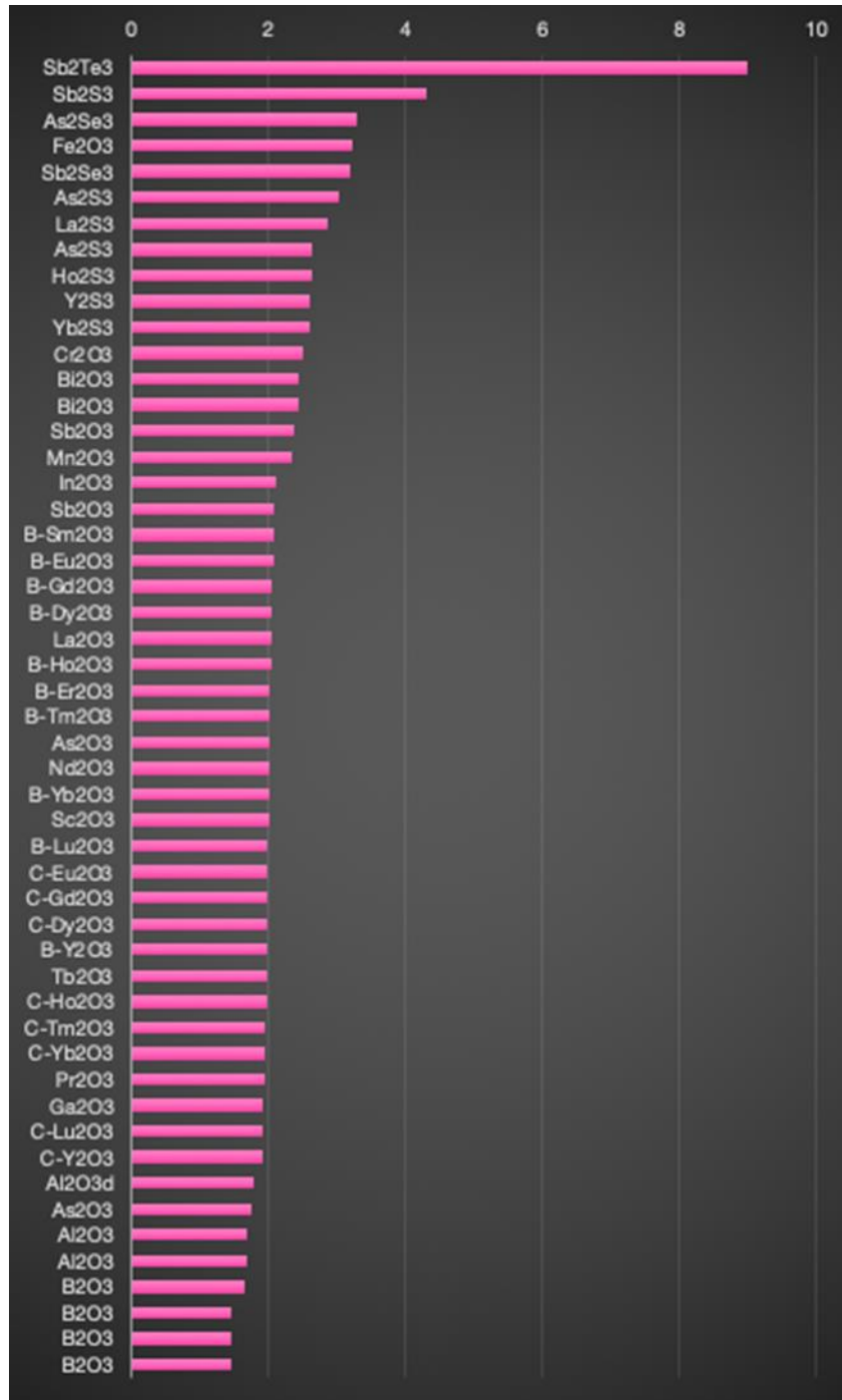
Figure 22. Refractive indices of metallic binary compounds of the type M_nX_3.

We have also identified a higher RI material in Sb_2Te_3. This is chalcogenide type material but with antimony. Antimony telluride (Sb2Te3) has a rhombohedral crystal structure (shown below in Figure 23) and behaves as a semimetal. It is also finding application as a topological insulator and photodetector. Other materials having higher RI continue to be oxides and group 6 elements indicating potential knobs for higher RI.
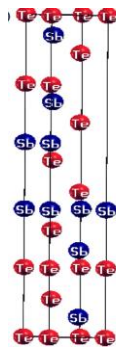
Figure 23. Sb_2Te_3 crystal structure.

5.2.2.5.7   *TERNARY AND QUATERNARY METALLIC OXIDES:*

The first group of compounds that are analyzed are on refractive indices of about 90 materials which consist of complex oxides of Group 13 metals compounded with other metals including rare earths as binary or ternary metallic oxides. The refractive indices are given in Figure 24. In the analysis, although we did not find high refractive index materials, the key trend is the need for rare earth elements (Tb, La, Y etc..) and alkaline earth elements (e.g. Sr) in these materials.

We plot RIs for other complex oxides, we have analyzed 51 materials Ti, V, Nb and Ta at 671 nm in Figure 25. The higher RI is more associated with Pb and Ti. In addition, several interesting results can be observed in these materials, as we elaborate below.

Finally, refractive indices of the 46 complex oxides of Cr, Mo, W, Mn, Fe are examined at 671 nm. The RIs are plotted in Figure 26. Ni and Fe-based oxides lead to materials with higher RIs. Unlike perovskites above, the critical role of transition metals is more evident. We will select the material with the highest RI to indicate the complex band theory. For $NiFe_2O_4$ material, a theoretical band gap of 0.98 eV was determined. The valence band is predominantly formed by O 2p states, while the conduction band minimum of the majority (minority) states is formed by the unoccupied 3d levels of Fe cations on tetrahedral (octahedral) lattice sites.[127] This illustrates the importance of cations (ferrous atoms in this case) in setting the band gap.

Figure 24. Refractive Indices of Ternary and Quaternary Metallic Oxides (Group 13).
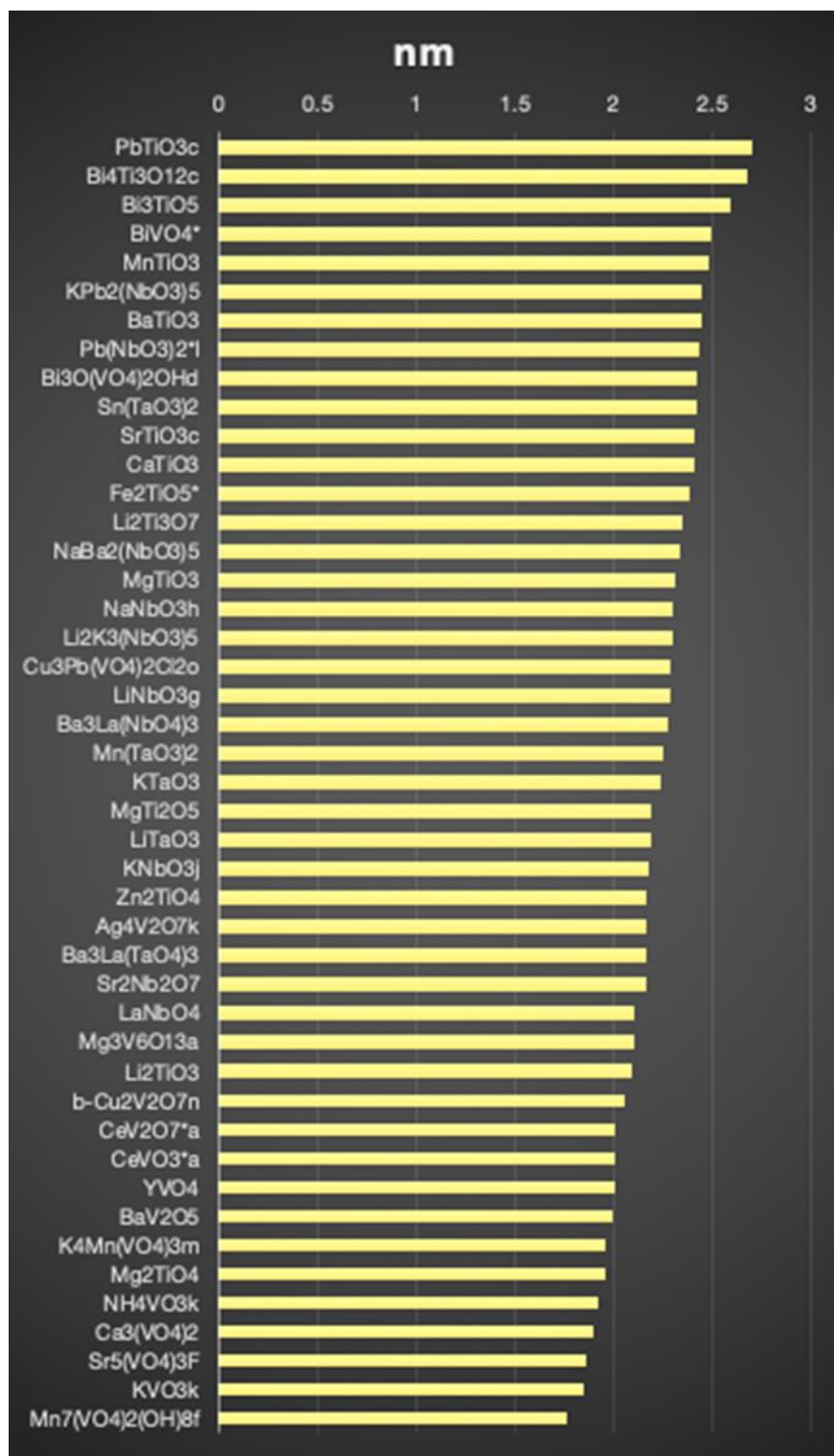
Figure 25. Refractive Indices of Ternary and Quaternary Metallic Oxides (Ti, V, Nb, Ta).
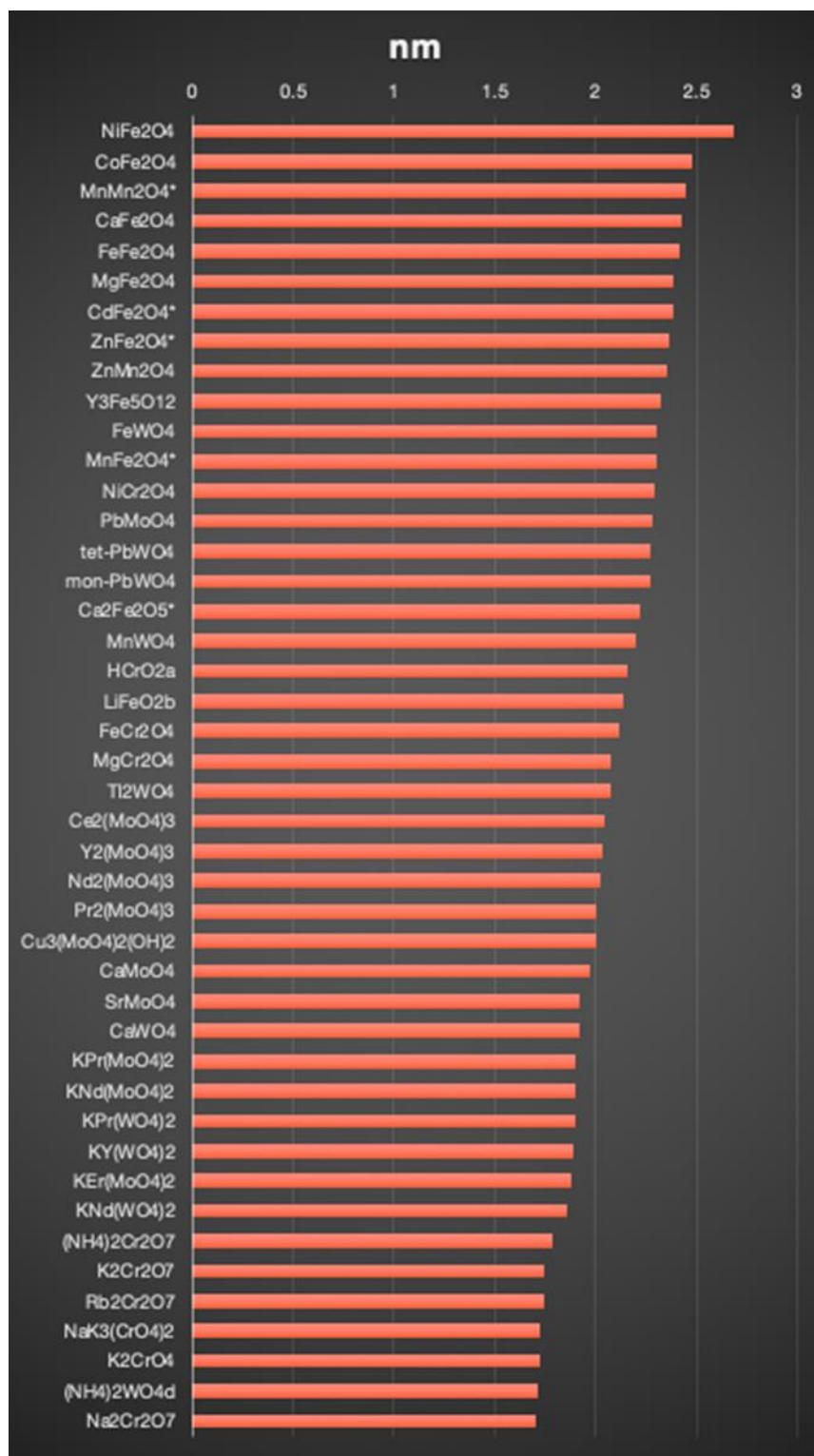
Figure 26. Refractive Indices of Ternary and Quaternary Metallic Oxides (Ferrous Materials).

5.2.2.6 WAVE LENGTH DEPENDENCE

The wavelength dependent complex refractive index can be expressed as, RI = n-i k, where n is the real part that corresponds to the velocity, k is the imaginary part, known as the extinction coefficient. In the following sections, the real (n) and imaginary (k) components are analyzed to develop specific material characteristics that can be optimized across the visible spectrum. As the literature for wavelength dependence is not comprehensive, we have used existing data to identify correlations between the different attributes.

5.2.2.6.1 *REAL REFRACTIVE INDICES:*

The variation of RI with the wavelengths was also analyzed. The wavelength dependent complex refractive index can be expressed as $N=n-ik$, where n is the real part that corresponds to the velocity, k is the imaginary part, known as the extinction coefficient. As the refractive index is determined by the interaction of the material with the electric field of an electromagnetic wave that propagates through the material, studying the imaginary part is critical, since it describes the decay of the incident electric field's amplitude. In other words, a large extinction co-efficient indicates the incident light is absorbed, changing the overall refractive index. The results are analyzed in Figure 27 and Table 9. We calculated the maximum refractive index and the corresponding material and crystal structures for over twenty materials. The highest refractive index is close to the middle of the visible spectrum at 589 nm, with relatively a long tail for infrared end of the spectrum and into the THZ range.
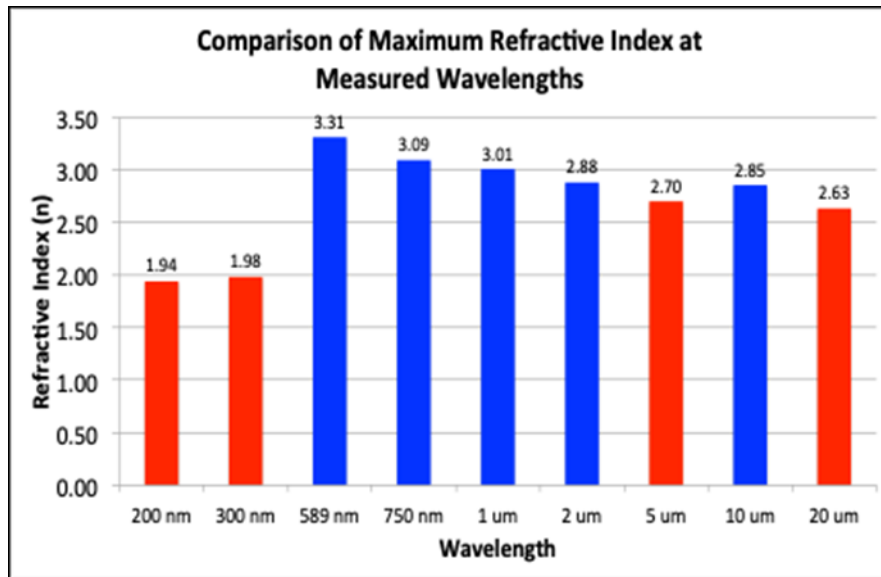
Figure 27. Highest Refractive Indices at different wavelengths.

Two crystal systems of ortho rhombic and tetragonal seem to indicate high RI in the materials that we have examined. The materials (HgS, CsI) are represented in the top with higher RI between 589 and 750 nm. Specifically, the ionic nature of the crystals illustrates one of the specific attributes contributing the optical property. This specific structure-property relationship is an important aspect of the RI of materials.

Table 10. Highest Refractive Index for different wavelengths and the corresponding material and crystal structure.

Wavelength	Max *n*	Material	Syst
200 nm	1.94	CsCl	Cubic
300 nm	1.98	CsI	Cubic
589 nm	3.31	HgS	Rhomb
750 nm	3.09	HgS	Rhomb
1 um	3.01	HgS	Rhomb
2 um	2.88	HgS	Rhomb
5 um	2.70	ZnTe	Cubic
10 um	2.85	HgS	Rhomb
20 um	2.63	CdTe	Cubic

Here we continue our literature analysis of RI as a function of radiation wave length, specifically with focus on K, Ta, Nb, and Li. We have analyzed the elements, highlighting two sets of materials (chalcogenides and perovskites). The elemental RIs are also plotted below (both the real and imaginary components). The red color is the real value of RI and blue is the imaginary or the extinction coefficient. The visible spectrum is delineated by the dotted vertical lines (340-780 nm). The results, shown in Figure 28 and Figure 29, are summarized below.
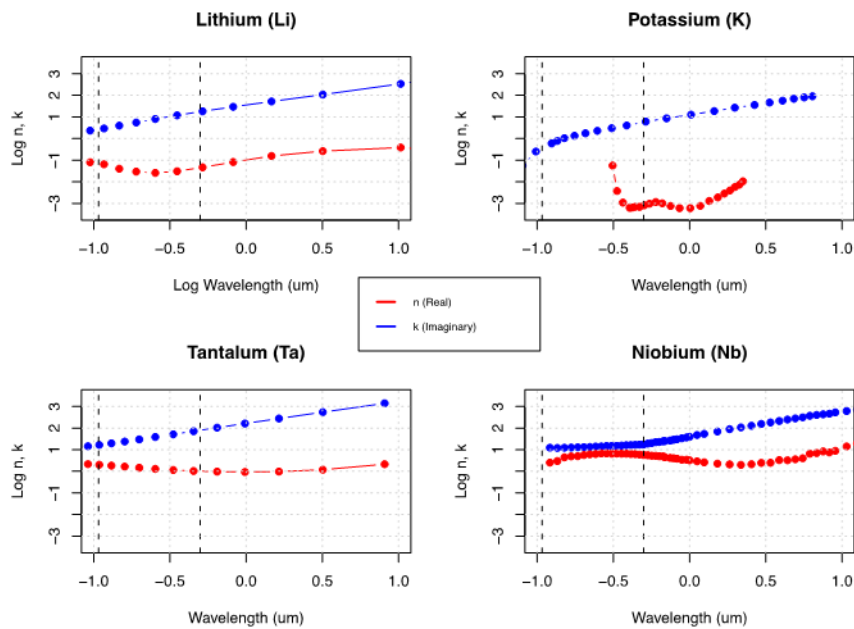
Figure 28. Change in Li, K, Ta, Nb refractive index (log) with respect to wavelength (log).
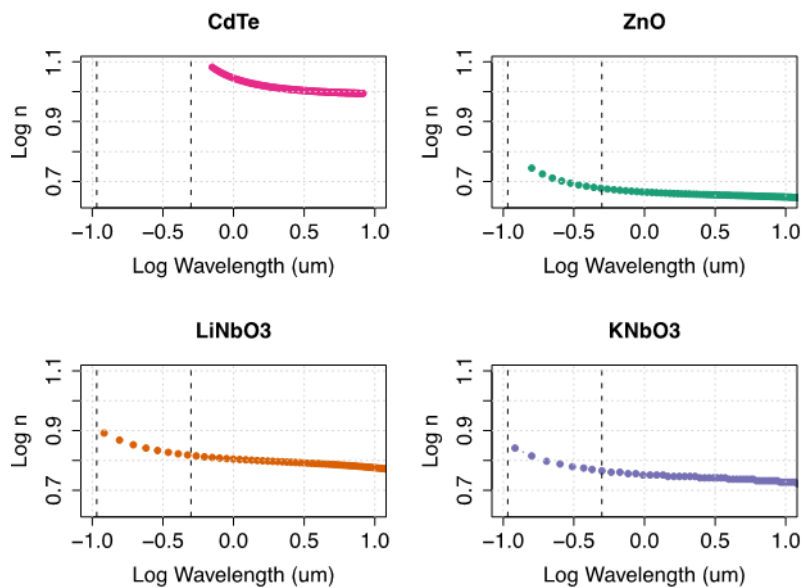
Figure 29. Change in PbTe, KTaO3, LiNbO3, KNbO3 refractive index (log) with respect to wavelength (log).

1. The K atom, which has large polarization also appears to have the largest variation as a function of wavelength, especially in the visible spectrum region

2. These metallic elements have a higher extinction coefficient (imaginary refractive index) compared to the real refractive index at all wavelengths. This in itself indicates the limitations of materials which are more metallic, since a significant part of the measured light will be attenuated or absorbed.

3. Niobium and Tantalum a higher RI compared to other metals over the range of the wave length.

In Figure 28 and Figure 29, the refractive index variation for both chalcogenides and perovskite-type materials are illustrated. The x-axis is given as log (wave length) and the y-axis is the log (n). The visible spectrum is again given as dotted vertical lines.

1. The perovskite materials are relatively flat as functions of wave lengths. The differences between metallic constituents are not significant over the whole range of wave lengths, but do have local variations.

2. The chalcogenide materials have larger variations with RI increasing for smaller wave lengths. The higher RIs are consistent with one of the higher RI materials that we reported earlier in our exhaustive literature search.

3. It is likely that semi metals may also have higher extinction coefficients which are dependent on the band structures. More analysis will be presented in the next update.

Our findings for Li, K, Ta, and Nb indicate that the refractive index is imaginary (absorbed) in the visible spectrum, with the imaginary part increasing for larger wavelengths. As our analysis finds that the refractive index real and imaginary variation changes at low wavelength regimes (e.g. Nb in Figure 28).

5.2.2.6.2 *DISTRIBUTION OF REAL (N) AND IMAGINARY (K) REFRACTIVE INDICES AS FUNCTIONS OF WAVELENGTH:*

The summary of the experimental data of 440 materials for which we analyzed both the variability and the maximum refractive index of the materials are plotted in Figure 30.
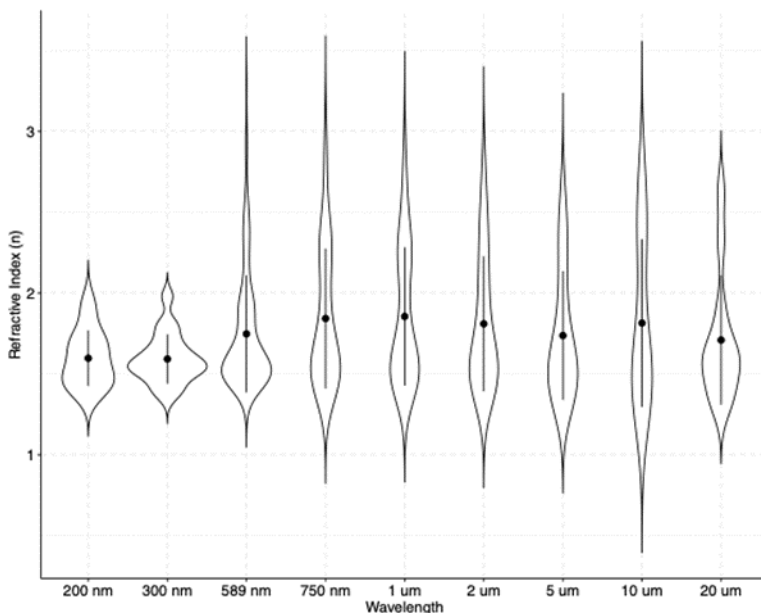
Figure 30. Variation and maximum value of refractive indices of 440 materials.

 A few specific observations can be made based on this analysis:

1. The refractive indices at the smaller wave lengths (towards UV range of the spectrum) have lower maximum values

2. The highest refractive indices are observed at longer wavelengths (towards the IR range of the spectrum)

3. The variations in the data (both due to the range of the values and also due to measurement variations) are higher for smaller wave lengths and are conversely lower for the longer wave lengths.

4. The RI values drop below 589 nanometers indicating both the paucity of experimental data and also the region in which the absorption increases as seen in Figure 30.

We further analyze four representative materials for which experimental data are available on real and imaginary components (Reference list attached at the end of the report). We studied the distribution of refractive index components as a function of wavelength. Figure 31 shows this distribution for 3

chalcogenides (MoS$_2$, MoSe$_2$, WS$_2$) and 1 perovskite (CH$_3$NH$_3$PbI$_3$). Since our previous analysis has predicted that chalcogenides and perovskites are associated with higher refractive indices, we analyzed the imaginary component to estimate how it would affect the high refractive index. While there are some local differences in how the real refractive index changes across wavelengths (e.g., MoS$_2$ n fluctuates between 500 and 750 nm while MoSe$_2$ locally fluctuates between 800 to 900 nm), an overall trend emerges. As Figure 31 shows, the imaginary refractive index is largest at lower wavelengths below ~400 nm, before it declines rapidly at higher wavelengths. This result agrees with the expression for the absorption coefficient, where k is the extinction coefficient and λ is the wavelength.

$$\alpha = \frac{4\pi k}{\lambda}$$

(20)

Since the absorption coefficient determines how far into a material can light penetrate before absorption, the expression above tells us that the absorption coefficient decreases at higher wavelengths, which is consistent with the data shown in Figure 31 and 32. Building upon our previous update, our analysis which predicted high refractive index n at 590-630 nm cannot be solely accounted for by the imaginary component of the refractive index, since this component overall decreases in the 590-630 nm wavelength regime. In fact, as shown in Figure 31, at even higher wavelengths >630 nm, the imaginary component tends towards zero, while the real refractive index remains stable. Overall, this suggests that in chalcogenides and perovskites at higher wavelengths (>600 nm), the overall refractive index is primarily comprised of the real component. [128-130]
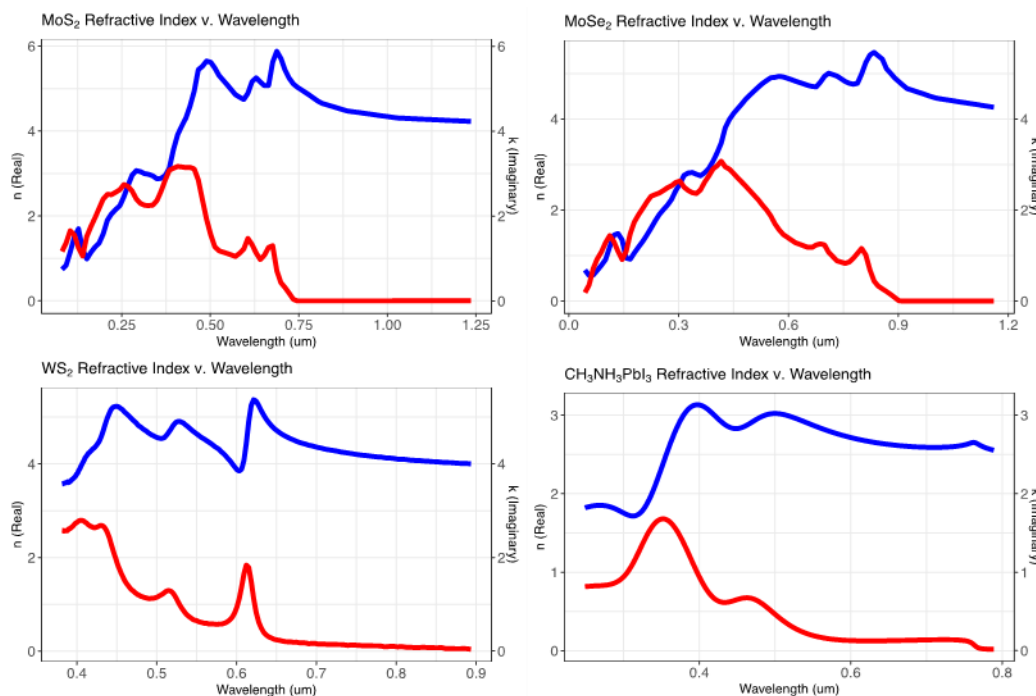
Figure 31. Distribution of real (blue) and imaginary (red) refractive indices as a function of wavelength for 3 chalcogenides (MoS$_2$, MoSe$_2$, WS$_2$) and 1 organic perovskite (CH$_3$NH$_3$PbI$_3$).

In Table 10, we list the maximum refractive index and the band gap of these four materials. The highest refractive index corresponds to the chalcogenide (MoS_2) and the lowest RI corresponds to perovskite ($CH_3NH_3PbI_3$). The correlation with the band gap is relatively modest. It is clear that the chemical nature and the structural details still contribute to modulating the RI as our ab initio calculations demonstrated.

Table 9. Tabulation of the maximum refractive index (RI) vs. band gap.

Material	Max Refractive Index n	Band Gap (eV)
CH3NH3PbI3	3.13	1.57
MoS2	5.88	1.23
MoSe2	5.01	1.09
WS2	5.37	1.32

In Figure 32, we are plotting the cosine or the fraction of the real component. If the cosine component is 1, the refractive index is mostly the real component and conversely, if the cosine component is zero, the radiation is completely absorbed. In Figure 32.a, we plot the cosine component for the four materials and in Figure 32.b, we zoom into the behavior of the cosine component in the visible spectrum.
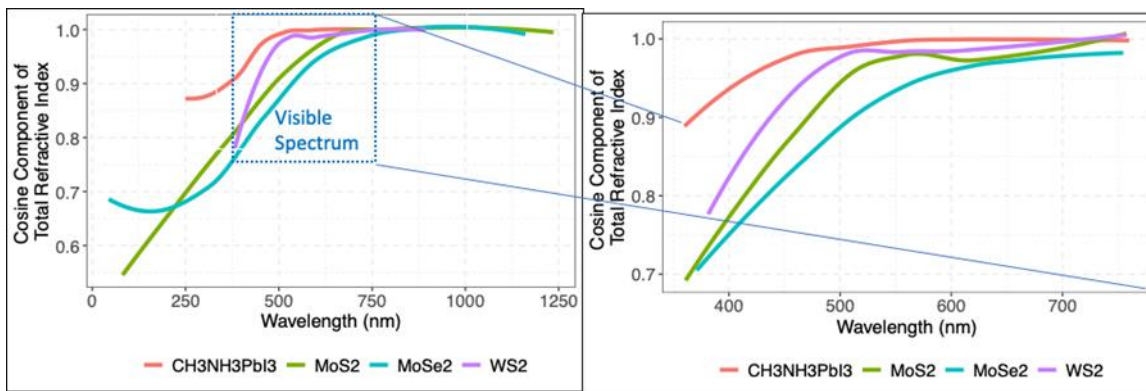
Figure 32. (a) The cosine component or the ratio of real to total refractive index; Figure (b) is magnification of the component for the visible spectrum.

For a practical material design for the refractive index, the material needs to satisfy the following three criteria:

1) high value of RI for the most of the range of the visible spectrum;

2) high value of the cosine component;

3) relatively flat cosine component.

57

In addition, the real component of RI needs to be high in the same range. Of these four materials, the perovskite ($CH_3NH_3PbI_3$) satisfies the first two criteria. However, its maximum RI is 3.13 and hence lower than the other materials. The other material that satisfies all the three criteria is WS_2. It is clear from Table 10 above and the analysis that a finite band gap is needed in reality for the material to exhibit a higher cosine component and a higher RI. It also appears that these two classes of materials have design parameters that could be used to tune the structure composition space to optimize the required refractive index response for high RI materials.

Based on our detailed literature analysis and the original material $K_{0.997}$ $Ta_{0.64}$ $Nb_{0.36}$:$Li_{0.003}$ (KTN:Li), detailed quantum and molecular modeling was focused on Chalcogenides and Perovskites in the following section. In addition, our Machine Learning (ML) analysis was more expansive as the intent was to get precise and accurate correlations.

5.2.3 QUANTUM AND MOLECULAR METHODS-BASED ANALYSIS

There are generally, several methods for using model-based or computational methods to predict optical properties. They are:

1. ab-initio quantum-based models, which combine the authors combine density functional theory, first-principles molecular dynamics and many-body perturbation approaches;

2. Quantitative structural relationships, or semi-empirical methods, which the group contributions method represented by functional forms that relate structural attributes to the materials with the calculated or measured properties. These could include theory-based heuristics, which connects the macroscopic RI value of a bulk material to the electronic polarizability a and number density N of its molecular constituents;

3. Hybrid formalisms which used Machine Learning and combines with data, theoretical-based formalisms, to relate optical properties with structures and chemical composition.

We used two specific quantum-based methods and hybrid technique based on machine Learning for our simulation-based analysis: 1). The first one is based on Density Functional Theory (DFT) simulations in collaboration with Oak Ridge National Laboratory (B. Sumpter), which have been used to simulate single crystals of specific classes of materials; 2). The second one is based on a new force field developed by our collaborator in Caltech (W. Goddard) using general rules for estimating force field parameters based on simple relations; 3). Use of a hybrid method which is based on existing data and a combination of methods (heuristics, machine learning, and semi-empirical methods).

5.2.3.1 <u>DENSITY FUNCTIONAL THEORY</u>

The accuracy of these methods and computational efficiency are limited by the approximation to its exchange-correlation energy. Currently, the local density approximation (LDA) and generalized gradient approximations (GGAs) are used widely mainly due to their efficiency. We have used the recently developed non-empirical strongly constrained and appropriately normed (SCAN) meta-GGA for our analysis that improves significantly over LDA and the standard Perdew-Burke-Ernzerhof GGA for geometries and energies of diversely-bonded materials (including covalent, metallic, ionic, hydrogen, and

van der Waals bonds) at comparable efficiency. The accuracy of these methods and computational efficiency are limited by the approximation to its exchange-correlation energy.
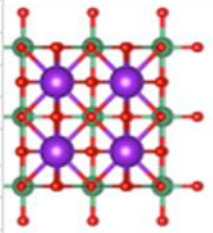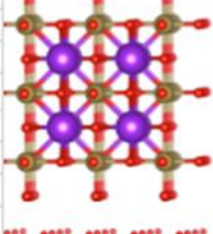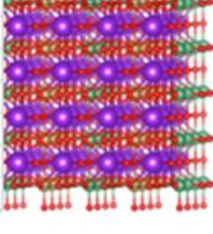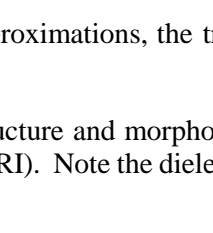
Interactions between ionic species are primarily electrostatic in origin, but can also have a significant component of vdW interactions among highly-polarizable negative ions, for example, making the description of such systems challenging. These situations often arise in ferroelectric materials especially the perovskites, like the prototypical BaTiO3 and PbTiO3, which exhibit spontaneous electric polarization due to structural instabilities at low temperature, and BiFeO3, a multiferroic material with ferroelectric and antiferromagnetic properties. The prediction of structural instabilities from first-principles calculations is extremely sensitive to volume changes, and even small errors of 1-2% in lattice constants obtained from LDA and PBE yield unsatisfactory predictions for ferroelectric materials. PBE, for example, is particularly poor in its description of these materials, as it predicts spurious supertetragonality (too large c/a) in BaTiO3 and PbTiO3.

To address these limitations, we have used the SCAN functions, where the energy differences between the cubic and tetragonal phases are much closer to the B1WC values than either LDA, PBE, or even HSE (Sun et al., 2015).[131]   SCAN also gives more realistic band gaps for these compounds than LDA and PBE, consistent with our findings in Si and other semiconductors. This is possible because the SCAN meta-GGA, like the hybrid functionals, is implemented in a generalized Kohn-Sham scheme in which the exchange-correlation potential is not a multiplicative operator. Hybrid gaps are however more realistic than SCAN gaps. In studies of multiferroics, where late 3d transition metals are usually present to provide the ferromagnetic properties, the Hubbard U is introduced for LDA and PBE to account for the on-site Coulomb interaction, and thus to open the band gap. Table 12 shows that the SCAN band gap is comparable to that of PBE+U with U=2 eV for the Fe atoms. Both SCAN and PBE+U give similar magnetic moments for Fe and comparable polarizations. However, SCAN is much better for the volume. Without being fitted to any bonded system, SCAN have been found to describe multiple kinds of bonding.

The frequency dependence of the dielectric was computed with the independent particle approximation (IPA). This approach tries to get a global description for all times and fields, but it does so in for a static distribution. This is the simplest treatment of the optical response of a crystal, at the level of a full band-structure calculation. Although it is now generally accepted that an accurate quantitative description requires a treatment beyond the independent particle picture, a qualitative agreement between theory and experiment can often be achieved on the level of density functional theory DFT with SCAN. The dielectric constant is related to the refractive index as $\epsilon = n^2 - k^2$, where ϵ is the dielectric constant, n and k are real and imaginary components of refractive index.

The dielectric constants are listed in Table 11. Single crystal simulations were done using VASP with advanced functionals.

Table 10. Quantum-based Simulation of Dielectric Constants of single crystal materials using DFT.

KNbO₃ Tetragonal	
a,b,c	a=4.0, b=4.0, c=4.13
Bandgap	1.86 eV
Dielectric Constant	5
Mass density	4.52 g/cc
KNbO₃ Cubic phase	
a,b,c	a=4.03, b=4.03, c=4.03
Bandgap	2.3 eV;
Dielectric Constant	5.3
Mass density	4.57 g/cc
KTaO₃ Cubic	
a,b,c	a=3.98, b=3.98, c=3.98
Bandgap	3.0 eV
Dielectric Constant	4.38
Mass density	7.06 g/cc
KTaNbO3 Orthorhombic	
a,b,c	a=7.98, b=7.97, c=8.1
Bandgap	2.15 eV
Dielectric Constant	4.4
Mass density	5.72 g/cc

Although these simulations still have limitations based on the current approximations, the trends provide fundamental understanding of the different material characteristics below:

1. Phase/Crystal structures modulate the properties. The crystal structure and morphological phase of the material is a modulator of the dielectric constant (and hence RI). Note the dielectric constant difference between the cubic and tetragonal phases;

2. Moving from Nb to Ta in KTaNbO3 reduces the static dielectric constant, but not large variations.

3. There appears to be an inverse dependence between the bandgap and dielectric constant;

We also show the density of states of a pure crystalline $KTaNbO_3$ material in Figure 33. The key observations are:

4. The large density of states in the valance and conduction band indicates the possibilities of multiple *intraband* transitions

5. The band gap is marked in the figure indicates the dielectric nature of the material

6. The band diagram could be affected by defects as expected in these classes of materials (e.g. O vacancy)
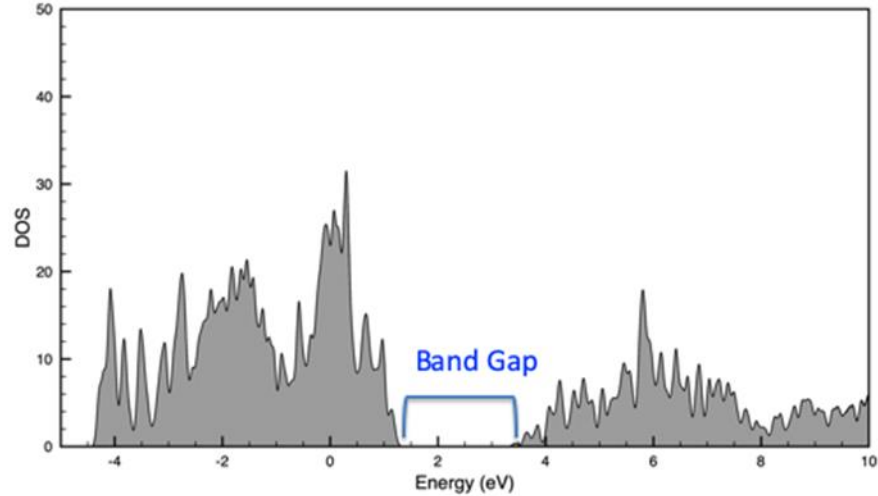
Figure 33. Density of states of a pure crystalline KTaNbO₃ material.

5.2.3.1.1 *CHALCOGENIDE MATERIALS:*

Chalcogenides are covalently bonded materials and, although they may be amorphous or crystalline, they can range from semimetals to semiconductors with band gaps up to several eVs, depending on composition and structure. Bulk chalcogenides are particularly noted for their functionality, with strong, varied responses to optical, electrical and thermal stimuli. chalcogenides exhibit strong and nonlinear properties, and are photosensitive. The lead chalcogenides, PbS, PbSe, and PbTe, crystallize in the rocksalt structure, while in tin telluride (SnTe) a ferroelectric phase transition from a rocksalt structure (13-SnTe) to a rhombohedral structure really occurs. As we go along the following elements, S, Se, and Te shows that bonding changes from molecular, covalent, to metallic. Among these three elements, only Se forms amorphous films and glassy ingots at room temperature.

Of these, we are reporting simulations for $SnTe_2$ and $PbTe_2$ as these classes of materials have been found from our detailed literature research to be capable of high dielectric constant (correlating with high RI). Summary of the results for $PbTe_2$ is given below. The atomic structure used for the orthorhombic simulations is given in Table 12. The relative size similarity between Pb (180-200 pm) and Te (140-202 pm) can be observed. The following are the key conclusions from these analyses:

1) PbTe2 indeed seems to indicate high dielectric constant;

2) Structure seem to be a key modulator for the optical response.

Specifically, the tetragonal structure, with higher density exhibits higher dielectric constant. Although the analysis itself is based on single crystalline materials, the strong modulation of structure will be also evident in the perovskite analysis.

Table 11. Dielectric Constant of two phases of PbTe$_2$.

PbTe$_2$ Tetragonal	
a, b, c	a=7.0, b=7.0, c=8.14
Bandgap	0.017 eV
Dielectric Constant	27.3
Mass density	7.7 g/cc
PbTe$_2$ Orthorhombic	
a,b,c	a=7.7, b=7.7, c=7.7
Bandgap	0.384 eV
Dielectric Constant	13.7
Mass density	6.7 g/cc
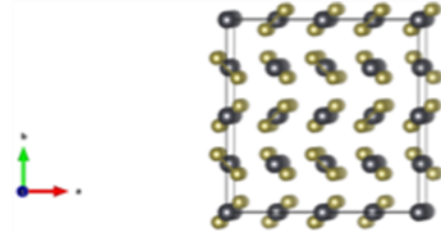
The simulation analysis of SnTe$_2$ in Figure 34. SnTe$_2$ is a semimetal and indicates a higher dielectric constant from the simulations. Specific observations include:

 1) the high dielectric constant for the hexagonally packed structure, with a small bandgap;

2) The density of states (DOS) The observation of the metallic nature is demonstrated. The fermi energy is 6.4 eV.

SnTe$_2$ Hexagonal	
a, b, c	a=4.22, b=3.66, c=12.1
Bandgap	0.004 eV
Dielectric Constant	60.4
Mass density	6.46 g/cc
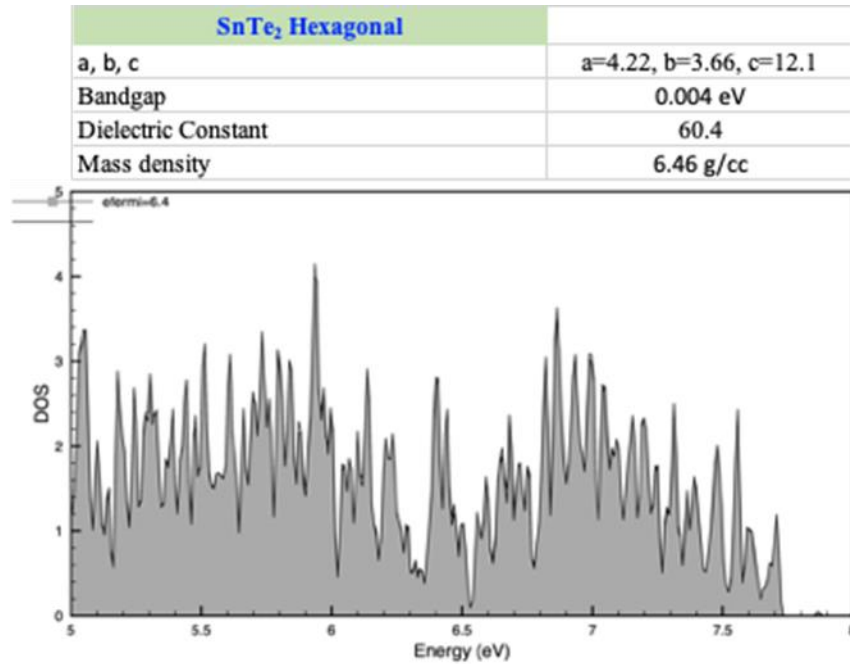
Figure 34. Quantum Simulations of SnTe2 Hexagonal Pure Crystal.

5.2.3.1.2   *PEROVSKITE MATERIALS-DETAILED ANALYSIS FOR K$_X$TA$_Y$NB$_Z$O$_3$:*

We had observed in the previous reports that the O-Ta and O-Nb interactions are critical to the electronic and optical properties. Given the large possibilities for of the KTaNbO3, we have done a systematic analysis of 4 variables: structures, two cations, and anion/defects.   The x, y, and z denote

the composition of the respective elements. The results are combined in the figure below. The summary of this analysis is as follows:

1. For structures, we simulated the same material $KNbO_3$ and $LiNbO_3$ in two different phases

2. For cations, simulations were done for two cases

    a. *Cation 1 substitution*: Compare LiTaO3 with KTaO3

    b. *Cation 2 substitution*: Compare KTaO3 with KNbO3; LiTaO3 with LiNbO3

3. For anion, as O is the only element, simulations were done removing O from $KNbO_3$. A few things need to highlighted for this analysis:

    a. When O is removed from the structure, such as KNbO3, the number of dangling bonds increase and the structure may not be thermodynamically stable. The simulations indicate this in a phase change as indicated in the figure below. It started with the same cell as $KNbO_3$ but the relaxed the cell became triclinic.

    b. In order to study the extreme effect, the simulations resulted in 8 O atom vacancies. For the structure simulated the density of states for the $KNbO_3$ system that has 1/3 oxygen vacancies are also attached below. Although this system has a magnetic moment (~5) and may not be thermodynamically stable, our intent was to find out large modulators.

Table 12. Systematic Computational Analysis of Perovskite with different cations, anions, and structures.

Material	Dielectric Contant
LiNbO3 Cubic	5.2
LiTaO3 Cubic	4.3

Material	Dielectric Contant
$KNbO_3$ (Cubic)	5.3
$KTaO_3$ (Cubic)	4.38

Cation 2 ⟶

Material	Dielectric Contant
LiTaO3 (Cubic)	4.3
$KTaO_3$ (Cubic)	4.38

Cation 1 ⟶

Material	Dielectric Contant
LiNbO3 (Tetragonal)	4.2
LiNbO3 (Cubic)	5.2

Material	Dielectric Contant
$KNbO_3$ (Tetragonal)	5
$KNbO_3$ (Cubic)	5.3

Structure ⟶

Material	Dielectric Contant
$KNbO_3$ Cubic phase	5.3
KNbO2 (8 oxygen vacancies in the cell) Triclinic	44.2

Anion & Structure ⟶

Several key conclusions can be obtained from this analysis (the color of the table in the above figure is also given below):

1. **Structure**: (*red colored table*). This parameter appears to be a strong modulator as seen $LiNbO_3$ (cubic with tetragonal).

2. **Cation 1**: Li with K (*blue colored table*). This parameter appears to be a weak modulator. Although the polarizability of K is higher than Li. This specific observation indicates that the optical property is less modulated by the alkaline cation compared to the structure.

3. **Cation 2**: Nb with Ta (*orange colored table*). The second cation is a stronger modulator as seen by the dielectric constant changing KNbO3 (5.3) when compared to $KTaO_3$ (4.38) and $LiNbO_3$ (5.2) when compared to LiTaO3 (4.3).

4. **Anion/Structure:** O defects (*green colored table*). The simulation analysis indicated this to be the largest modulator. One cautionary note in this regard. Since the number of O vacancies were high, and since the simulations relaxed to an alternate structure, the conclusions need to be understood in this context. The structure and the density of states are also given in Figure 35.
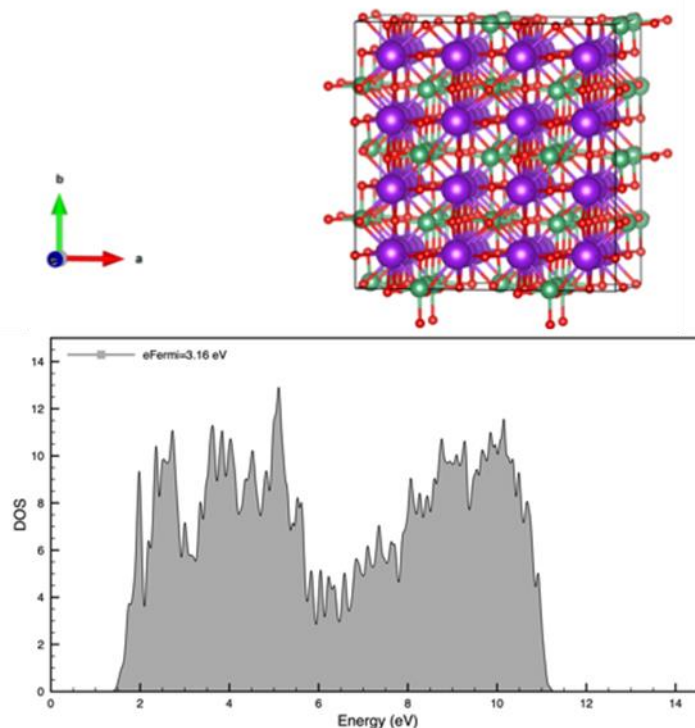
Figure 35. Structure and Density of States of KNbO2 with O defects.

The structure indicates the newly relaxed atomic configuration with O defects. The density of states shows the fundamental change in the electronic and optical properties. The fermi energy for the KNbO2 is 3.16 eV. The interesting observation that the material has become a semimetal indicating the potential for a larger dielectric constant (44.2 based on the simulations). As mentioned above, the O vacancy concentration has been changed significantly, but essentially shows what could be the strongest modulator for dielectric constant (and hence the RI). In addition, the density of states indicate that the electronic and optical properties may be closer to chalcogenides if the O vacancies increase significantly. We intend to complete the analysis of the simulations in the next report.

5.2.3.2   SEMI-EMPIRICAL MOLECULAR METHODS

Although we simulated different materials derived from KTN perovskite to understand structure, two kinds of cations, and anionic defects, we wanted to be able to study both surface structures and also optical response as a function of radiation frequency. In order to address these two items, a new hybrid force functional-based formalism, Polarizable Charge Equilibration Model, was developed by our Caltech collaborator (W. A. Goddard) and compared with more rigorous quantum simulations (but limited in size of systems). This set of fundamental parameters is based only on the element, its hybridization, and connectivity. This new force field is what is being referred here as a Universal force field (UFF). Since the perovskites are strongly polarizable, the interatomic model needed to comprehend the physics and the chemistry of bonding. This is currently done with what is called the Universal Force Field (UFF) which leads to fairly accurate predations of structure for the entire periodic table (up to Lr, Z=103, Z is the atomic number) although it only has 6 parameters per atom. We will briefly discuss the UFF model below.

In order to facilitate studies of a variety of atomic associations, the Caltech team had developed a new force field using general rules for estimating force field parameters based on simple relations. This set of fundamental parameters is based only on the element, its hybridization, and connectivity. The angular distortion functional forms in UFF are chosen to be physically reasonable for large amplitude displacements. The parameters used to generate the Universal force field include a set of hybridization dependent atomic bond radii, a set of hybridization angles, van der Waals parameters, torsional and inversion barriers, and a set of effective nuclear charges.

For the ability to compute dielectric constant of perovskite-type material, the Caltech team replaced the charge equilibration method for predicting charges in the original UFF with a new method (PQEq) [132] that leads to polarization response in excellent agreement with QM, even though PQEq is also very simple with just 4 parameters per atom. The original UFF was for non-reactive systems, using a new way to predicting bond distances and force constants. As such it did not include electrostatic interaction between bonded atoms. For applications to dielectrics, the formalism needed to include all electrostatics including bonded atoms, which required reformulating the bond distance force constant relationships. The PQEq parameters were validated and optimized based on accurate QM polarization energies for many elements of the periodic table including transition metals, main group, and p-block elements.[133-135] The PQEq predictions of interaction energies are observed to be in excellent agreement with QM, much better than other common charge models such as obtained from many of the currently-used interatomic potential methods.

Since our goal was to specifically study complex materials such as $KNbO_3$, $KTaO_3$, $KTa(1-x)Nb_xO_3$ etc, a hybrid method was developed and tested. PQEq was combined with UFF for calculation of dielectric constant properties of complex materials as follows: UFF was used to describe the covalent bonds and angles and van der Waals (vdW) interactions, while PQEq was used to describe the polarization and electrostatic interactions. In this report, we focus on $KNbO_3$ and $KTaO_3$ systems to validate the accuracy of the hybrid force field in computing electronic properties for such complex systems. The crystal structure of $KNbO_3$ and $KTaO_3$ are shown in Figure 36. The crystal structures were minized using quantum mechanics with A) KNbO3 with Pm3m space group and a=4.057 Å and B) KNbO3 with Pm3m space group and a=4.031 Å. The unit cell of each crystal includes 4 atoms.
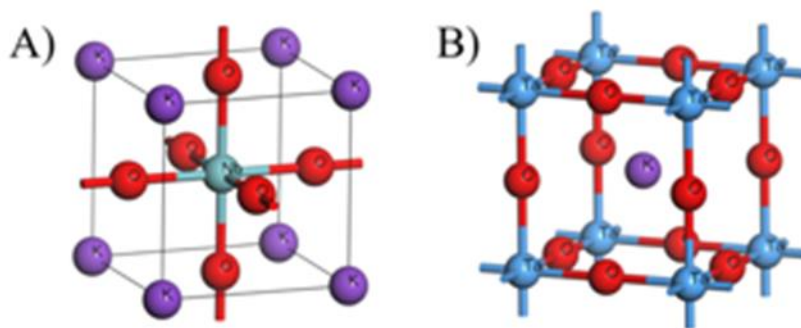
Figure 36. The crystal structure of $KNbO_3$ and $KTaO_3$.

5.2.3.2.1 DIELECTRIC CONSTANT COMPUTATIONS:

The dielectric constant (ε) calculation was added to the PQEq formalism in presence of an external field as shown below.. PQEq parameters used optimized parameters from QM dipole scans for transition metal oxides. [136] The polarization density (P) is aligned with and proportional to the electric field (E_f)

$$P = \varepsilon_0 \chi E_f$$

(21)

The dielectric constant can be obtained as a function of P and E_f given by

$$\varepsilon = 1.0 + c \frac{P}{E_f}$$

(22)

Where c is unit conversion factor. The dielectric property estimates found using PQEq-UFF, were validated with quantum mechanics simulations. Upon minimization at 0K, both structures shrunk by only 3%, indicating good agreement between the experimental and theoretical lattice parameters. Following minimization, density functional perturbation theory (DFPT) to calculate the static dielectric properties of these structures. For $KNbO_3$ the isotropic dielectric tensor the static dielectric constant was estimated to be 6.33. For $KTaO_3$ the static dielectric constant was estimated to be 5.35 (both of these calculations include local field effects at the RPA and DFT levels). These results are given in Table 14.

Table 13. Comparison of dielectric constant values computed by PQEq-UFF with Quantum Simulations.

System	ε (PQEq-UFF)	ε (QM)
$KNbO_3$	7.51	6.33
$KTaO_3$	8.22	5.35

Although these results are encouraging, it is clear that more analysis is needed before applying these newly developed methods to estimate dielectric constant of complex materials including frequency dependence. For the next steps (if the project continues beyond the current phase), the newly developed PQEq-UFF needs to be compared with DFT calculations and with experiments for these materials. As part of our future work, this formalism will be used to compute various properties such as polarization, ferroelectricity, and electric field frequency response for select crystal systems (determined by our detailed literature analysis).

5.2.3.3 HYBRID FORMALISM BASED ON MACHINE LEARNING, SIMULATIONS, AND EXPERIMENTAL DATA

As indicated before, our previous analysis looked at materials properties for 1056 inorganic compounds screened using Density Functional Perturbation Theory, we evaluated the consistency of this approach with other methods of predicting refractive index n and corresponding experimental data.[137] Figure 11 shows

the comparison of the perturbation theory approach from with Wemple and DiDomenico's approach for nine perovskite materials, including $KNbO_3$, $BaTiO_3$, $SrTiO_3$, $RbMnF_3$, $CsPbF_3$, $CsCaF_3$, $RbCdF_3$. [138,139] Based on a single-oscillator model, the semi-empirical Wemple and DiDomenico approach can be expressed for oxide and halide perovskites as follows, where E_g is the lowest direct band gap:

Oxide Perovskites

$$n = \sqrt{1 + \frac{16.64 eV}{E_g}}$$

(23)

Halide Perovskites

$$n = \sqrt{1 + \frac{8.32 eV}{E_g}}$$

(24)

While there are other models for estimating refractive index including the Moss relation based on Bohr's hydrogen model, these often do not accurately capture the energy levels in solids, which is shaped by the specific electronic structure and the structural morphology. Through its semi-empirical approach, the Wemple and DiDomenico approach provides a basic approximation that better accounts for the structural restrictions on energy levels. As shown in Fig. 1, the values between perturbation theory and this semi-empirical model correlate reasonably well (r = 0.97), suggesting consistency between the different approaches.

To further characterize how various material properties, relate to refractive indices, we conducted a data-driven analysis. There were two reasons on us choosing specific data: 1) We wanted to ensure *that the data were consiste*nt as the variabilities in data from different sources were not well-characterized and statistically indeterminate; 2) *The principal variables that modulated the RI had to be material-dependen*t (e.g. molar entropy) and not just based on atomic properties (e.g. polarizability), as we have observed that molecular composition alone is not sufficient to explain the optical response. However, the limitation of this analysis is two-fold: 1) Since the imaginary component of RI is not part of the data, the dissipation component of the RI is need to understand the absorption and transmission components; 2) The material stability, time-dependent response, and the non-linear optical properties are not accounted for in this analysis.

With this as the basis, our analysis studied materials properties for 1056 inorganic compounds screened using Density Functional Perturbation Theory. [140] This method, benchmarked to be more accurate compared to GGA/LDA methods in predicting refractive index from electronic structure calculations, has a 5.7% mean deviation from experiments predicting *n*. Even more, the method is known to accurately rank (ρ = 0.92) the refractive index of materials when compared to the ranking of the experimentally measured refractive indices. With this as the requirement, we evaluated the relation between RI (denoted by n) and each material's band gap and polycrystalline estimate of the dielectric constant. For

each material, we also calculated the molecular weight and the entropy by summing the standard molar entropies of the constituent elements.

To determine if the combination of these features had any relation to the refractive index, we applied principal components analysis. Figure 37 shows the map of the first two principal components and helps interpret the embeddings with respect to the available features. At first glance, the first and second principal component capture 21.6% and 16.21% of the variance in the data. As these components combined capture over 37% of the variance in the data, it highlights that the calculated embeddings can be effectively used to study a significant proportion of the variance in refractive index and its relation with these other material properties.
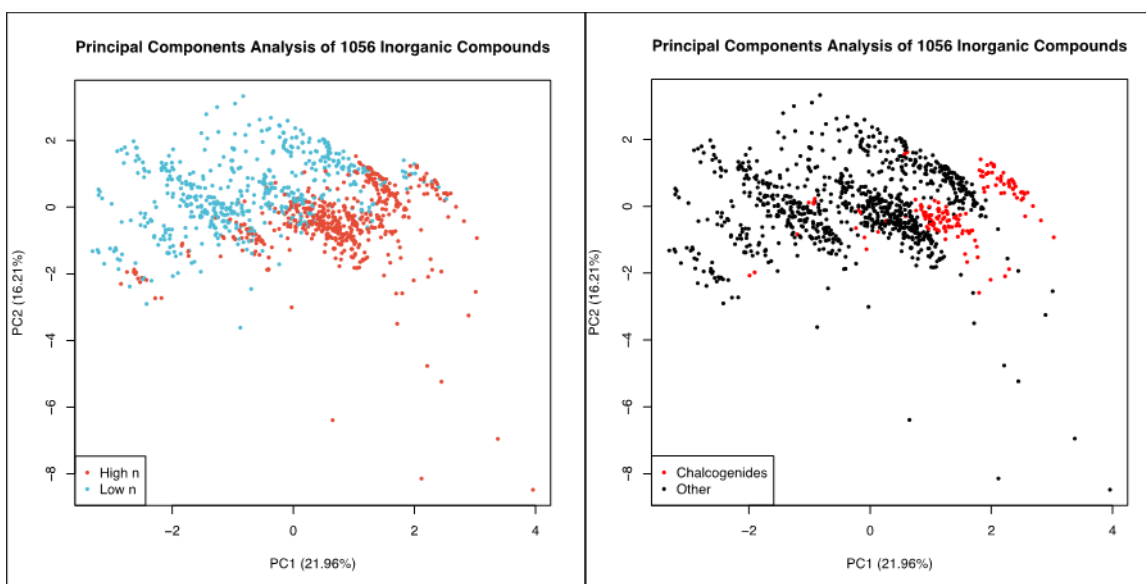
Figure 37. Principal components analysis is used to reduce the dimensionality of 1056 inorganic compounds and study the relation of components to refractive index (left) and material type (right). High RI (*n*) materials, shown in orange, are labeled if its refractive index is larger than 2.19 or the median *n* in this dataset. [139-183]

Figure 37 (left) shows that the combination of these calculated properties (e.g., band gap, dielectric constant, molecular weight, entropy) can separate high *n* materials from low *n* materials. A material was determined to be high *n,* if its refractive index was larger than the median *n* (2.19) in the dataset. Comparing the right and left plots shows that the red points (chalcogenides) largely overlap with the region of materials that are high n, which highlights that chalcogenides tend to have higher refractive indices, consistent with the separate ab initio analysis done earlier and the other literature data. As our previous analysis suggests that metal oxides, chalcogenides (including non-oxides), and perovskites have higher refractive index, Figure 37 (right) looks at the calculated principal components based on material type. Only 14.3% of the materials in the database are chalcogenides (red). Nonetheless, comparing Figure 37 left and right, we can note that the high *n* materials overlap with the chalcogenides, cross-validating our finding from previous updates.

Figure 38 shows a statistical effect plot that visualizes which features have the largest effect or comprise each of the top two principal components. The high refractive index materials are colored in red and lower ones are shown in blue. The loadings plot shows that the first principal component, where materials on the

right have high RI, is explained by the variance in standard molar entropy, whether the material is a chalcogenide, band gap, polycrystalline dielectric constant. In this analysis, if the material is a chalcogenide, it is notable that this feature contributes significantly to the first principal component and is correlated with high refractive index status. Our plot also shows the standard molar entropy inversely correlates with the high refractive index. Other variables such as whether the material is an oxide, perovskite, or ferroelectric contribute less significantly to account for the variance in refractive index status.
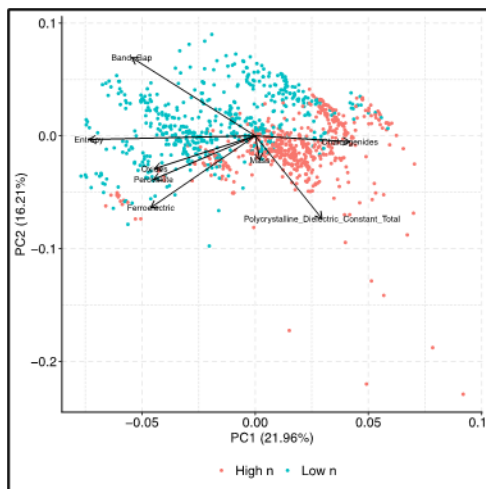
Figure 38. The loadings plot shows the modulation of different variables to the RI.

Figure 39 shows the relation of refractive index with molecular weight (g/mol), band gap (eV), and standard molar entropy (cal K^-1 mol^-1). In this figure, oxides are shown in red, chalcogenides in blue, and others in black.
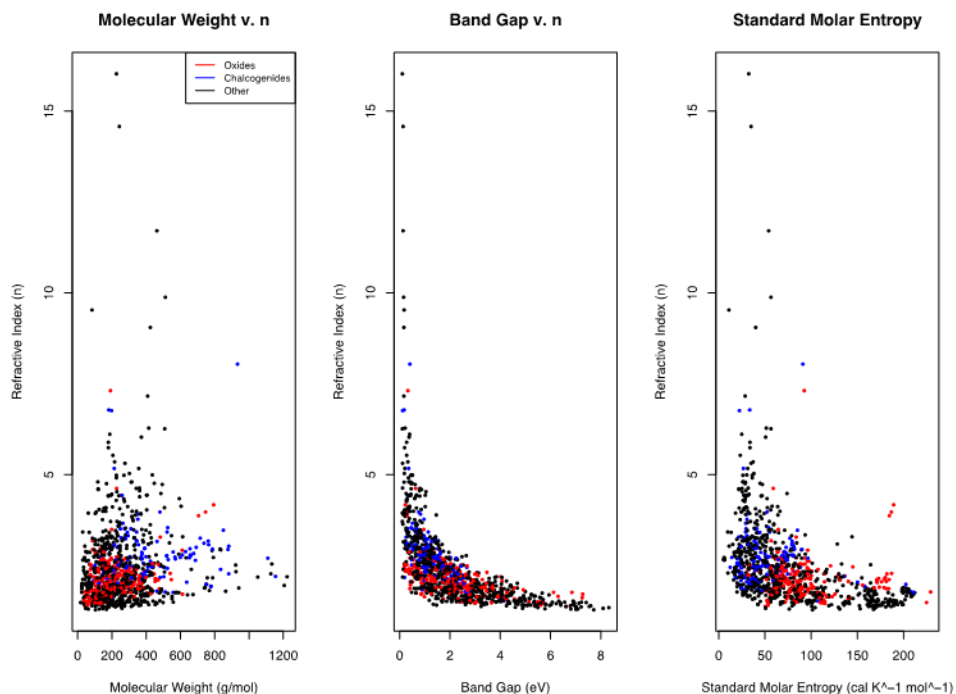
Figure 39. The refractive index is plotted with respect to molecular weight (g/mol), band gap (eV), standard molar entropy (cal K^-1 mol^-1). Our plots show that lower standard molar entropy, lower band gap correlate with higher refractive index.

There are many insights to learn from Figure 39 and here we highlight some of the key ones. First, we note that the high refractive index materials appear to be distributed across various molecular weights.

1. From the plot, we infer that there is no obvious relationship between molecular weight and refractive index.

2. Second, looking at the distribution of band gap to refractive index, a strong inverse relationship emerges. This is a well-known correlation between the dielectric constant and band gaps. All materials with highest refractive index appear to have the lowest band gap, where the first quartile ranges from 0.11 to 0.89. The band gap for the materials with the top 10 refractive indices is shown in Table 15.

3. Three, in studying the distribution of the total standard molar entropy for each material, we find substances with the highest refractive index tend to have lower molar entropies. As various crystal packings likely alter the entropy of each material, as we had reported in our previous analysis, the refractive index can vary according to the crystal structure.

Table 14. Top 10 materials based on highest refractive index. The chalcogenides are shown in blue and oxides in red. These calculations were completed at the optical long wavelength limit (~590 nm).

Formula	Mass (g/mol)	Entropy (cal K^-1 mol^-1)	Band Gap (eV)	Refractive Index (n)
SrAgP	226.46	32.49	0.11	16.03
Li2AgSb	243.50	35.01	0.14	14.58
Sr(CdAs)2	462.28	54.04	0.14	11.71
Ba(CdAs)2	512.00	56.55	0.16	9.88
FeSi	83.93	11.02	0.18	9.53
CoSb3	424.18	39.94	0.17	9.05
Ge2Te5As2	933.02	91.04	0.41	8.04
SrFeO3	191.47	92.57	0.33	7.31
HfSiRu2	408.72	28.54	0.17	7.16
KCuSe	181.60	33.53	0.18	6.78

Finally, Figure 39 illustrates two plots. Fig 39 (a) is based on the above analysis based on experimental data/simulation analysis, and Fig 39 (b) are using the analysis to extrapolate to possible materials that could have higher RIs. Our machine learning analysis seem to indicate specific materials that have potentially high refractive index n. This is also given in Table 14. As mentioned before, the RI does not include the imaginary components, as these datasets did not have both the components.
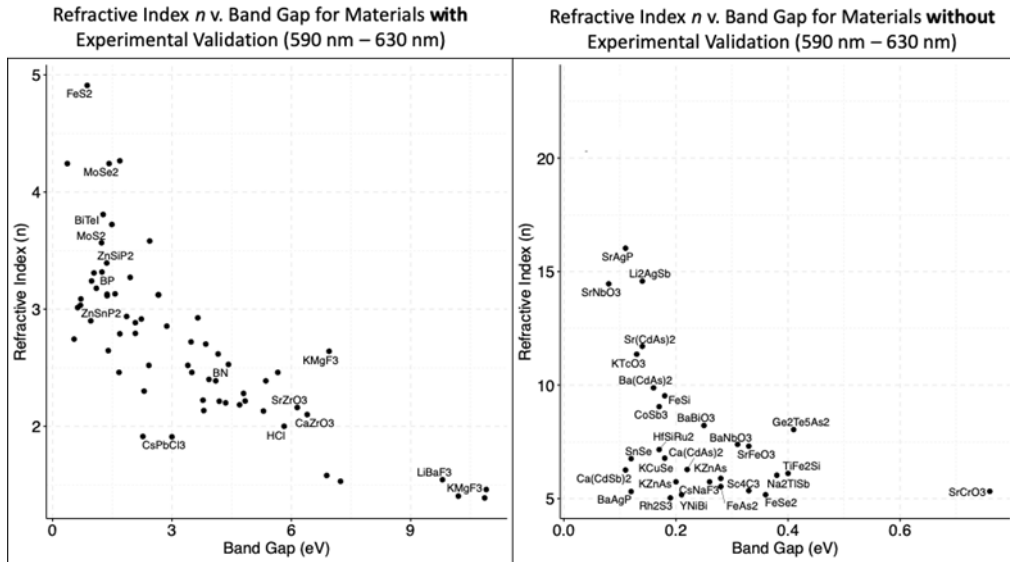
Figure 40 (a) Distribution of Refractive Index v. Band Gap for Materials with experimental validation (left) and (b) predicted high n without experimental validation (right).

5.3 SYNTHESIS PATHWAYS OF THE PREDICTED MATERIALS WITH MAXIMAL REFRACTIVE INDEX

The key questions that were addressed were (1) What are the key optical properties of the GR phase in the KTN:Li perovskite crystals? (2) How are these properties related to the structure of the GR super-crystals?[1] (3) Can the essential optical properties be replicated in a metasurface design, using KTN:Li, some other crystalline material possessing similar long-range correlations, or in a metamaterial basis some other combination of dipole radiators and phase-changing elements.

The crystal-growth technique that creates the supercrystal structure responsible for giant refraction (GR) in Li:KTN (KLTN) was reviewed with the aim of understanding how an analogous metamaterial structure could be designed and synthesized.

We studied the specific organization of the KLTN to elucidate the way in which the periodic modulation of the supercrystal composition leads to the formation of a macroscopic coherent optical state exhibiting giant refraction. The supercrystals have the same sub-nanometer unit cells as the perovskite KTN, but are organized into supercells with alternating regions of high and low niobium density (arising from the off-center crystal-growth process[2] employed), having a superlattice constant of 5.5 µm. The underlying geometry of the supercrystal is illustrated in the Figure 41 taken from one of the key papers from this group.[3]
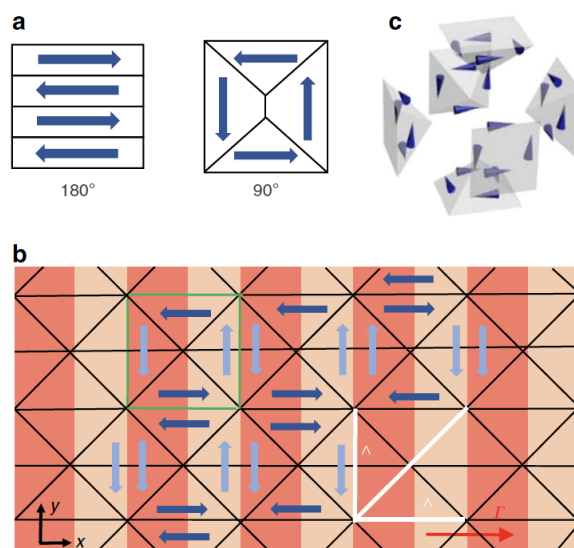
Figure 41. Polar domains in the x-y plane of the supercrystal structure are shown. [184] (a) Adjacent domains in ordinary polar perovskites are rotated either 90° or 180°. (b) In the supercrystal with its built-in ordering in niobium density along the *x* direction, it is the 90° structure that is observed. The supercrystal unit cell is outlined in green in this schematic; the black lines highlight the planes that govern the observed optical refraction, with periods shown in white lines. Light blue arrows mark what are essentially paraelectric domains in the crystal. The period *L* of the superlattice growth along the *x* direction is shown in the lower right. (c) Here the projection of the unit cell into three dimensions is seen in exploded view.

A critical point seems to be that in the supercrystal, neighboring supercells – within which the individual dipoles are locally ordered – are also antiferroelectrically ordered as one crosses domain walls in both 90° and 180° rotation planes. That structure apparently is frozen in just below the critical temperature boundary (the Curie temperature T_c) between the paraelectric and ferroelectric phases of the KLTN and arises after dipolar relaxation in the ferroelectric phase at T_c-2K. Moreover, the observed diffraction anisotropy feature arises because there are no grating planes in the *y-z* face of the crystal.

Thus, the para- to ferroelectric phase transition is an essential feature of the short- and long-range ordering scheme that leads to the GR effect. Since it appears that the critical features of the supercrystal have dimensions ranging from sub-micron to few-micron dimensions, it would seem that fabrication of an appropriate meso- to microscale metamaterial should not be an issue – **if** the appropriate analogs for the

domains can be translated into the appropriate meta-atoms. The design strategy that leads to a viable metalens thus requires a similar combination of local and global ordering in the context of a phase transition.

We considered the thermodynamics of the KLTN to understand how the transition from the disordered paraelectric phase of the supercrystal to the ordered ferroelectric phase leads to the jet-like propagation of an optical signal normal to the KLTN supercrystal surface in the giant refraction (GR) phenomenon. The key underlying point is that this is a second-order phase transition and thus has generic characteristics that are well understood, although application to this specific case will have unique features.
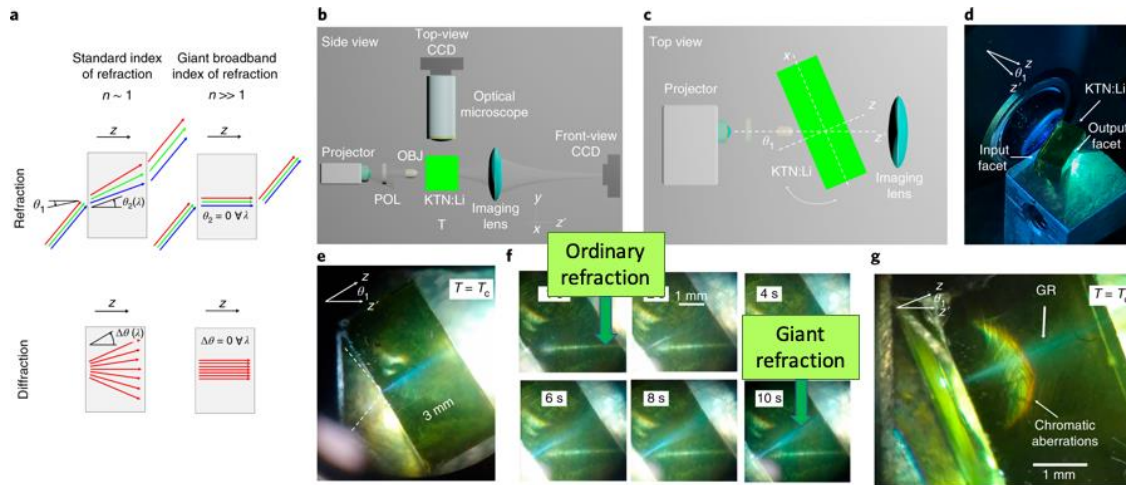
Figure 41. This reproduces Fig. 1 from Ref. 184. The key points are in panels e and g, where the GR beam propagates normal to the crystal face, and for incident white light (g) shows evidence of chromatic aberration on a mm scale. In panels f, on the other hand, the GR beam grows in alongside the normal diffracted beam only gradually with time as the crystal equilibrates at T_c, on a scale of seconds.

The supercrystals have the same sub-nanometer unit cells as the perovskite KTN:Li, but are organized into supercells with alternating regions of high and low niobium. Neighboring supercells – within which the individual dipoles are locally ordered – are also antiferroelectrically ordered as one crosses domain walls in both 90˚ and 180˚ rotation planes. That structure appears to freeze in over a period of seconds just below the Curie temperature T_c after dipolar relaxation to the ferroelectric phase at T_c-2K. The observed diffraction anisotropy – the forward jet – forms because there are no grating planes in the *y-z* crystal face to diffract the incident phase front.

As the authors of Ref. [184] observe, only the components of the light impinging on regions of the supercrystal with the correct anisotropy undergo GR; the other components experience normal Snell's law refraction. The GR beam is shown in **Figure 42**, Ref. [184], to undergo filamentation on a scale of μm, compatible with the size of the supercrystal domains. But this observation does not appear to be compatible with the idea of a giant refractive index that preserves memory of the phase front of an incident optical beam – and therefore also raises serious doubts as to the proffered explanation of the phenomenon.
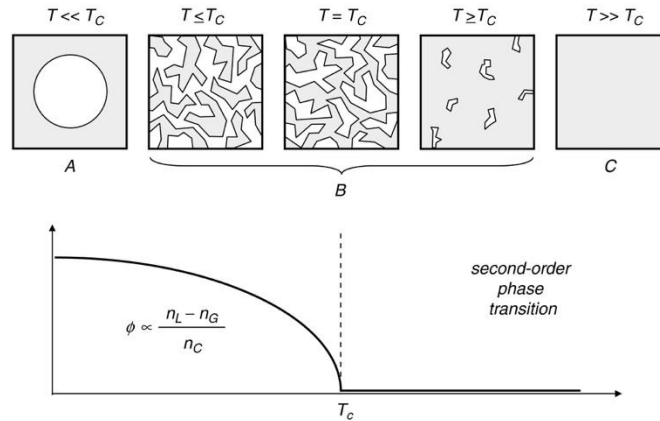
Figure 43. Schematic material structures of a two-phase system for a second-order phase transition at various temperatures, where T_c designates the critical temperature. Ref. [185].
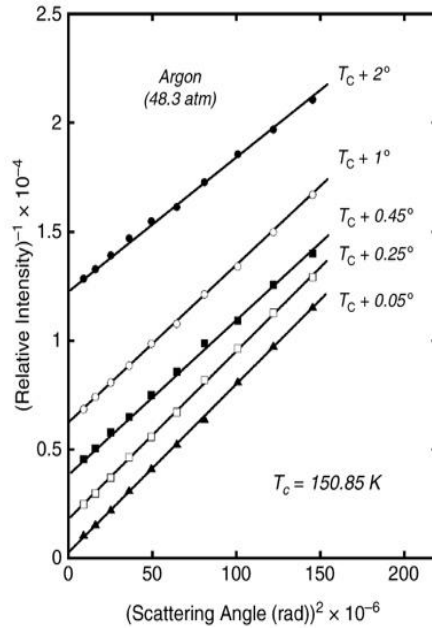
Figure 44. X-ray scattering from argon near the critical liquid-vapor phase transition temperature. Ref. [186]

So, if GR is not an appropriate way to describe what is observed in KLTN, is there a better way to understand what is happening? Given the prominent place occupied by critical temperature in the GR phenomenology, it is sensible to ask what can be learned by thinking about the second-order phase transition. As shown schematically in **Figure 43**, at T_c, the fractional difference between the number density of the two phases $\Delta = n_{PE}\text{-}n_{FE}/n_{total}$ is precisely zero, and the specific way in which the two phases order themselves will probably determine the way the KLTN composite responds to light scattering.

In KLTN, we will have equal concentrations of electric dipoles in the disordered paraelectric phase and the ordered ferroelectric phase at T_c; in the super-crystal, that may very well lead to preferential or coherent scattering of visible light from the ordered phase, given its μm-scale dimensions. But this phenomenon has long been known in the scattering of electromagnetic radiation from two-phase mixtures undergoing

second-order phase transitions: It is called critical opalescence. An example of small-angle X-ray scattering at the phase boundary between gas-phase and liquid-phase argon is shown in **Figure 44**, in which the inverse scattering amplitude is plotted as a function of the square of the scattering angle. As the critical temperature is approached from above, the scattering amplitude rises rapidly, with more and more scattering amplitude confined to small forward angles.

This appears to be very similar to the strong forward "jetting" that is observed in **Figure 42 e-g** – suggesting that what is being observed is not refraction, but rather coherent forward scattering caused by the ordered dipoles in the ferroelectric phase of the KLTN.

This leads to new questions to be investigated (1) Can coherent light scattering of the GR type produce metalens functionality? That would require some way to reconstruct phase fronts using a metasurface layer, and it is not clear that the answer can ever be affirmative. (2) Is there a role for critical phenomena like those observed in KLTN in the design and optical functionality of a metalens? When Prof. Richard Haglung visited Prof. Owen Miller at Yale on February 18th, he raised this question with Prof. Charles Ahn and Prof. Frederick Walker in Prof. Owen's department, both with deep experience with the electronic properties of ferroelectrics, and they referred him to a recent paper on $BaTiO_3$, another ferroelectric with a perovskite structure like KLTN. This paper seems to advance a generic perspective on using correlated electron phenomena to achieve optical functionality.

5.3.1 SELF-ACTION AS A POSSIBLE MECHANISM FOR GIANT REFRACTION

A key claim about the GR phenomenon is that should be observable in a strongly correlated material in which "susceptibility is dominated by local fields, [so that] n can be anomalously enhanced through self-action."[184,185] Self action, by definition, assumes that when the incident electric field induces a change in polarizability, this in turn interacts with and modifies the incident field – an effect that is well known in nonlinear optical phenomena, such as multi-photon absorption or nonlinear refraction. However, nonlinear optical effects have small cross sections, typically decreasing from linear processes by 10^{-12} per order of the nonlinearity. Thus, the cross section for nonlinear refraction n_2I, a third-order nonlinear process, is a small fraction of the linear index of refraction even at high optical intensity – which was certainly not the case for the Di Mei experiment with its low-power white-light source.

Of more significance is the fact that the sign of the nonlinear index n_2 can be either positive (self-focusing) or negative (self-defocusing); only the former is conceivably interesting for imaging. So, for example, the newly discovered two-dimensional (2D) halide perovskites have recently been shown to have very large nonlinearities, but it turns out that the large n_2 values are negative.[186-190] Moreover, an extensive survey[191] of the nonlinear properties of semiconductors and insulators – including the ferroelectric $LiNbO_3$ – shows that nonlinear contributions to the refractive index are additive and of order less than 1. That is, nonlinear refractive effects are not multiplicative, and require light intensities greater than 100 MW/cm^2 to be significant.

From general principles, the refractive index in an isotropic medium satisfies the Lorentz-Lorenz relation $n^2 = \{1+(8/3)\pi Na)/[1-(4/3)\pi Na]\}$, where N is the number density of atomic dipoles and a is the polarizability.[192] DiMei *et al.* then argue that in the vicinity of a phase transition, it is possible that $(4/3)\pi Na \sim 1$, leading to a large (linear) index of refraction, and cites as evidence a paper describing quantum enhancement of the refractive index near the phase transition in a Bose-Einstein condensate (BEC).[193] But in that report, the quantum enhancement is only a few *per cent*, the number density is of 10^{14} cm^{-3}; in discussing the mechanism, the authors explicitly note that the Lorentz-Lorenz correction is negligible as seems reasonable given that the density of the BEC is so low. It appears, then, that this line of argument leads to a dead end. Whether a solid-solid phase transition can in fact yield such a condition remains an open question.

5.3.2 PROGRESS TOWARD EXPERIMENTAL TESTING OF ENHANCED REFRACTION

As noted in the February report, the Di Mei KLTN supercrystals have the sub-nanometer unit cells like the perovskite KTN, but are organized into supercells with alternating regions of high and low niobium density (arising from the off-center Czochralski crystal-growth process[185] employed), with a superlattice constant of 5.5 µm.[186] Neighboring supercells – within which the individual dipoles are locally ordered – are antiferroelectrically ordered as one crosses domain walls in both 90˚ and 180˚ rotation planes. That structure appears to freeze in just below the Curie temperature T_c ; the observed diffraction anisotropy – the forward jet – forms because there are no grating planes in the y-z crystal face to diffract the incident phase front.

When I visited Owen Miller on February 18th, I discussed these questions with Charles Ahn and Frederick Walker, both with deep experience with electronic properties of ferroelectrics, and they referred me to a recent paper on $BaTiO_3$, another ferroelectric with a perovskite structure similar to that of KLTN.[194] This paper advances a generic perspective on using correlated electron phenomena to achieve optical functionality near a phase transition, suggesting that if there are GR-like effects in KLTN, there might be hints in other ferroelectrics near their phase transition.

With William Martinez (Vanderbilt Institute for Nanoscale Science and Engineering - VINSE), we have begun discussions on how to fabricate thick (2-3 µm) films of KLTN and other doped and undoped ferroelectrics to search for unusual optical nonlinearities, and to investigate the effects of lithium doping. VINSE facilities include both CVD (chemical vapor deposition) and sputtering tools capable of growing thick films either in layer-by-layer fashion or a continuous deposition cycle. The techniques for growing oxide-ferroelectric films are exceedingly well developed, given their long commercial history.[195-197] Once the current coronavirus pause ends and VINSE facilities become available, we will then begin depositions of KTN, $BaTiO_3$ and $LiNbO_3$ to establish deposition protocols. We can then explore the nonlinear properties of phase-changing metasurfaces made up of small (~5 µm lateral dimensions) supercells of the ferroelectrics created in various array geometries, using standard oxide-etch protocols.

5.3.3 SYNTHESIZING THE GR MATERIALS

We have been able to locate a supplier of sputtering targets who can make both KTN and the lithium-doped KTN, and have therefore added KTLN as a fourth model material to the list in the last report, to be synthesized in a metasurface geometry, as summarized in the **Table 15**. The Curie temperature is the temperature below which ferroelectric local order is possible.

Table 15. List of model materials.

Material	Structure	Local order	Curie temperature
KTN (KTN)	Perovskite	Ferroelectric	20˚C
KTLN	Perovskite	Ferroelectric	20˚C
$BaTiO_3$	Perovskite	Ferroelectric	120˚C
$SmNiO_3$	Perovskite	Antiferromagnetic	400˚C

We are growing thick (3-5 µm) films of $KTa_xNb_{1-x}O_3$, $KTa_xLi_dNb1_{-x}O_3$, $BaTiO_3$ and $SmNiO_3$ by rf magnetron sputtering[196] using a continuous deposition cycle. Techniques for growing correlated-oxide films, including ferroelectrics have a long commercial history, so that there are standard "recipes" available in the literature. VINSE also the facilities needed for microstructuring surfaces at the desired scale, including a laser writer, a photolithography tool, and wet- and plasma-etch capabilities.

We will begin materials synthesis and optical experiments on $KTa_xNb_{1-x}O_3$ (KTN) and $KTa_xLi_dNb1_{-x}O_3$ (KTLN) as the highest priority, because KLTN is identical to the Di Mei crystals, while KTN is also undergoes a paraelectric to ferroelectric transition, but does not have the small lithium dopant that DiMei *et al.* argue is responsible for the unique properties of their material. We expect that this direct comparison will answer questions about the effect of local disorder in the KLTN material *vis á vis* KTN, the role of the phase transition, and effects of local order (ferroelectric *vs* anti-ferromagnetic). Depending on the outcome of the optical experiments, we will then decide whether to proceed with Metasurfaces of the model materials will be designed with the aid of the Lumerical® software, consisting of small (~5 µm lateral dimensions) supercells in various array geometries, using photolithography and standard oxide-etch protocols. Crystallinity, structure, and stoichiometry will be assessed using tools also available in the VINSE facilities.

5.3.3.1 OPTICAL EXPERIMENTS

The nonlinear optical properties of phase-changing metasurfaces will be investigated in the Haglund optics laboratories, are now returning to normal levels of research activity. In addition to standard linear refraction and angle-dependent diffraction measurements that we have set up during the past month, we can also make sensitive measurements of second[17] and third-order[18] nonlinear optical properties of correlated materials. The experimental layout for the nonlinear optical experiments, and the data acquired in a recent measurement on another nonlinear heterostructure, are shown in the **Figure 45 and 46**. The second- and third-harmonic peaks arise from the second- and third-order susceptibilities, while the broadband multiphoton photoluminescence (MPPL) arises from incoherent electronic excitation.
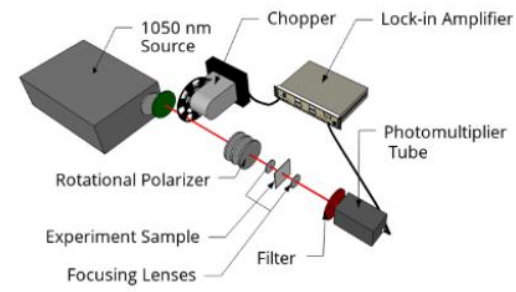

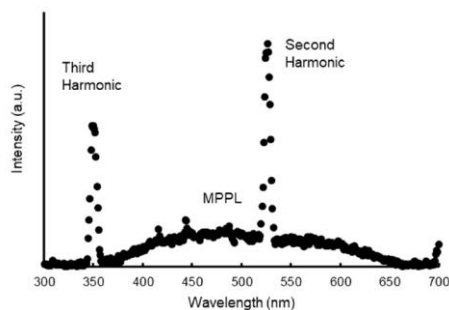**Figure 45. Experimental schematic for measuring the nonlinear susceptibilities of nanostructured samples.**

Figure 46. Monochromator scan of an experimental semiconductor-metal nanostructured bilayer.

5.3.3.2 COMPUTER SIMULATIONS BASED ON OPTICAL CONSTANTS

Given the optical constants of a thin film, it is possible to simulate the response to a specified optical input using finite-difference, time-domain calculations. We have implemented a Lumerical® simulation for arrays of nano- and microstructured arrays, and the test case using zinc oxide has been vetted. We have collected the existing data on optical constants for KTN in the literature and will also measure the optical constants of our films as-grown using variable-temperature spectroscopic ellipsometry to verify the literature values. Metasurfaces of the model materials will be designed with the aid of the Lumerical® software, consisting of small (~5 μm lateral dimensions) supercells in various array geometries, using photolithography and standard oxide-etch protocols. Crystallinity, structure and stoichiometry of thin films and the metasurface structures will be assessed using tools also available in the VINSE facilities.

5.3.4 DEPOSITIONS OF KTN AND KTLN FILMS THROUGH SPUTTERING.

We have deposited and characterized a matched set of KTN and KTLN films at thicknesses up to 100 nm, on silicon and (100) single-crystal substrates of magnesium oxide, using the sputtering parameters in the table below [184]. Both targets "strike" to ignite the sputtering plasma at 40 ccm argon flow, 30 mTorr chamber pressure and 30 W power, well within the limits of our sputtering tool. The quoted deposition rate is nm/minute.

Table 16. sputtering parameters for KTN and KTN:Li films.

Material	Ar (sccm)	O₂ (sccm)	Pressure (mT)	Ramp (s)	Power (W)	Rotation	Height	Tilt	Rate
KTN	20	0	10	40	50	Y	110	10	0.66
KTN:Li	20	0	10	40	50	Y	110	10	0.63

5.3.4.1 CHARACTERIZATION OF SPUTTERED FILMS

The films were grown on 1 cm^2 coupons for variable-temperature spectroscopic ellipsometry and optical spectroscopy measurements. Ellipsometry results in the table acquired at 60˚ and 70˚ input angle agree with published results for the paraelectric phase of KTN.

Table 17. Refractive indices obtained through ellipsometry of KNT and KTNLi deposited on Si and MgO substrates

Material	Substrate	n @ 632.8 nm
KTN	Si	1.91913
KTN	MgO	1.95174
KTNLi	Si	1.9301
KTNLi	MgO	1.88119

The surface quality of the films was characterized using atomic-force microscopy; in each of the micrographs, the sampling is done over a 1 μm x 1 μm area. The arithmetic mean deviation Ra, and mean-square variance Rq and the maximum height difference are all measured in nm; not surprisingly, the KLTN sample is marginally rougher than the KTN. The micrographs themselves suggest that all of the films have similar morphological characteristics, with tightly packed grains.

Table 18 Surface roughness metrics obtained from AFM on KTN and KTNLi films depoisted on Si and MgO.

Material	Substrate	Ra	Rq	Rmax	Skew	Kurtosis
KTN	Si	0.947	1.19	10.6	0.382	3.40
KTN	MgO	0.922	1.15	9.85	0.282	3.02
KTNLi	Si	1.14	1.54	15.6	1.4	10.3
KTNLi	MgO	1.03	1.3	12.2	0.359	3.23

A)

KTN on silicon

B)

KTN on MgO(100)

C)

KTN:Li on silicon

D)
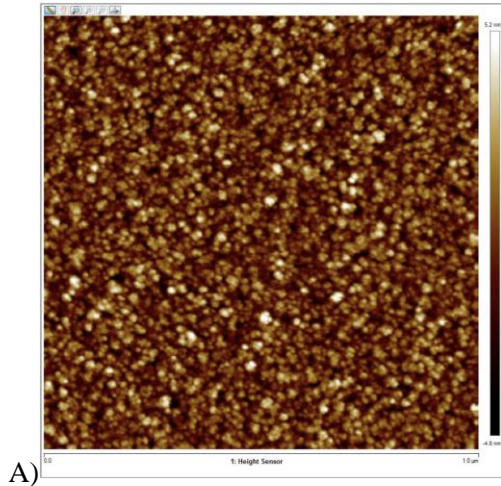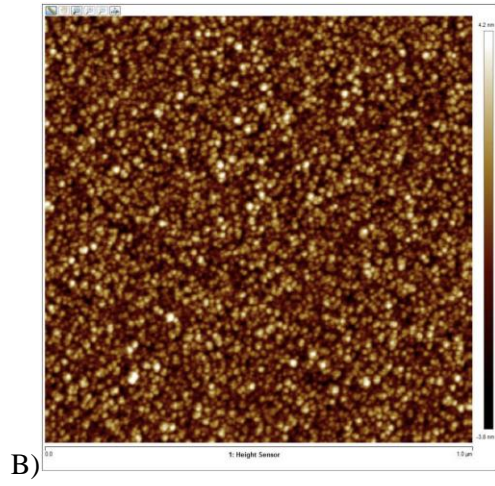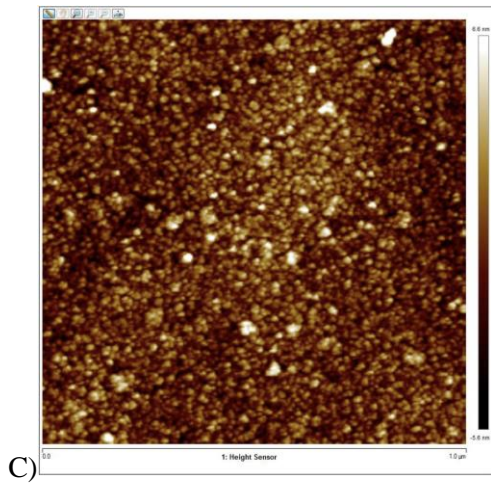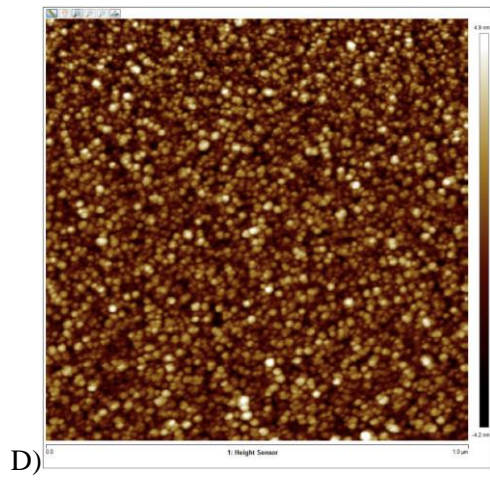
KTN:Li on MgO(100)

Figure 42 AFM micrographs for KTN deposited on A) Silicon and B) MgO substrates as well as KTN:Li on C) silicon and D) MgO.

We characterized a matched set of KTN and KTLN films at thicknesses up to 100 nm, on silicon and (100) single-crystal substrates of magnesium oxide. The films were grown on 1 cm^2 coupons for variable-

temperature spectroscopic ellipsometry and optical spectroscopy measurements. As noted in the February report, ellipsometry results agreed with published results for paraelectric KTN. [13]. As is typical for oxide films, we annealed the as-deposited films at 800˚C in a mild oxygen environment for approximately one hour to reach the desired KTN stoichiometry.
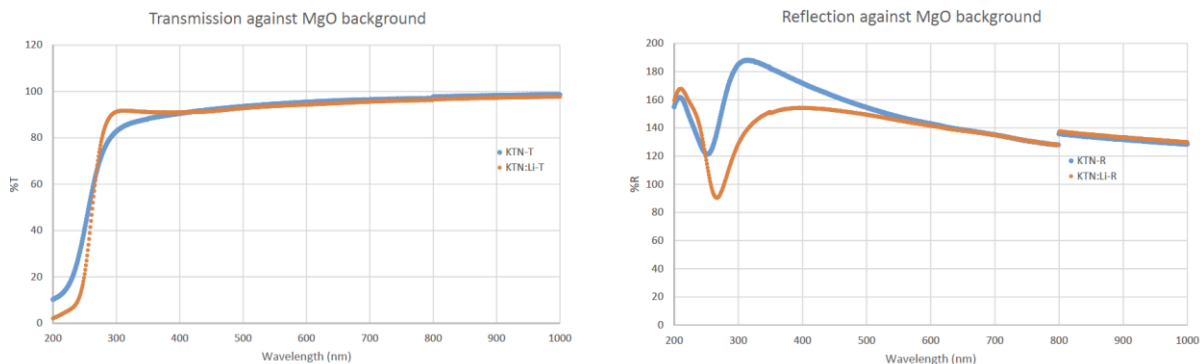
Figure 43 Transmission and reflection for for KTN and KTN:Li films.

As noted in the January 15 2021 report and shown in the figure above, the transmission of KTN and KTNL films on MgO showed no significant differences except below 350 nm, and thus no significant difference in the visible wavelength region where giant refraction (GR) was reported by di Mei *et al*.[184] Raman microscopy and X-ray diffraction studies – which should be sensitive to the nanostructural, domain-level alterations in local crystalline structure hypothesized in the GR report – also showed no difference between the KTN and KTLN films, even though the KLTN films are identical in composition to the Di Mei crystals.

Structural studies of the pre-annealed KTN and KTLN films by X-ray diffraction (XRD) on both the MgO and silicon substrates (below) showed little evidence of the KTN/KTLN films, possibly because the film was too thin. In particular, there were no significant Ta or Nb peaks that we would have expected to see in the 2ϑ scans between 35˚ and 55˚. It is possible that grazing incidence XRD, available in our instrument with minor adjustments, would show those peaks more clearly; however, the pressure of time and other user commitments precluded that.
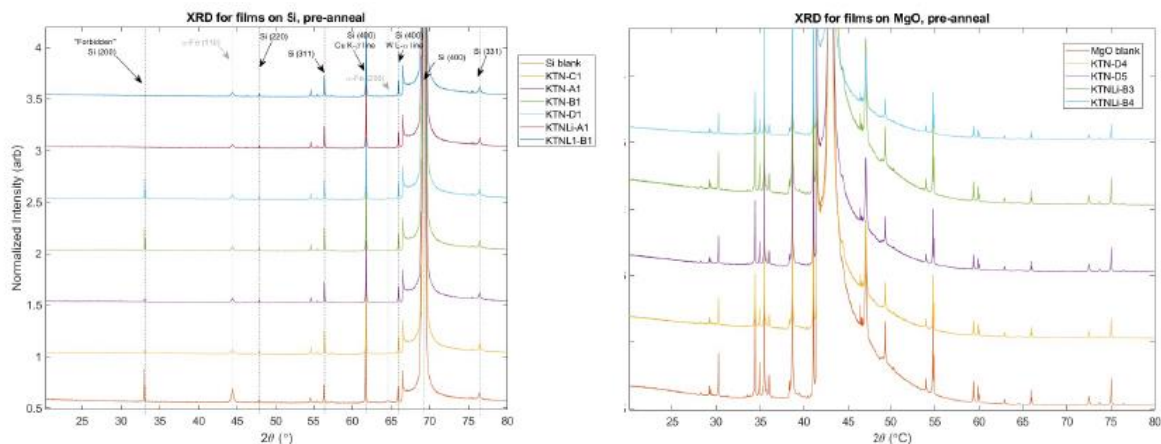
Figure 44 XRD spectra of KTN on Si and MgO substrates before heat treatment.

In contrast to these discouraging results, a comparison of XRD data on the pre-annealed *vs* post-annealed films on silicon show obvious differences (see below), suggesting that annealing yielded the expected improvement in crystallinity, as evidenced by the appearance of stronger peaks in the expected angular range and a decrease in some of the Si signals.
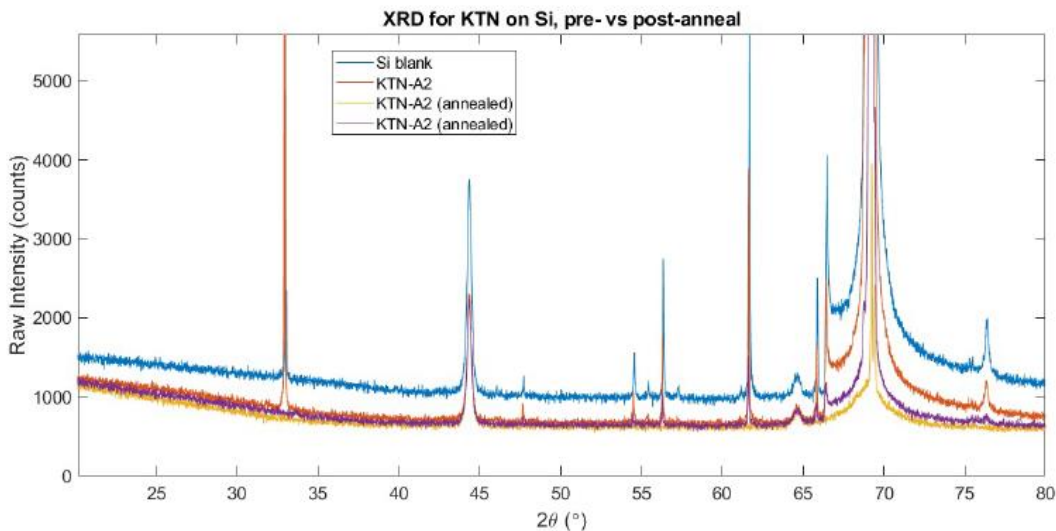
Figure 45 XRD spectra of KTN on Si and MgO substrates after heat treatment.

Raman microscopy of KTN show differences between spectra below and above the phase-transition temperature (298 K = 25°C). The strong central peak is known to be from the silicon substrate; however, the broad feature around 950 cm^{-1} appears to include features from both the substrate and the film. Raman spectra of the bare Si substrate show that this feature has no dependence on temperature as expected, while the samples with KTN do show a variation in this peak above and below the critical temperature. Nevertheless, resolution is poor and further studies will be needed to correlate spectral features with the microstructural difference between KTN and KTLN mooted in [184].
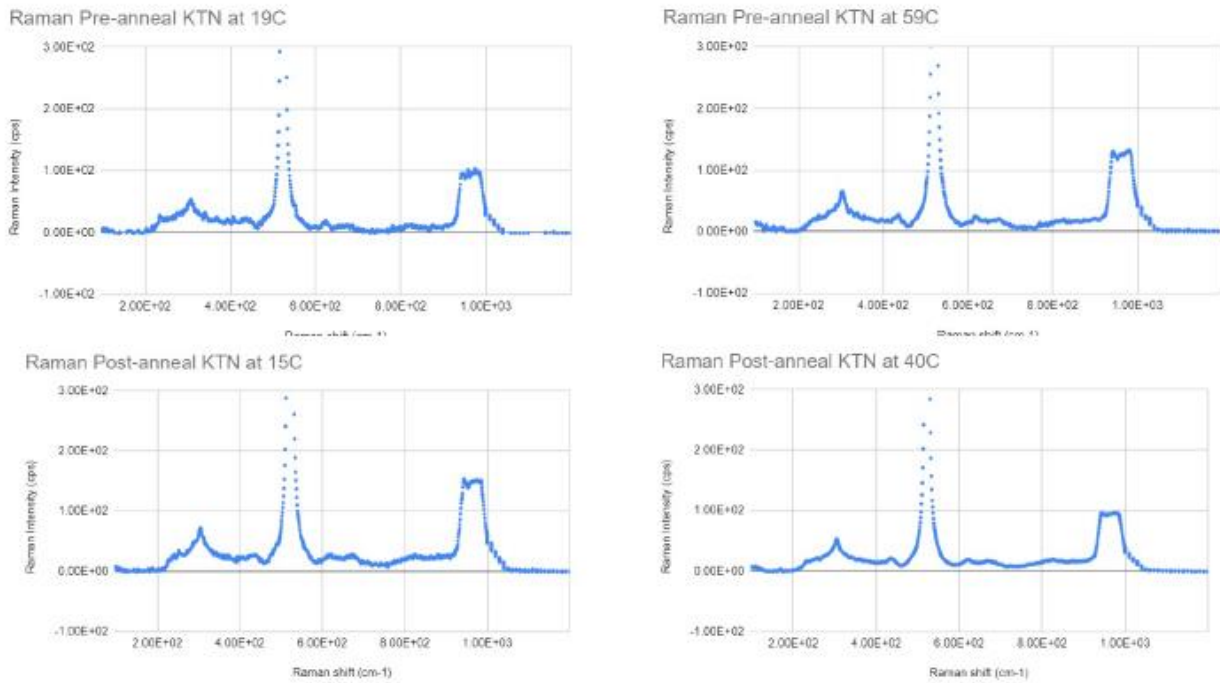
Figure 46 Raman spectroscopy of KTN above and below the ferroelectric transition temperature for KTN with and post deposition annealing.

6. RESULTS OBTAINED

6.1 LIMITATIONS OPTICAL FOCUSING AND DETERMINING BROAD BAND LIMITS

We have established the maximal refractive index valid for arbitrary passive, linear media, given constraints on dispersion or bandwidth. Starting from Kramer's–Kronig relations and the *f*-sum rule that all causal media have to obey, we have obtained a general representation of susceptibility. We have employed linear-programming techniques to demonstrate that the optimal solution is a single Drude–Lorentz oscillator with infinitesimal loss rate, which gave simple, analytic bounds on refractive index. Based on a similar approach, we have obtained bounds on high-index optical glasses and refractive index averaged over arbitrary bandwidth.
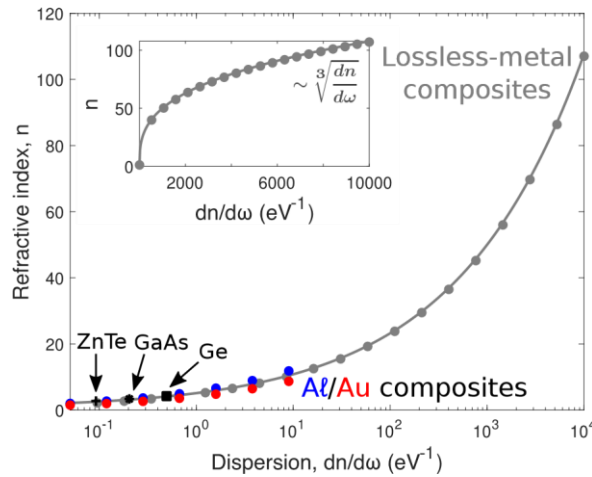
Figure 47 Lower-loss metals would enable even more dramatic enhancements of refractive index. Composites with a nearly lossless metal can be designed to achieve refractive indices larger than 100 at 1550nm wavelength. These composites (circle markers) exactly achieve our bounds (solid line), and require enormous dispersion values to do so, thanks to the cube-root scaling indicated in the inset.

We have also generalized our bounds to any bianisotropic media described by a positive- or negative-semidefinite effective permittivity $\overline{\overline{\varepsilon_{nl}}}(\omega,\mathbf{k})$, rendering our bounds more general than initially expected (i.e., the maximal refractive indices obtained in Sec. 8. II and Sec. 8. IV also describe materials incorporating magnetic, gyrotropic, and other bianisotropic response). We have also designed low-loss metal-based composites with refractive indices exceeding those of best performing natural materials by a factor of two or more. The approach developed herein can be extended to address a variety of related questions. For example, one can allow for gain media, which can still be described by a sum of Drude–Lorentz oscillators with infinitesimal loss rates (see Eq. (4)). However, the oscillator strengths in this scenario need not be positive, leading to different optimal linear-programming solutions depending on the exact objective and constraints. Besides, while we have considered transparent optical materials in this paper, the bounds established here can be used to compare state-of-the-art dielectrics at microwave and other frequencies of interest. One may also be interested in metrics other than refractive index. A key metric in the context of waveguides and optical fibers is group velocity dispersion [184], which can be seamlessly incorporated into our framework.

Another metric closely related to refractive index is the group index, which measures the reduction in *group* velocity of electromagnetic waves in a medium. However, unlike refractive index, the group index can reach values up to 60 even in the near-IR, and much higher elsewhere [185]. This is because group index n_g, by definition, increases with dispersion:

$$n_g = \frac{\mathrm{d}(n\omega)}{\mathrm{d}\omega} = n + \omega\frac{\mathrm{d}n}{\mathrm{d}\omega}.$$
(20)

Since the first term in Eq. (20) is just the refractive index, which is often of the order of unity, the second term, scaling with dispersion, is usually the dominant term for very large values of group index. That being said, we show in the SM that bounds on group index averaged over arbitrary nonzero bandwidth can be obtained based on our refractive-index bound.

One can also explore negative (anomalous) dispersion, which typically occurs around resonances where losses become comparable to refractive index. While our current susceptibility representation is not suited to allow for arbitrarily large losses at the frequency of interest (where we maximize refractive index), one might construct other representations that can describe arbitrary line shapes with anomalous dispersion. We have used Kramer's–Kronig relations to bound refractive index in this paper, but various other integral relations could be useful starting points to branch out to a wide range of problems that are not necessarily linear. The linear programming techniques employed here does not rely on the linearity of the physical quantity of interest and is applicable to nonlinear susceptibility and various other complex, nonlinear phenomena.

Another avenue that can potentially prove fruitful is to better understand the key characteristics of materials that determine refractive index. While the maximum allowable dispersion sets a limit on refractive index, are there more fundamental, physical quantities at play behind the scenes? In the SM, we identify a characteristic trait of high-index materials: a combination of low molar mass and high electronegativity, to achieve large valence electron densities. Going further, it might prove fruitful to combine the insights and directions laid out here with band-structure analysis (through *ab-initio* methods for example), to extract physical properties conducive to high-index materials.

6.2   COMPUTATIONAL FRAMEWORK FOR DESIGN OF MATERIALS

Our intent in one year was to demonstrate feasibility of a systematic framework for key components to designing materials with high refractive indices. The bigger focus of the project is to understand the fundamental physics that drives the high refractive index in materials. Based on the refractive index, materials can be divided into bulk materials and micro-structured materials. As mentioned in the proposal, we are planning to map out a computational framework for design of materials to estimate refractive indices of complex classes of materials. For understanding the relationship of material structures and chemical nature to refractive indices, we need to analyze both the bulk materials and microstructure-dominated materials. As a result, we need to understand what limits the refractive index of materials from fundamental physics and chemistry. This will be helpful to understanding the second class of materials under which meta-materials result.

The research that has exhibited as giant RI by Di Mei et al in 2018 has the chemical structure of K 0.997 Ta 0.64 Nb 0.36 :Li 0.003 (KTN:Li) perovskite. With this as background our intent was to use existing literature data and a variety of modeling and computational methods to further the understanding of how RI can be modulated by chemical and material knobs in bulk materials. In order to systematically address this problem in one year, we used a systematic 4-step methodology which used existing data to narrow the large-scale simulation analysis: 1). Detailed literature review to identify correlations between chemical elements, material chemistry (organic or inorganic), and wavelength dependence; 2). Based on the analysis, identify specific classes of materials for detailed quantum simulation analysis; 3) Use quantum and molecular methods to understand the effect of knobs on RI of specific bulk materials; 4) Combine the different methods to identify design knobs for engineering high RI materials.

Based on literature data of over 1000 materials, and very diversified data, we identified two classes of bulk inorganic materials that can potentially exhibit high dielectric constant and potentially high refractive index as well. They are Chalcogenides and Perovskite materials. The next step of our methodology consisted of simulating specific materials from each of the classes and try to compare them with existing data. Subsequently, we did in silico-based analysis of several material structures, composition, and chemical defects to understand the effects on the dielectric constants. Our analysis indicated that Structure, Cation 2 (Nb or Ta), and oxygen defects are all strong modulator. One of the interesting conclusions is that O defects and crystal structures together can increase the dielectric constant (and hence the refractive index).

Based on our analysis of the wavelength dependence, optimal material for the refractive index needs to satisfy the following three criteria:

1) high value of RI for most of the range of the visible spectrum.

2) high value of the cosine component.

3) relatively flat cosine component.

In addition, the real component of RI needs to be high in the same range. Our analysis indicated that the perovskite ($CH_3NH_3PbI_3$) satisfies the first two criteria. However, its maximum RI is 3.13 and hence lower than the other materials. The other material that satisfies all the three criteria is WS_2. It is also clear from our analysis that a finite band gap is needed in reality for the material to exhibit a higher cosine component and a higher real component of RI, with a smaller imaginary component. Based on our quantum-based analysis, it also appears that these two classes of materials have design parameters that could be used to tune the structure composition space to optimize the required refractive index response for high RI materials.

6.2.1.1 FUTURE WORK

Based on the detailed literature analysis and ab initio simulations, we have identified that both perovskite and chalcogenide materials are capable of exhibiting strong optical property modulation. The analysis illustrated strong potential modulation of the optical property (electronic dielectric constant), due to structure, cations, and anionic vacancies. We think that these two materials may be exhibiting potential non-linear optical responses. This can also be seen in electronic density of states where perovskite materials are changing qualitative behavior with sufficiently high O-defects. Given these exciting observations, we would like to complete three aspects of the analysis as extension of this ongoing 1-year project. These would consist of the following three activities:

1. Simulate using potential-based formalism for structural and time dependent dielectric response

2. Compute phase stability of select KTN materials and defects

3. Synthesizability of recommended materials using Artificial Intelligence-based framework that we are developing for organic chemical synthesis. (This project will be a potential collaboration V. Wheeler, with Naval Research Laboratory on Atomic Layer Deposition).

Potential-based quantum Analysis for estimating dielectric constant as functions of time and structures: For materials problems we need to deal with systems from 10-15 nm (200,000 atoms) to 100 nm (billion atoms) not possible with density functional theory (DFT). The Caltech team has developed systematic approaches to scale atomistic methods to such sizes while retaining the accuracy of DFT. For some applications such as chemical vapor deposition (CVD) growth of materials using potential methods such as ReaxFF and the new generation RexPoN that describes chemical reactions accurately (but at some penalty in computational cost). For applications involving predictions of dielectric response this method

will extend these potential formalisms to optimally bridge with rigorous quantum formalism. The intent is to obtain very accurate estimates of how polarization responds to strain (and vice versa) and then the time dependence for this response. To validate the dielectric properties found using PQEq-UFF, it will be compared with DFT methods in quantum mechanics. After that, the team will use these force field-based formalisms to compute various properties such as polarization, ferroelectricity, and electric field response for other crystal systems. We should emphasize that such characterizations are not possible with any other potential-based formalisms including charge-based models since PQEq is the only charge model that considers explicit QM-based Gaussian electrons with and without masses that can dynamically respond to the electric field. This part of the project will address the following aspects:

1. Static dielectric constants:

    a. Estimate of dielectric constant as $KTaO_3$ is changed to $KTaNbO_3$. We would study specific substitutions of interest

    b. Difference between $KTaO_3$ vs. $KNbO_3$ vs $LiNbO_3$ in terms of response and tying to different structural properties

    c. Effects of the presence of O defects

    d. Similar studies for typical chalcogenide material like $SrVO_3$

2. On frequency dependence:

    a. At THz or higher and will attempt visible spectrum to study potential non-linear effects.

We are planning to work with Haglund on the experimental analysis to test a few of the phase, structure, compositional studies. Although the initial results using these methods (given below) are encouraging, we would like to ensure that the method needs more development before being applied to our system of interest.

Compute phase stability of select KTN materials and defects: The complex nature of these materials makes it imperative that thermodynamic stability of materials need to be understood. This is done using computing Gibbs energy for complex elemental composition. The methods employed in computational thermodynamics can be classified into the following methods: first-principles or ab initio methods, atomistic calculations, and calculations using semi-empirical approaches. While the first two approaches operate on the atomistic level and primarily treat single phases and pure crystals, semi-empirical approaches deal easily with the properties of the multiphase macroscopic body. Semi-empirical approaches are also computationally significantly attractive and amenable to linking with machine learning. Each of these methods needs experimental data for validating the results from the calculations and some also need data to develop the functions that are being used in the calculations. Using the CALPHAD-based formalism, we estimate Gibbs free-energy semi-empirically. This work will estimate thermodynamic phase envelope of perovskite family of materials. This is critical to determining which phases of which materials are stable for synthesis in the laboratory.

Synthesizability of recommended materials using Artificial Intelligence-based framework: We are in the process of developing an Artificial Intelligence-based formalism for complex organic chemical synthesis. While understanding the chemical reactions that drive biological systems and synthetic processes is critical for enabling new insights and applications, the fundamental computational methods used to study chemical reactions have been limited in multiple aspects. To accurately model a system of chemical reactions requires grappling with the complexity of scaling molecular chemical behavior to real systems, where the atomic and electronic movements in reactions are only in local equilibrium. Our methodology addresses the above limitations of current chemical reaction modeling methods that serially

compute chemical and biological reaction systems, which are predominantly parallel in nature. We address this by developing a novel underlying architecture that is specific and optimal for complex chemical systems.

6.3 SYNTHESIS PATHWAYS OF THE PREDICTED MATERIALS WITH MAXIMAL REFRACTIVE INDEX

Studies of KTN and KTLN thin films deposited through sputtering methods during the course of this project do not show any anomalous behavior consistent with the hypothesis of giant refraction (GR) in the visible spectrum. Ellipsometry of the films are consistent with a visible refractive index $n = 1.95$. Particularly in light of Owen Miller's computational results, what we are observing appear to suggest that the observation of giant refraction could be due to the unique fabrication method employed by De Mei which produced highly crystalline samples. More effort in tuning thin film deposition techniques should be undertaken to reproduce these results to obtain thin films with a giant refractive index.

The program has laid foundational work on which we plan to continue materials experiments (such as the effects of variations in annealing protocols) and linear and nonlinear optical experiments [205-207] that complement the work we are doing in other phase-transition materials with unusual intensity-dependent nonlinear optical properties.[208]

7. ESTIMATES OF TECHNICAL FEASIBILITY

We have established the maximal refractive index valid for arbitrary passive, linear media, given constraints on dispersion or bandwidth. Starting from Kramer's–Kronig relations and the *f*-sum rule that all causal media have to obey, we have obtained a general representation of susceptibility. We have employed linear-programming techniques to demonstrate that the optimal solution is a single Drude–Lorentz oscillator with infinitesimal loss rate, which gave simple, analytic bounds on refractive index. Based on a similar approach, we have obtained bounds on high-index optical glasses and refractive index averaged over arbitrary bandwidth. We have also generalized our bounds to any bianisotropic media described by a positive- or negative-semidefinite effective permittivity $\overline{\overline{\varepsilon_{nl}}}(\omega,\mathbf{k})$, rendering our bounds more general than initially expected. We have also designed low-loss metal-based composites with refractive indices exceeding those of best performing natural materials by a factor of two or more.

We used a systematic 4-step methodology which used existing data to narrow the large-scale simulation analysis: 1). Detailed literature review to identify correlations between chemical elements, material chemistry (organic or inorganic), and wavelength dependence; 2). Based on the analysis, identify specific classes of materials for detailed quantum simulation analysis; 3) Use quantum and molecular methods to understand the effect of knobs on RI of specific bulk materials; 4) Combine the different methods to identify design knobs for engineering high RI materials.

We identified two classes of bulk inorganic materials that can potentially exhibit high dielectric constant and potentially high refractive index as well. They are Chalcogenides and Perovskite materials. The next step of our methodology consisted of simulating specific materials from each of the classes and try to compare them with existing data. Subsequently, we did in silico-based analysis of several material structures, composition, and chemical defects to understand the effects on the dielectric constants. Our analysis indicated that Structure, Cation 2 (Nb or Ta), and oxygen defects are all strong modulators. One of the interesting conclusions is that O defects and crystal structures together can increase the dielectric constant (and hence the refractive index).

The program has laid foundational work on which we plan to continue materials experiments (such as the effects of variations in annealing protocols) and linear and nonlinear optical experiments that complement the work we are doing in other phase-transition materials with unusual intensity-dependent nonlinear optical properties.

Finally, in our white paper, we proposed new ideas to pursue based on the outcome of this study as a next step for this program.

8. REFERENCES

[1] N. I. Zheludev and Y. S. Kivshar, From metamaterials to metadevices, Nature Materials **11**, 917 (2012).

[2] N. Yu and F. Capasso, Flat optics with designer metasurfaces, Nature Materials **13**, 139 (2014).

[3] D. Lin, P. Fan, E. Hasman, and M. L. Brongersma, Dielectric gradient metasurface optical elements, Science **345**, 298 (2014).

[4] A. Arbabi, Y. Horie, M. Bagheri, and A. Faraon, Dielectric metasurfaces for complete control of phase and polarization with subwavelength spatial resolution and high transmission, Nature Nanotechnology **10**, 937 (2015).

[5] M. Khorasaninejad, W. T. Chen, R. C. Devlin, J. Oh, A. Y. Zhu, and F. Capasso, Metalenses at visible wavelengths: Diffraction-limited focusing and subwavelength resolution imaging, Science **352**, 1190 (2016).

[6] A. I. Kuznetsov, A. E. Miroshnichenko, M. L. Brongersma, Y. S. Kivshar, and B. Luk'yanchuk, Optically resonant dielectric nanostructures, Science **354**, aag2472 (2016).

[7] A. Li, S. Singh, and D. Sievenpiper, Metasurfaces and their applications, Nanophotonics **7**, 989 (2018).

[8] S. Noda, A. Chutinan, and M. Imada, Trapping and emission of photons by a single defect in a photonic bandgap structure, Nature **407**, 608 (2000). [9] P. Michler, A Quantum Dot Single-Photon Turnstile Device, Science **290**, 2282 (2000).

[10] M. Lonˇcar, A. Scherer, and Y. Qiu, Photonic crystal laser sources for chemical detection, Applied Physics Letters **82**, 4648 (2003).

[11] J. P. Reithmaier, G. Se¸k, A. Lo¨ffler, C. Hofmann, S. Kuhn, S. Reitzenstein, L. V. Keldysh, V. D. Kulakovskii, T. L. Reinecke, and A. Forchel, Strong coupling in a single quantum dot–semiconductor microcavity system, Nature **432**, 197 (2004).

[12] T. Tanabe, M. Notomi, S. Mitsugi, A. Shinya, and E. Kuramochi, All-optical switches on a silicon chip realized using photonic crystal nanocavities, Applied Physics Letters **87**, 151112 (2005).

[13] K. Hennessy, A. Badolato, M. Winger, D. Gerace, M. Atatu¨re, S. Gulde, S. Fa¨lt, E. L. Hu, and A. Imamogˇlu, Quantum nature of a strongly coupled single quantum dot–cavity system, Nature **445**, 896 (2007).

[14] K. Srinivasan and O. Painter, Linear and nonlinear optical spectroscopy of a strongly coupled microdiskquantum dot system, Nature **450**, 862 (2007).

[15] J. B. Khurgin and G. Sun, In search of the elusive lossless metal, Appl. Phys. Lett. **96**, 181102 (2010).

[16] A. Boltasseva and H. A. Atwater, Low-loss Plasmonic Metamaterials, Science **331**, 290 (2011).

[17] A. Yariv, *Quantum electronics*, 3rd ed. (John Wiley & Sons, New York, 1989).

[18] E. Yablonovitch, Statistical Ray Optics., Journal of the Optical Society of America **72**, 899 (1982).

[19] J. A. Schuller, R. Zia, T. Taubner, and M. L. Brongersma, Dielectric Metamaterials Based on Electric and Magnetic Resonances of Silicon Carbide Particles, Physical Review Letters **99**, 107401 (2007).

[20] J. C. Ginn, I. Brener, D. W. Peters, J. R. Wendt, J. O. Stevens, P. F. Hines, L. I. Basilio, L. K. Warne, J. F. Ihlefeld, P. G. Clem, and M. B. Sinclair, Realizing Optical Magnetism from Dielectric Metamaterials, Physical Review Letters **108**, 097402 (2012).

[21] J. Geffrin, B. Garc´ıa-Ca´mara, R. Go´mez-Medina, P. Albella, L. Froufe-P´erez, C. Eyraud, A. Litman, R. Vaillon, F. Gonza´lez, M. Nieto-Vesperinas, J. Sa´enz, and F. Moreno, Magnetic and electric coherence in forwardand back-scattered electromagnetic waves by a single dielectric subwavelength sphere, Nature Communications **3**, 1171 (2012).

[22] Y. H. Fu, A. I. Kuznetsov, A. E. Miroshnichenko, Y. F. Yu, and B. Luk'yanchuk, Directional visible light scattering by silicon nanoparticles, Nature Communications **4**, 1527 (2013).

[23] S. Person, M. Jain, Z. Lapin, J. J. Sa´enz, G. Wicks, and L. Novotny, Demonstration of zero optical backscattering from single nanoparticles, Nano Letters **13**, 1806 (2013).

[24] R. M. Bakker, D. Permyakov, Y. F. Yu, D. Markovich, R. Paniagua-Dom´ınguez, L. Gonzaga, A. Samusev, Y. Kivshar, B. Lukyanchuk, and A. I. Kuznetsov, Magnetic and electric hotspots with silicon nanodimers, Nano Letters **15**, 2137 (2015).

[25] A. Vaskin, J. Bohn, K. E. Chong, T. Bucher, M. Zilk, D.-Y. Choi, D. N. Neshev, Y. S. Kivshar, T. Pertsch, and I. Staude, Directional and Spectral Shaping of Light Emission with Mie-Resonant Silicon Nanoantenna Arrays, ACS Photonics **5**, 1359 (2018).

[26] A. Komar, R. Paniagua-Dom´ınguez, A. Miroshnichenko, Y. F. Yu, Y. S. Kivshar, A. I. Kuznetsov, and D. Neshev, Dynamic Beam Switching by Liquid Crystal Tunable Dielectric Metasurfaces, ACS Photonics **5**, 1742 (2018).

[27] T. Baba, Slow light in photonic crystals, Nature Photonics **2**, 465 (2008).

[28] J. T. Robinson, C. Manolatou, L. Chen, and M. Lipson, Ultrasmall Mode Volumes in Dielectric Optical Microcavities, Physical Review Letters **95**, 143901 (2005).

[29] X. Liang and S. G. Johnson, Formulation for scalable optimization of microcavities via the frequencyaveraged local density of states, Optics Express **21**, 30812 (2013).

[30] S. Hu and S. M. Weiss, Design of Photonic Crystal Cavities for Extreme Light Concentration, ACS Photonics **3**, 1647 (2016).

[31] H. Choi, M. Heuck, and D. Englund, Self-Similar Nanocavity Design with Ultrasmall Mode Volume for Single-Photon Nonlinearities, Physical Review Letters **118**, 223605 (2017).

[32] Q. Zhao, L. Zhang, and O. D. Miller, Minimum dielectric-resonator mode volumes, arXiv:2008.13241 (2020).

[33] S. Nie and S. R. Emory, Probing single molecules and single nanoparticles by surface-enhanced Raman scattering, Science **275**, 1102 (1997).

[34] K. Kneipp, Y. Wang, H. Kneipp, L. T. Perelman, I. Itzkan, R. R. Dasari, and M. S. Feld, Single Molecule Detection Using Surface-Enhanced Raman Scattering (SERS), Physical Review Letters **78**, 1667 (1997).

[35] T. S. van Zanten, A. Cambi, M. Koopman, B. Joosten, C. G. Figdor, and M. F. Garcia-Parajo, Hotspots of GPI-anchored proteins and integrin nanoclusters function as nucleation sites for cell adhesion, Proceedings of the National Academy of Sciences **106**, 18557 (2009).

[36] L. Schermelleh, R. Heintzmann, and H. Leonhardt, A guide to super-resolution fluorescence microscopy, Journal of Cell Biology **190**, 165 (2010).

[37] H. O. Marcy, L. A. DeLoach, J.-H. Liao, M. G. Kanatzidis, S. P. Velsko, M. J. Rosker, L. F. Warren, C. A. Ebbers, P. H. Cunningham, and C. A. Thomas, l-Histidine tetrafluoroborate: a solution-grown semiorganic crystal for nonlinear frequency conversion, Optics Letters **20**, 252 (1995).

[38] M. Jain, H. Xia, G. Y. Yin, A. J. Merriam, and S. E. Harris, Efficient Nonlinear Frequency Conversion with Maximal Atomic Coherence, Physical Review Letters **77**, 4326 (1996).

[39] A. J. Merriam, S. J. Sharpe, M. Shverdin, D. Manuszak, G. Y. Yin, and S. E. Harris, Efficient nonlinear frequency conversion in an all-resonant double-Λ system, Physical Review Letters **84**, 5308 (2000).

[40] V. Petrov, M. Ghotbi, O. Kokabee, A. Esteban-Martin, F. Noack, A. Gaydardzhiev, I. Nikolov, P. Tzankov, I. Buchvarov, K. Miyata, A. Majchrowski, I. Kityk, F. Rotermund, E. Michalski, and M. Ebrahim-Zadeh, Femtosecond nonlinear frequency conversion based on BiB3O6, Laser & Photonics Reviews **4**, 53 (2010).

91

[41] H. H. Li, Refractive index of silicon and germanium and its wavelength and temperature derivatives, Journal of Physical and Chemical Reference Data **9**, 561 (1980).

[42] J. R. DeVore, Refractive Indices of Rutile and Sphalerite, Journal of the Optical Society of America **41**, 416 (1951).

[43] J. Y. Kim, H. Kim, B. H. Kim, T. Chang, J. Lim, H. M. Jin, J. H. Mun, Y. J. Choi, K. Chung, J. Shin, S. Fan, and S. O. Kim, Highly tunable refractive index visiblelight metasurface from block copolymer self-assembly, Nature Communications **7**, 12911 (2016).

[44] J. Shin, J.-T. Shen, and S. Fan, Three-Dimensional Metamaterials with an Ultrahigh Effective Refractive Index over a Broad Bandwidth, Physical Review Letters **102**, 093903 (2009).

[45] M. Choi, S. H. Lee, Y. Kim, S. B. Kang, J. Shin, M. H. Kwak, K.-Y. Kang, Y.-H. Lee, N. Park, and B. Min, A terahertz metamaterial with unnaturally high refractive index, Nature **470**, 369 (2011).

[46] C. Kittel and P. McEuen, *Introduction to Solid State Physics*, vol. 8 ed. (Wiley New York, 1996).

[47] P. Lunkenheimer, S. Krohns, S. Riegg, S. G. Ebbinghaus, A. Reller, and A. Loidl, Colossal dielectric constants in transition-metal oxides, Eur. Phys. J. Spec. Top. **180**, 61 (2009).

[48] W. Hu, Y. Liu, R. L. Withers, T. J. Frankcombe, L. Nor´en, A. Snashall, M. Kitchin, P. Smith, B. Gong, H. Chen, J. Schiemer, F. Brink, and J. Wong-Leung, Electron-pinned defect-dipoles for high-performance colossal permittivity materials, Nat. Mater. **12**, 821 (2013).

[49] F. Di Mei, L. Falsi, M. Flammini, D. Pierangeli, P. Di Porto, A. J. Agranat, and E. DelRe, Giant broadband refraction in the visible in a ferroelectric perovskite, Nature Photonics **12**, 734 (2018).

[50] T. S. Moss, A Relationship between the Refractive Index and the Infra-Red Threshold of Sensitivity for Photoconductors, Proceedings of the Physical Society. Section B **63**, 167 (1950).

[51] N. Ravindra, P. Ganapathy, and J. Choi, Energy gap–refractive index relations in semiconductors – An overview, Infrared Physics & Technology **50**, 21 (2007).

[52] J. D. Jackson, *Classical Electrodynamics, 3rd Ed.* (John Wiley & Sons, 1999).

[53] F. Andreoli, M. J. Gullans, A. A. High, A. Browaeys, and D. E. Chang, Maximum refractive index of an atomic medium, Phys. Rev. X **11**, 011026 (2021).

[54] M. G. Kuzyk, Physical Limits on Electronic Nonlinear Molecular Susceptibilities, Physical Review Letters **85**, 1218 (2000).

[55] M. G. Kuzyk, Fundamental limits of all nonlinearoptical phenomena that are representable by a secondorder nonlinear susceptibility, The Journal of Chemical Physics **125**, 154108 (2006).

[56] J. Skaar and K. Seip, Bounds for the refractive indices of metamaterials, Journal of Physics D: Applied Physics **39**, 1226 (2006).

[57] M. Gustafsson and D. Sjo¨berg, Sum rules and physical bounds on passive metamaterials, New Journal of Physics **12**, 043046 (2010).

[58] M. I. Stockman, Criterion for Negative Refraction with Low Optical Losses from a Fundamental Principle of Causality, Physical Review Letters **98**, 177404 (2007).

[59] G. W. Milton and A. Srivastava, Further comments on Mark Stockman's article "Criterion for Negative Refraction with Low Optical Losses from a Fundamental Principle of Causality", arXiv preprint arXiv:2010.05986 (2020).

[60] R. J. Vanderbei, *Linear programming*, Vol. 3 (Springer, 2015).

[61] H. M. Nussenzveig, *Causality and dispersion relations* (Academic Press, 1972).

[62] M. I. Abdelrahman and F. Monticone, Broadband and giant nonreciprocity at the subwavelength scale in magnetoplasmonic materials, Physical Review B **102**, 155420 (2020).

[63] F. Reiche and W. Thomas, Uber die Zahl der Dis-¨ persionselektronen, die einem stationa¨ren Zustande zugeordnet sind. (Vorla¨ufige Mitteilung), Zeitschrift fu¨r Physik **34**, 510 (1925).

[64] W. Kuhn, Uber die Gesamtsta̋rke der von einem Zu-̋ stande ausgehenden Absorptionslinien, Zeitschrift fűr Physik **33**, 408 (1925).

[65] F. W. King, Sum rules for the optical constants, J. Math. Phys. **17**, 1509 (1976).

[66] J. P. Boyd, *Chebyshev and Fourier spectral methods*, 2nd ed. (Dover, New York, 2001).

[67] M. Cardona and Y. Y. Peter, *Fundamentals of semiconductors* (Springer, 2005).

[68] E. Kaxiras and J. D. Joannopoulos, *Quantum theory of materials* (Cambridge university press, 2019).

[69] L. D. Landau, J. S. Bell, M. J. Kearsley, L. P. Pitaevskii, E. M. Lifshitz, and J. B. Sykes, *Electrodynamics of continuous media*, Vol. 8 (Elsevier, 2013).

[70] J. Nocedal and S. J. Wright, *Numerical Optimization*, 2nd ed. (Springer, New York, NY, 2006).

[71] P. Genevet, F. Capasso, F. Aieta, M. Khorasaninejad, and R. Devlin, Recent advances in planar optics: from plasmonic to dielectric metasurfaces, Optica **4**, 139 (2017).

[72] W. T. Chen, A. Y. Zhu, V. Sanjeev, M. Khorasaninejad, Z. Shi, E. Lee, and F. Capasso, A broadband achromatic metalens for focusing and imaging in the visible, Nature Nanotechnology **13**, 220 (2018).

[73] T. Chang, J. U. Kim, S. K. Kang, H. Kim, D. K. Kim, Y.-H. Lee, and J. Shin, Broadband giant-refractive index material based on mesoscopic space-filling curves, Nature Communications **7**, 12661 (2016).

[74] H. H. Li, Refractive index of alkaline earth halides and its wavelength and temperature derivatives, Journal of Physical and Chemical Reference Data **9**, 161 (1980).

[75] I. H. Malitson, Interspecimen Comparison of the Refractive Index of Fused Silica, Journal of the Optical Society of America **55**, 1205 (1965).

[76] C. Tan, Determination of refractive index of silica glass for infrared wavelengths by IR spectroscopy, Journal of Non-Crystalline Solids **223**, 158 (1998).

[77] M. J. Weber, *Handbook of Laser Science and Technology: Volume 4: Optical Mtls*, Vol. 4 (CRC-Press, 1986).

[78] K. Luke, Y. Okawachi, M. R. E. Lamont, A. L. Gaeta, and M. Lipson, Broadband mid-infrared frequency comb generation in a Si_3N_4 microresonator, Optics Letters **40**, 4823 (2015).

[79] F. Peter, Uber Brechungsindizes und Absorptionskon-̋ stanten des Diamanten zwischen 644 und 226 mμ, Zeitschrift fűr Physik **15**, 358 (1923).

[80] D. L. Wood, K. Nassau, T. Y. Kometani, and D. L. Nash, Optical properties of cubic hafnia stabilized with yttria, Applied Optics **29**, 604 (1990).

[81] D. L. Wood and K. Nassau, Refractive index of cubic zirconia stabilized with yttria, Applied Optics **21**, 2978 (1982).

[82] D. E. Zelmon, D. L. Small, and D. Jundt, Infrared corrected Sellmeier coefficients for congruently grown lithium niobate and 5 mol.% magnesium oxide-doped lithium niobate, Journal of the Optical Society of America B **14**, 3319 (1997).

[83] M. Debenham, Refractive indices of zinc sulfide in the 0405–13-μm wavelength range, Applied Optics **23**, 2238 (1984).

[84] C. A. Klein, Room-temperature dispersion equations for cubic zinc sulfide, Applied Optics **25**, 1873 (1986).

[85] A. S. Barker and M. Ilegems, Infrared Lattice Vibrations and Free-Electron Dispersion in GaN, Physical Review B **7**, 743 (1973).

[86] T. Amotchkina, M. Trubetskov, D. Hahner, and V. Pervak, Characterization of e-beam evaporated Ge, YbF_3 , ZnS, and LaF_3 thin films for laser-oriented coatings, Applied Optics **59**, A40 (2020).

[87] H. H. Li, Refractive Index of ZnS, ZnSe, and ZnTe and Its Wavelength and Temperature Derivatives, Journal of Physical and Chemical Reference Data **13**, 103 (1984).

[88] G. D. Pettit and W. J. Turner, Refractive Index of InP, Journal of Applied Physics **36**, 2081 (1965).

[89] T. Skauli, P. S. Kuo, K. L. Vodopyanov, T. J. Pinguet, O. Levi, L. A. Eyres, J. S. Harris, M. M. Fejer, B. Gerard, L. Becouarn, and E. Lallier, Improved dispersion relations for GaAs and applications to nonlinear optics, Journal of Applied Physics **94**, 6447 (2003).

[90] D. Chandler-Horowitz and P. M. Amirtharaj, Highaccuracy, midinfrared ($450\text{cm}^{-1} \le \omega \le 4000\text{cm}^{-1}$) refractive index values of silicon, Journal of Applied Physics **97**, 123526 (2005).

[91] O. G. Lorimor and W. G. Spitzer, Infrared Refractive Index and Absorption of InAs and CdTe, Journal of Applied Physics **36**, 1841 (1965).

[92] J. H. Burnett, S. G. Kaplan, E. Stover, and A. Phenis, Refractive index measurements of Ge, in *Infrared Sensors, Devices, and Applications VI*, Vol. 9974 (International Society for Optics and Photonics, 2016) p. 99740X.

[93] J. N. Zemel, J. D. Jensen, and R. B. Schoolar, Electrical and Optical Properties of Epitaxial Films of PbS, PbSe, PbTe, and SnTe, Physical Review **140**, A330 (1965).

[94] R. S. Caldwell and H. Y. Fan, Optical Properties of Tellurium and Selenium, Physical Review **114**, 664 (1959).

[95] G. C. Bhar, Refractive index interpolation in phasematching, Applied optics **15**, 305 (1976).

[96] F. Weiting and Y. Yixun, Temperature effects on the refractive index of lead telluride and zinc selenide, Infrared Physics **30**, 371 (1990).

[97] Z.-c. Yan and G. W. F. Drake, Theoretical lithium $2\,2\,\text{S} \rightarrow 2\,2\,\text{P}$ and $2\,2\,\text{P} \rightarrow 3\,2\,\text{D}$ oscillator strengths, Physical Review A **52**, R4316 (1995).

[98] M. Born and E. Wolf, *Principles of optics: electromagnetic theory of propagation, interference and diffraction of light* (Elsevier, 2013).

[99] A. G. Schott, Optical glass data sheets, Retrieved February (2011).

[100] J. B. Hearnshaw, *The analysis of starlight: one hundred and fifty years of astronomical spectroscopy* (CUP Archive, 1990).

[101] H. Hovestadt, *Jena Glass: And Its Scientific and Industrial Applications* (Macmillan, 1902).

[102] L. Bergmann and C. Schaefer, *Optics of waves and particles* (W. de Gruyter, 1999).

[103] P. Hartmann, R. Jedamzik, S. Reichel, and B. Schreder, Optical glass and glass ceramic historical aspects and recent developments: a Schott view, Applied Optics **49**, D157 (2010).

[104] M. G. Silveirinha, Metamaterial homogenization approach with application to the characterization of microstructured composites with negative parameters, Physical Review B **75**, 115104 (2007).

[105] M. Altarelli, D. L. Dexter, H. M. Nussenzveig, and D. Y. Smith, Superconvergence and Sum Rules for the Optical Constants, Physical Review B **6**, 4502 (1972).

[106] V. M. Agranovich and V. Ginzburg, *Crystal optics with spatial dispersion, and excitons*, Vol. 42 (Springer Science & Business Media, 2013).

[107] A. Poddubny, I. Iorsh, P. Belov, and Y. Kivshar, Hyperbolic metamaterials, Nature Photonics **7**, 948 (2013).

[108] L. Ferrari, C. Wu, D. Lepage, X. Zhang, and Z. Liu, Hyperbolic metamaterials and their applications, Progress in Quantum Electronics **40**, 1 (2015).

[109] D. J. Bergman, Exactly Solvable Microscopic Geometries and Rigorous Bounds for the Complex Dielectric Constant of a Two-Component Composite Material, Phys. Rev. Lett. **44**, 1285 (1980).

[110] G. W. Milton, Bounds on the complex dielectric constant of a composite material, Appl. Phys. Lett. **37**, 300 (1980).

[111] C. Kern, O. D. Miller, and G. W. Milton, Tight bounds on the effective complex permittivity of isotropic composites and related problems, Phys. Rev. Applied **14**, 054068 (2020).

[112] G. W. Milton, *The Theory of Composites* (Cambridge University Press, 2002).

[113] G. W. Milton, Bounds on the complex permittivity of a two-component composite material, J. Appl. Phys. **52**, 5286 (1981).

[114] G. W. Milton, Bounds on the transport and optical properties of a two-component composite material, J. Appl. Phys. **52**, 5294 (1981).

[115] D. J. Bergman, Bounds for the complex dielectric constant of a two-component composite material, Phys. Rev. B **23**, 3058 (1981).

[116] Z. Hashin and S. Shtrikman, A Variational approach to the theory of the effective magnetic permeability of multiphase materials, J. Appl. Phys. **33**, 3125 (1962).

[117] K. Okamoto, *Fundamentals of optical waveguides* (Academic press, 2006).

[118] A.I. Vogel, J. Chem. Soc 1833 (1948)

[119] A.I. Vogel, W.T. Cresswell, G. Jeffery, J. Leicester, J. Chem. Soc. 514 (1952)

[120] K.J. Miller, J. Am. Chem. Soc. 112, 8533 (1990)

[121] K. Hattori, W. McCrone, Analyt. Chem. 28, 1791 (1956)

[122] S.F. Marenkin, A.M. Rauhkman, I.N. Matsyuk et al., Inorg. Mater. 27, 21427 (1991). (in Russian)

[123] K. Bascar, C.R. Raja, K. Thangaraj, R. Gobinathan, Mater. Chem. Phys. 28, 1 (1991)

[124] J.D. Grice, E. Gasparrini, Canad. Miner. 19, 337 (1981)

[125] J.A. Kohn, G. Katz, J.D. Broder, Amer. Miner. 42, 398 (1957)

[126] Batsanov, S.; Ruchkin, E.; Poroshina, I. Springer,Singapore Pte Ltd.: Singapore, 2016.

[127] M. Hoppe: Volume 118; Forschungszentrum Jülich GmbH:Jülich, Germany, 2016.

[128] R. Beal and H. P. Huges. Kramers-Kronig analysis of the reflectivity spectra of 2H-MoS2, 2H-MoSe2, and 2H-MoTe2, J. Phys. C 12, 881 (1979)

[129] G.-H. Jung, S. Yoo, Q-H. Park. Measuring the optical permittivity of two-dimensional materials without a priori knowledge of electronic transitions, Nanophotonics 8, 263-270 (2019).

[130] A. M. A. Leguy, Y. Hu, M. Campoy-Quiles, M. I. Alonso, O. J. Weber, P. Azarhoosh, M. van Schilfgaarde, M. T. Weller, T Bein, J. Nelson, P. Docampo, and P. R. F. Barnes. Reversible hydration of CH3NH3PbI3 in films, single crystals, and solar cells, Chem. Matter. 27, 3397-3407 (2015)

[131] Sun, J., Ruzsinszky, A., and Perdew, J.P., Strongly constrained and appropriately normed semilocal density functional. Phys. Rev. Lett. 115, 036402 (2015).

[132] Naserifar, S., Brooks, D.J., Goddard, W.A., and Cvicek, V. (2017). Polarizable charge equilibration model for predicting accurate electrostatic interactions in molecules and solids. The Journal of Chemical Physics *146*, 124117.

[133] Naserifar, S., Brooks, D.J., Goddard, W.A., and Cvicek, V. (2017). Polarizable charge equilibration model for predicting accurate electrostatic interactions in molecules and solids. The Journal of Chemical Physics *146*, 124117.

[134] Kwon, S., Naserifar, S., Lee, H.M., and Goddard, W.A. (2018). Polarizable Charge Equilibration Model for Transition-Metal Elements. J. Phys. Chem. A *122*, 9350–9358.

[135] Oppenheim, J.J., Naserifar, S., and Goddard, W.A. (2018). Extension of the Polarizable Charge Equilibration Model to Higher Oxidation States with Applications to Ge, As, Se, Br, Sn, Sb, Te, I, Pb, Bi, Po, and At Elements. J. Phys. Chem. A *122*, 639–645.

[136] Kwon, S., Naserifar, S., Lee, H.M., and Goddard, W.A. (2018). Polarizable Charge Equilibration Model for Transition-Metal Elements. J. Phys. Chem. A *122*, 9350–9358.

[137] Petousis I, Mrdjenovich D, Ballouz E, Liu M, Winston D, Chen W, Graf T, Schladt TD, Persson KA, Prinz FB., Sci Data. 2017 Jan 31;4:160134. doi: 10.1038/sdata.2016.134.

[138] Petousis I, Mrdjenovich, D, et al, High-throughput screening of inorganic compounds for the discovery of novel dielectric and optical materials. *Sci Data.* 2017 Jan 31;4:160134. doi: 10.1038/sdata.2016.134.

[139] H. Salehi, N. Shahtahmasebi, S.M. Hosseini, Eur. Phys. J. B, 32, 177, (2003).

[140] D. Ambika, V. Kumar, C. S. Suchand Sandeep and Reji Philip, Appl. Phys. B 97, 661-664, (2009)

[141] W.M. Haynes, CRC Handbook of Chemistry and Physics: 2016-2017, 97th Edition / Boca Raton, Florida: CRC Press, (2016)

[142] S. Batsanov, E. Ruchkin, I. Poroshina, I. Springer, Singapore, (2016).

[143] J. Jeevaratnam, F.P. Glasser, J. Am. Ceram. Soc. 44, 563 (1961)

[144] D. London, M.E. Zolensky, E. Roedder, Canad. Miner. 25, 173 (1987)

[145] N.A. Toropov, Dokl. Acad. Sci. USSR (in Russian) 23, 74 (1939)

[146] S.S. Cole, S.R. Scholes, C.R. Amberg, J. Am. Ceram. Soc. 18, 58 (1935)

[147] J. Schluer, D. Pohl, U. Golla-Achindler, Chile. N. Jb. Miner. Abh. 185, 27 (2008)

[148] N.A. Toropov, P.F. Konovalov, Dokl. Acad. Sci. USSR (in Russian) 66, 1105 (1949)

[149] N.N. Pertsev, W. Schreyer, Th Armbruster et al., Eur. J. Miner. 16, 151 (2004)

[150] L.R. Batsanova, L.A. Novosel'tseva, A.I. Madaras, Inorg. Mater. (in Russian) 10, 621 (1974)

[151] E.M. Levin, C.R. Robbins, J.L. Waring, J. Amer. Ceram. Soc. 44, 87 (1961)

[152] G.F. Claringbull, M.H. Hey, Miner. Mag. 29, 841 (1952)

[153] V.G. Hill, R. Roy, E.F. Osborn, J. Amer. Ceram. Soc. 35, 135 (1952)

[154] K. Walenta, Tscherm. Min. Petrog. 26, 69 (1979)

[155] Y. Baskin, Y. Harada, J.H. Handwerk, J. Amer. Ceram. Soc. 44, 456 (1961)

[156] D.P. Shashkin, M.A. Simonov, N.I. Chernova, et al., Dokl. Acad. Sci. USSR (in Russian) 182, 1402 (1968)

[157] N.N. Vasil'kova, Proc. Miner. Soc. USSR (in Russian) 91, 455 (1962)

[158] S.V. Malinko, B.P. Fitsev, N.N. Kuznetsova et al., Proc. Miner. Soc. USSR (in Russian) 109,469 (1980)

[159] S.I. Kovalenko, A.V. Voloshin, Ya.A. Pakhomovsky, et al., Dokl. Acad. Sci. USSR (in Russian) 272, 1449 (1983)

[160] M.A. Bogomolov, I.B. Nikitina, N.N. Pertsev, Dokl. Acad. Sci. USSR (in Russian) 184, 1398, (1969)

[161] P.F. Konovalov, Dokl. Acad. Sci. USSR (in Russian) 70, 847 (1950)

[162] Nakai, H. Okada, K. Masutomi et al., Am. Miner. 71, 1234 (1986)

[163] Kusachi, C. Henmi, S. Kobayashi, Miner. Mag. 59, 549 (1995)

[164] H. Gaertner, K.L. Roese, R. Kühn, Naturwiss. 49, 230 (1962)

[165] R.M. Honea, F.R. Beck, Am. Miner. 47, 665 (1962)

[166] H.M. Davis, M.A.Knight, J. Am. Ceram. Soc. 28, 97 (1945)

[167] N.L. Dilaktorsky, Proc. Miner. Soc. USSR (in Russian) 68, 18 (1939)

[168] B.W. King, L.L. Suber, J. Am. Ceram. Soc. 38, 306 (1955)

[169] M. Simon, F. Mersch, C. Kuper, et al., Phys. Stat. Solidi a159, 559 (1997)

[170] K. Walenta, P.J. Dunn, G. Hentschel G., et al., Tscher. Min. Petrogr. Mitt. 31, 165 (1983)

[171] R. Basso, G. Lucchetti, L. Zefiro, A. Palenzona. Z. Krist. 201, 223 (1992)

[172] J. Brugger, P. Elliott, N. Meisser, S. Ansermet, Am. Miner. 96, 1894 (2011)

[173] H. Han, L. Cai, H. Hu, Opt. Mater. 42, 47 (2015)

[174] A. Safiankoff, Bull. Acad. Roy. Soc. 5, 1251 (1959)

[175] V.A. Bron, A.K. Podnogin, Dokl. Acad. Sci. USSR (in Russian) 91, 93 (1953)

[176] N. Umemura, K. Yoshida, K. Kato, Appl. Opt. 38, 991 (1999)

[177] S.S. Batsanov, A.S. Sonin, Crystallography (in Russian) 1, 321 (1956)

[178] M.H. Francombe, B. Lewis, Acta Cryst. 11, 696 (1958)

[179] T. Witzke, F. Zhen, K. Seff et al., Am. Miner. 86, 1081 (2001)

[180] J.M. Hughes, R.W. Birnie, Am. Miner. 65, 1146 (1980)

[181] D.W. Strickler, R. Roy, J. Amer. Ceram. Soc. 44, 225 (1961)

[182] P.F. Kerr, F.Young, Am. Miner. 29, 192 (1944)

[183] L.N. Formozova, Rus. J. Gen. Chem. (in Russian) 15, 863 (1945)

[184] Di Mei, F.; Falsi, L.; Flammini, M.; Pierangeli, D.; Di Porto, P.; Agranat, A. J.; Delre, E., Giant broadband refraction in the visible in a ferroelectric perovskite. *Nature Photonics* **2018,** *12* (12), 734-+.

[185] de Oliveira, C. E. M.; Orr, G.; Axelrold, N.; Agranat, A. J., Controlled composition modulation in potassium lithium tantalate niobate crystals grown by off-centered TSSG method. *Journal of Crystal Growth* **2004,** *273* (1-2), 203-206.

[186] Pierangeli, D.; Ferraro, M.; Di Mei, F.; Di Domenico, G.; de Oliveira, C. E. M.; Agranat, A. J.; Delre, E., Super-crystals in composite ferroelectrics. *Nature Communications* **2016,** *7*.

[187] Sidebottom, David, *Introduction to Crystalline and Condensed-Matter Physics* (Cambridge, Cambridge University Press, 2015). Figure 15.9.

[188] Thomas, J. R. and Schmidt, P. W., "X-ray study of critical opalescence in argon," *Journal of Chemical Physics* **39,** 2506 (1963).

[189] Xiong, c., Pernice, W. H. P., Ngai, J. H., Reiner, J. W., Kumah, D., Wlker, F. J., Ahn, C. H. and Tang, H. X., "Active Silicon Integrated Nanophotonics: Ferroelectric BaTiO₃," *Nano Letters* **14**, 1419-1425 (2014).

[190] Abdelwahab, I.; Dichtl, P.; Grinblat, G.; Leng, K.; Chi, X.; Park, I. H.; Nielsen, M. P.; Oulton, R. F.; Loh, K. P.; Maier, S. A., Giant and Tunable Optical Nonlinearity in Single-Crystalline 2D Perovskites due to Excitonic and Plasma Effects. Advanced Materials 2019, 31 (29).

[191] DeSalvo, R.; Said, A. A.; Hagan, D. J.; VanStryland, E. W.; SheikBahae, M., Infrared to ultraviolet measurements of two-photon absorption and n(2) in wide bandgap solids. Ieee Journal of Quantum Electronics 1996, 32 (8), 1324-1333.

[192] Born, M.; Wolf, E., Principles of Optics. 7th ed.; Cambridge University Press: Cambridge, United Kingdom, 1999.

[193] Bons, P. C.; de Haas, R.; de Jong, D.; Groot, A.; van der Straten, P., Quantum Enhancement of the Index of Refraction in a Bose-Einstein Condensate. Physical Review Letters 2016, 116 (17).

[194] de Oliveira, C. E. M.; Orr, G.; Axelrold, N.; Agranat, A. J., Controlled composition modulation in potassium lithium tantalate niobate crystals grown by off-centered TSSG method. Journal of Crystal Growth 2004, 273 (1-2), 203-206.

[195] Xiong, C.; Pernice, W. H. P.; Ngai, J. H.; Reiner, J. W.; Kumah, D.; Walker, F. J.; Ahn, C. H.; Tang, H. X., Active Silicon Integrated Nanophotonics: Ferroelectric BaTiO3 Devices. Nano Letters 2014, 14 (3), 1419-1425.

[196] Sashital, S. R.; Krishnakumar, S.; Esener, S., Synthesis and Characterization of RF-Planar Magnetron-Sputtered KTaxNb1-xO3 Thin Films. Applied Physics Letters 1993, 62 (23), 2917-2919.

[197] Tunaboylu, B.; Sashital, S. R.; Harvey, P.; Esener, S. C., Synthesis and properties of KTN films by sol-gel deposition and RF-magnetron sputtering. Ferroelectrics Letters Section 2001, 28 (3-4), 75-84.

[198] Mantese, J. V.; Micheli, A. L.; Schubring, N. W.; Catalan, A. B.; Chen, Y. L.; Waldo, R. A.; Wong, C. A., Characterization of Potassium Tantalum Niobate Films formed by Metalorganic Deposition. Journal of Applied Physics 1992, 72 (2), 615-619.

[199] Abdelwahab, I.; Dichtl, P.; Grinblat, G.; Leng, K.; Chi, X.; Park, I. H.; Nielsen, M. P.; Oulton, R. F.; Loh, K. P.; Maier, S. A., Giant and Tunable Optical Nonlinearity in Single-Crystalline 2D Perovskites due to Excitonic and Plasma Effects. *Advanced Materials* **2019,** *31* (29), 1902685.

[200] Davidson, R. B. I.; Yanchenko, A.; Ziegler, J. I.; Avanesyan, S. M.; Lawrie, B. J.; Haglund, R. F., All-Optical Field-Induced Second-Harmonic Generation. *ACS Photonics* **2016,** *3* (8), 1477-1481.

[201] Haglund, R. F.; Yang, L.; Becker, K.; Magruder, R. H. I.; Wittig, J. L.; Zuhr, R. A., Picosecond Optical Nonlinearity in Cu Nanocluster Composites Made by Ion Implantation. *Optics Letters* **1993,** *18*, 373-375.

[202] Spear, N. J.; Hallman, K. A.; Hernandez-Pagan, E. A.; Davidson, R. B.; Arrowood, S. L.; Wistuba, A. L.; Tan, W. Z.; Haglund, R. F.; Macdonald, J. E., Enhanced Broadband and Harmonic Upconversion from Coupled Semiconductor and Metal Nanoparticle Films. *Acs Applied Nano Materials* **2020,** *3* (4), 3144-3150

[203] Spear, N. J.; Hallman, K. A.; Hernandez-Pagan, E. A.; Davidson, R. B.; Arrowood, S. L.; Wistuba, A. L.; Tan, W. Z.; Haglund, R. F.; Macdonald, J. E., Enhanced Broadband and Harmonic Upconversion from Coupled Semiconductor and Metal Nanoparticle Films. *Acs Applied Nano Materials* **2020,** *3* (4), 3144-3150.

[204] "Optical Limiting Based on Huygens Metasurfaces," Austin Howes, Zhihua Zhu, David Curie, Jason Avila, Virginia Wheeler, Richard Haglund and Jason Valentine, *Nano Letters* **20**, 4638-4644 (2020).

[205] K. Okamoto, *Fundamentals of optical waveguides* (Academic press, 2006).

[206] T. Baba, Slow light in photonic crystals, Nature Photonics **2**, 465 (2008).

[207] Spear, N. J.; Hallman, K. A.; Hernandez-Pagan, E. A.; Davidson, R. B.; Arrowood, S. L.; Wistuba, A. L.; Tan, W. Z.; Haglund, R. F.; Macdonald, J. E., Enhanced Broadband and Harmonic Upconversion from Coupled Semiconductor and Metal Nanoparticle Films. Acs Applied Nano Materials 2020, 3 (4), 3144-3150.

[208] "Optical Limiting Based on Huygens Metasurfaces," Austin Howes, Zhihua Zhu, David Curie, Jason Avila, Virginia Wheeler, Richard Haglund and Jason Valentine, *Nano Letters* **20**, 4638-4644 (2020).

LIST OF SYMBOLS, ABBREVIATIONS, AND ACRONYMS

AFM – Atomic Force Microscope
AFRL – Air Force Research Lab
BEC -- Bose-Einstein condensate
CVD -chemical vapor deposition
DARPA -- Defense Advanced Research Projects Agency
DFT -- density functional theory
DPFT -- density functional perturbation theory
DSO -- Defense Sciences Office
DTIC -- Defense Technical Information Center
EXTREME -- DARPA DSO Program name
GGA -- generalized gradient approximation
GR -- giant refraction
III-V -- compounds of group III and V elements
II-VI -- compounds of group II and VI elements
IPA -- independent particle approximation
IR – Infrared
KK – Kramers-Kronig
LDA -- Local Density Approximation
NLM -- DARPA DSO Program Name
NLO -- Nonlinear Optics
PBE -- Perdew-Burke-Ernzerhof
RI – Refractive Index
RXAN – Nanoelectronic Materials Branch
SAF – Secretary of Air Force
SCAN -- strongly constrained and appropriately normed
SM -- supplementary material
UFF -- universal force field
UV – Ultraviolet
VASP -- a simulation program
XRD – X-ray Diffraction